University of Nevada, Reno

DESIGN, ANALYSIS AND CONTROL OF SOFT WEARABLE DEVICES USING TWISTED STRING ACTUATORS

A Dissertation Submitted in Partial Fulfillment
of the Requirements for the Degree of Doctor of Philosophy in
Mechanical Engineering

by
Thulani Tsabedze
Jun Zhang, Ph.D. / Dissertation Advisor
December, 2023

THE GRADUATE SCHOOL

We recommend that the dissertation
prepared under our supervision by

Thulani Tsabedze

entitled

DESIGN, ANALYSIS AND CONTROL OF SOFT WEARABLE DEVICES USING TWISTED STRING ACTUATORS

be accepted in partial fulfillment of the
requirements for the degree of

Doctor of Philosophy

Jun Zhang, Ph.D.
Advisor

Yantao Shen, Ph.D.
Committee Member

Matteo Aureli, Ph.D.
Committee Member

Floris van Breugel, Ph.D.
Committee Member

Sesh Commuri, Ph.D.
Graduate School Representative

Markus Kemmelmeier, Ph.D., Dean
Graduate School

December, 2023

ABSTRACT

Physical assistive robotic devices have demonstrated many desirable advantages in rehabilitation and augmentation, allowing for effective performance of activities of daily living (ADLs). Robotic rehabilitation, for instance, allows for accurate and efficient dynamic exercise routines where performance metrics can be easily retrieved. In human augmentation, wearable devices allows human beings to carry heavier loads for longer duration. However, it is challenging to create wearable robotic systems and devices that are inherently safe, compact, and can produce sufficient power and force. Existing robotic devices are often bulky, actuate limited degrees of freedom or produce limited force outputs. The large footprint of the devices usually lead to the devices being tethered either in the lab or in rehabilitation centers, limiting the duration of usage. In addition, active wearable devices that provide resistive capabilities to enable strength training have been difficult to develop.

The properties of the wearable devices — inherent safety, compactness, high force output — is heavily driven by the choice of actuation mechanism. Twisted string actuators (TSAs) are appealing for wearable robotic applications because they are compliant, energy-efficient, capable of producing large translational force, and exhibit high power density. To utilize the properties of TSA, it is important to understand TSAs' key performance metrics to allow for ubiquitous usage. The performance analysis of TSAs is challenging due to the strong coupling between the TSA model parameters. It is important to compare TSA's performance to motor-based actuators, helping in understanding the trade-offs of TSAs compared to motor-based tendon-driven actuators.

This dissertation first provides a theoretical model-based framework to analyze the performance of TSAs focusing on four metrics: contraction range, linear velocity, effective torque input and force output. The performance of the TSA is then compared to the spooled motor-tendon actuator (SMTA). SMTA is a motor based actuation approach that is similar in some regard to TSA. The results of the analysis and comparisons were then used as a basis to select to use TSAs for the actuation approach for the wearable devices in this work. Next, the design, characterization and open loop control of two devices that are driven by TSAs are described in detail. The two devices explored in detail are: 1) wearable glove and 2) wearable wrist orthosis. Specifically, the evolution of the wearable glove is presented in four versions, named a biomimetic robotic assistive glove (BRAG) v1, BRAG v2, Active Wearable Assistive and Resistive Device (AWARD) v1 and AWARD v2. In particular, BRAG v1 used only stiff strings while BRAG v2 and AWARD utilized stiff strings and compliant super coiled polymer strings for position sensing.

In addition, the kinematic modeling, dynamic modeling and closed-loop control of AWARD is presented to demonstrate the different control strategies that can be used to achieve the unique capabilities in trajectory tracking. To allow for full state estimation of the finger motions without requiring tethered approaches, inertial measurement units, supercoiled polymer actuators, force sensitive resistors, encoders and motor current sensors were implemented, ensuring that the footprint and weight of the device is not affected drastically. Position control was implemented in the tendon space and also in the encoder space and demonstrated that desired trajectories were attained.

Dedicated to my loving, supportive family.

ACKNOWLEDGEMENTS

I had tremendous support as I pursued this degree and I want to thank everyone for being on my team. First and foremost, I would like to thank my advisor, Professor Jun Zhang, for his invaluable and insightful mentorship, steady support, kindness and expertise. His drive and vision on research has influenced my thoughts and is a constant inspiration.

Second, I would also like to express my gratitude to my dissertation committee, Professors Yantao Shen, Matteo Aureli, Floris van Breugel, and Sesh Commuri for their time and advice in the preparation of this thesis.

Additionally, I would also like to thank Smart Robotics Lab members — it would have been nearly impossible to complete this work without their contributions. Thank you Erik Hartman, Ammar Alomran, Jennifer Trinh, Revanth Konda PhD and David Bombara for your technical discussions, coffee drinking skills and running skills — you have helped in keeping me sane throughout my PhD.

Finally, I would like to thank my family for their unending support and encouragment. Majahonkhe Shabangu PhD, Jordan Landis MBA, Nicholas Mushaike and Sehluko Dlamini, I am thankful for your deep friendship that continues to color my worldview. I am also grateful to my good friends at UNR — Luiz Carneiro PhD, Megan Higley PhD, Amir Zahiri PhD, Laura Lum, Libby McKenna, Nadav Zimron-Politi PhD, Ashish Kasar PhD and Lily Raymond (in no particular order) — the conversations, runs, crossfit, soccer, volleyball, bike rides and walks, made graduate school a bit more joyful. You have influenced my outlook on life. You are such a strong support system. I am because you are.

TABLE OF CONTENTS

LIST OF TABLES

LIST OF FIGURES

CHAPTER 1

INTRODUCTION

1.1 Background of Wearable Devices

Wearable robotics have not only helped improve mobility in cases of injury or trauma, but can also possibly extend, complement, substitute or enhance human capability and function [1]. Wearable robotics can be broadly classified into two categories: rigid and soft robots. Rigid wearable robots are predominantly composed of rigid links with joints that must match the center of rotations of the human movements, necessitating complicated self-aligning mechanisms and bulky devices [2, 3, 4, 5, 6, 7, 8]. In addition, rigid wearable robotic systems also possess significant inertia which may adversely affect the metabolic costs of the intended human function [9]. Soft wearable robots are manufactured with either compliant actuators or fabrics, leading to compact, lightweight and form-fitting devices. The form-fitting nature allows for the reduction of inertia, and leading to intimate devices that users can utilize for extended period of time. However, the softness and compliance of the materials used need to be carefully selected so that the force output of the devices is not hugely sacrificed. Therefore, the design and component selection have to be selected carefully.

1.2 Design, Modeling and Control of Soft Wearable Devices

In this section, a description of the motivation to develop the three devices presented in this dissertation is outlined. The need, benefit and the difficulty of developing these devices are demonstrated.

1.2.1 Design of soft wearable devices

BRAG Glove

Hands are one of the most important ways that human beings interact with the environment. Whether it is performing Activities of Daily Living (ADL) such as eating or undertaking Instrumental Activities of Daily Living (IADL) such as removing trash and clutter, hand use is critical. The loss of hand function can greatly diminish the ease of environmental interactions and reduce the quality of life. Robotic assistive devices have shown great potential to rehabilitate hand functions [10, 11]. In cases where injuries are incurred, such as spinal cord injury or stroke, assistive gloves can help restore both movement and strength, thereby enhancing the users' quality of life. Assistive gloves can also be used to augment human hand capabilities in order to obtain larger force output. Additionally, assistive gloves can be deployed to provide the needed strength to contract a pressurized Extravehicular Mobility Unit (EMU) glove, relieving fatigue from astronauts and extending the duration of space walks [12].

While multiple assistive and rehabilitation gloves with different actuation mechanisms have been developed [5, 11], these devices predominantly consist entirely of rigid linkages [5], or spooled cables with semi-rigid components [6, 7, 8]. The design approaches produce systems that can generate considerably high force outputs; however, the rigid designs make them unnatural, bulky and potentially dangerous to wearers. Devices with rigid linkages demand matching the centers of rotation of the device and fingers [5], with misalignment causing discomfort. This extra constraint increases the difficulty in designing safe wearable gloves. While high force outputs are desired to efficiently perform ADLs, using high torque actuators may result to relatively compact system that are heavy [7]. Cable-driven methods allow for the actuators to be placed in the forearm. Cable-driven assistive gloves have been proposed for EMU while conducting Extra-Vehicular Activities (EVA) in the past [12]. While cable-driven approaches can allow for compact devices, using conventional spooled configuration require actuators to be perpendicular to the direction of actuation, making it difficult to install on the forearm. In cases where a linear actuator is used [13], the rigidity of linear component may restrict motions of the wrist. Therefore there is a strong demand to develop low-cost, compact, lightweight, and high-performance wearable robotic gloves. In this dissertation, the design of a biomimetic robotic assistive glove (BRAG) will be presented in detail.

AWARD Glove

It is desirable in everyday living, rehabilitation, and space exploration to develop robotic devices that exhibit assistive and resistive capabilities. This not only reduces the need for independent wearable devices for each mode but also minimizes the number of device changes for different specific functions. In rehabilitation, patients could benefit from resistance training to build strength in their previously lost or weakened movement capabilities [14]. In space exploration, assistive and resistive capabilities may be life-saving by reducing detrimental muscle atrophy from long durations in outer space [15]. Further, the assistive glove could be useful for space walks by helping to contract a pressurized EMU glove. This lowers fatigue from astronauts, facilitating various tasks like longer duration space walks [16].

While the need for safe, lightweight assistive and resistive wearable devices are evident, their realization has been difficult. The three predominant factors that make this challenging are: limitations in existing actuator technology, difficulties of realizing compact sensing, and the complex coupling between assistive and resistive modes. An Active Wearable Assistive and Resistive Device (AWARD) was designed to circumvent these challenges and is described in this dissertation.

Wrist Orthosis

While rehabilitation systems have been largely a success in making repetitive rehabilitation tasks easier, and freeing the time physical therapists have to spend with patients, the functionality and portability of these systems are still limited. A majority of the upper extremity rehabilitation devices are still stationary and tethered-table top [11, 17, 18, 19, 20, 21, 22, 23].

Wearable rehabilitation robotic devices can also allow for daily usage, greatly improving the ability of patients to perform ADL [24]. However, the current wearable upper extremity rehabilitation devices are either bulky [25] or rigid, and only provide limited degrees of freedom (DOF) for the wrist [26, 27, 24, 28, 29]. In particular, only flexion/extension is actuated in [26, 28, 27], only pronation/supination in [24, 30, 31], and only pronation/supination coupled with flexion/extension in [32].

While robotic actuators like shape memory alloy (SMA) actuators and super-coiled polymer (SCP) actuators have been adopted in wearable wrist orthosis, the resulting devices were bulky and offered limited DOF [27, 25]. Using pneumatic-based actuators led to soft, lightweight, and compact wrist wearable orthoses [32, 31, 30]; however, the pressure source requirement often meant that these devices needed to remain tethered. Twisted string actuators (TSAs) are based on rotative electromagnetic motors that allows for the usage of small low-torque motors for higher force amplification [33, 34]. Using electromagnetic motors allow for the usage of well developed power sources and makes untethered wearable wrist orthoses possible. The wearable wrist orthosis presented in this work was designed to be compact, high-performance and actuate all the degrees of freedom of the wrist.

1.2.2 Modeling and control of AWARD

It is challenging to utilize a closed form model when modeling soft wearable devices. This, in part, is due to the difficulty in measuring the device to body forces and torques. The difficulty lies in the need of sensors that allow for a transparent knowledge of the state of the device. However, it is challenging to install conventional sensing mechanisms on soft wearable devices which in turn complicates the ability to measure these interactions. For instance, measuring the joint angles of the fingers on a soft wearable device is difficult – installing rotary hall effect sensors is not feasible — space is limited, and the deformation of the fabrics would lead to inaccurate measurements. In addition to the limitation in space to install sensors, wearable devices are prone to slipping and sliding on the users limb (a phenomenon called migration). Further, the deformation of the fabrics or soft materials used can be difficult to model. Due to these challenges, modeling and analyzing soft wearable devices is a challenging task.

In literature, closed-loop control is attained by using lab based motion capture systems [35, 36] like Vicon, OptiTrack, Qualys, electromagnetic sensors [37], strain gauges [38] or vision based approaches to estimate the bending angles of the fingers [39].

A kinematic and dynamic model for AWARD is derived. Due to the choice of compact sensors, a framework to control AWARD is presented and it does not rely on expensive and bulky sensing methods that would have limited AWARD to the lab.

1.3 Contributions

The contributions in this dissertation are:

- Closed-form performance analysis of TSAs based on synthesizing existing TSA models. In addition, a theoretical framework for comparing key performance metrics of TSAs and SMTAs is developed. The metrics are then validated in simulation and experiments.
- Design, characterization and validation of soft wearable devices that are driven by twisted string actuators. These devices included two versions of an assistive and rehabilitation glove (BRAG v1 and BRAG v2), two versions of a wearable glove combining both assistive and resistive capabilities (AWARD v1 and AWARD v2) and a wearable wrist orthosis. The characterization for the devices included range of motion tests on both phantom model and able-bodied human test subject, force output and open-loop control for the manipulation of everyday objects.
- Modeling and closed-loop control of AWARD. The kinematic and dynamic models are sytematically derived, allowing for the implementation of closed-loop control in the encoder space and tendon space is then conducted.

1.4 Dissertation Overview

This dissertation contains ten Chapters. In this chapter, Chapter 1, a brief background on wearable robotic devices is provided. In addition, motivation on the design, modeling and control of wearable devices is outlined. Furthermore, the contributions and the overview of the dissertation are presented.

The next Section (Sec. I) provides a rationale on the choice of actuation mechanism that was used in the design of the devices. Chapter 2 introduced the type of actuation mechanisms predominantly used for wearable robotic devices. More emphasis was placed on the motor-based actuation mechanisms that were introduced, specifically providing detailed background information on twisted string actuators. The different configuration of TSAs and their advantages were discussed. In Chapter 3, an in-depth discussion on the performance analysis of TSAs was conducted. This analysis was systematically performed in closed form and experimental validation was conducted. This analysis clearly demonstrated the reasons TSAs were selected for the use in the wearable devices that were designed and presented in this dissertation.

In the next Section (Sec. II), a detailed design and characterization of the wearable devices are presented. In Chapter 4, the design of BRAG is described. The differences between BRAG v1 and BRAG v2 are highlighted. Chapter 5 describes the design and characterization of AWARD — an Active Wearable Assistive and Resistive Device. The second version of AWARD is presented in Chapter 6. The electrical design and data acquisition is described in this chapter. In Chapter 7, the design of the wrist orthosis is described and characterized.

The next Section (Sec. III) outlines the modeling and control of AWARD. Chapter 8 presents the modeling framework for AWARD, outlining the kinematics and the dynamics. And in Chapter 9, the control approaches are explained and experiments are performed to demonstrate the performance on AWARD. The control of BRAG and the wrist orthosis are left as future work.

Finally, Chapter 10 in Sec. IV , provides a summary of the contributions and the discusses some future work.

Part I

Choice of Actuation

CHAPTER 2

ACTUATION MECHANISMS

A number of actuation approaches have been utilized in the community to design wearable gloves and wrist robotic devices. The actuation mechanisms employed can be broadly divided into two classes: 1) Non-motor based actuation and motor-based actuation. Non-motor based actuation include pneumatic actuators, like fabric based pneumatic actuation, elastomeric actuators, SMAs and SCPs. Motor-based actuation uses electro-magnetic motors on different configurations and transmission system for the drive system of the devices. The predominant motor-based actuators are the spooled motor tendon drive mechanisms and the twisted string actuator.

2.1 Non–motor based Actuators

The non-motor based actuation approaches include pneumatic actuators [40, 41, 42], like fabric based pneumatics [43, 44, 45, 46], elastomeric actuators [47], shape memory alloys [48] and supercoiled polymer actuators [49, 50, 51]. Non-motor based actuation mechanisms tend to be preferred by the community due to their ease in implementation in soft wearable devices. It is unsurprising that a survey found that 64% of soft wearable devices were actuated by pneumatic actuators. Despite that, pneumatic based actuators require pressure sources that may lead to bulky actuation mechanisms. In addition, artificial muscles like SMA and SCPs are thermally driven — their performance is affected by the ambient environment and they may demonstrate low operational frequency.

2.1.1 Supercoiled Polymer (SCP) actuator

SCP actuators, shown in Fig. 2.1, are emergent artificial muscles that use highly twisted thin nylon sewing threads to induce linear motion through heat activated contraction. These artificial muscles are lightweight, low-cost and have high power density — they perform better than biological muscles [52]. Due to these advantageous properties, SCPs have been utilized in various applications like crawling robots [53], soft manipulators [54], soft pumps [55], assistive devices [27] and robotic grippers [56]. SCPs have dual functionality — they can act as actuators and can also work like sensors.

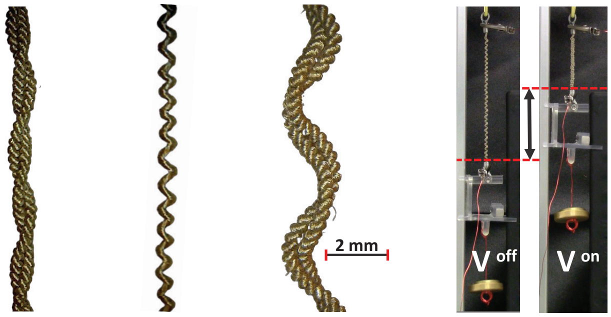

(a) (b) (c) (d)

Figure 2.1: The structures of the three super-coiled polymer actuators: (a) a non-mandrel-coiled, (b) a mandrel-coiled super-coiled polymer (SCP) actuator and (c) a helically-wrapped (HW)-SCP actuator. (d) Actuation of an HW-SCP actuator results in over 50% strain to be generated.

Joule–heating Actuation

When SCPs are used as actuators, actuation can be achieved when heat is provided by external heaters when non-conductive filaments are used or Joule-heated when conductive filaments are used. In cases where compactness is desired, Joule-heated SCPs are preferred since they eliminate the need of external heaters. When used as an actuator, the SCP can attained repeatable contractions between 10−50% of strain, depending on the actuator configuration that is used. As shown in Fig. 2.1, the three configurations are the non-mandrel-coiled, mandrel-coiled and helically-wrapped SCPs. Extensive performance characterization and modeling of the Joule-heated SCPs was presented in our work [57, 58]. In addition, parameter estimation and adaptive control of the SCPs actuators were conducted in our work [59]. For the remainder of work presented in this dissertation, the SCPs were primarily utilized as sensors.

Resistance sensing

SCPs that are manufactured out of conductive silver-coated nylon filaments, not only eliminate the need of external heaters but also allow for resistance sensing. Due to their conductive nature, the resistance of the SCP strings can be measured. The change in resistance of the SCP string is measurable when the strings change in length. The resistance can be measured without consideration of the causes of the change in length. The complicated nature of the SCP strings allow for the resistance measurement to be significant even at small length changes. Using conventional resistance wires to measure the resistance change, significantly large length changes are necessary to induce recognizable resistance change.

The resistance is then used to compute the length of the SCP strings which is in turn used for position sensing. Our group has conducted multiple studies investigating the link between resistance of the SCP strings with the length [60, 61]. For the rest of the dissertation, SCPs were used for position sensing through monitoring the change in resistance.

2.2 Motor–based Actuators

The commonly used motor-based actuators are the SMTAs and TSAs. Both these actuation mechanism utilize tendons to induce motion on the human limb of interest. However, in some cases, the motors are directly attached to linkages for motion [62]. These motor-based actuation approaches are generally preferred due to the higher actuation frequencies that can be achieved. The footprint of the drive units, the output force and torques depend on the selected mechanism. In particular, devices that use SMTA tend to have bigger drive units or limited actuated degrees of freedom [63, 64]. An in-depth background of the TSAs is provided below.

2.2.1 Spooled motor tendon actuator (SMTA)

As shown in Fig. 2.2, an SMTA consists of a spool, pulley, or winch connected to a motor and a tendon (e.g., cable, string, rope, or belt). The SMTA converts the motor's rotation to linear motion [65]. The direction of linear motion is perpendicular to the rotational axis of the spool or pulley [66]. The tendons of the SMTAs allow the motors to be placed at the base of the system, thus reducing the inertia of the system. Therefore robotic and mechatronic systems with low inertia can be realized through the application of forces at distances away from the motor (remote actuation) by using SMTA [65, 67, 68].

SMTAs have been widely used in mechatronics and robotics, including wearable robotic devices [69, 8], aerial grasping manipulation [70], soft robots [66, 71, 72] and in tensegrity robots [73].

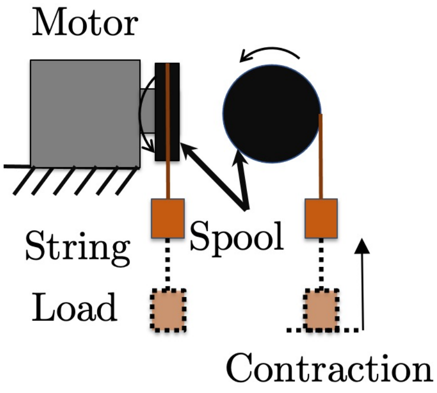

Figure 2.2: A schematic of a spooled motor tendon-driven actuator (SMTA) during actuation.

2.2.2 Twisted String Actuator (TSA)

As an emerging compliant actuation mechanism, TSAs efficiently convert the rotational motion of the motors to linear contraction without requiring extra gears or pulleys [74, 75]. TSAs convert rotative motion to linear travel by twisting two or more strings that are parallel to each other [33, 34], as shown in Fig. 2.3. The configuration of the TSA is such that the direction of movement is inline and parallel to the axis of rotational axis of the motor. High speed, low torque motors can be used in TSA leading to small footprint actuation units that do not sacrifice force and torque performance. TSAs exhibit compliance, high energy efficiency, provide high translational force output, and typically generate maximum strains of 30–40% of their untwisted length [76]. TSAs possess unique advantages over other soft actuators, such as simplicity of construction, low power requirement, and high operating frequency [76, 77]. TSAs have been applied in a variety of applications — including wearable devices [78, 79], soft robots [80], tensegrity robots [81], aerial manipulators [82], mechatronics [83], and haptics [84].

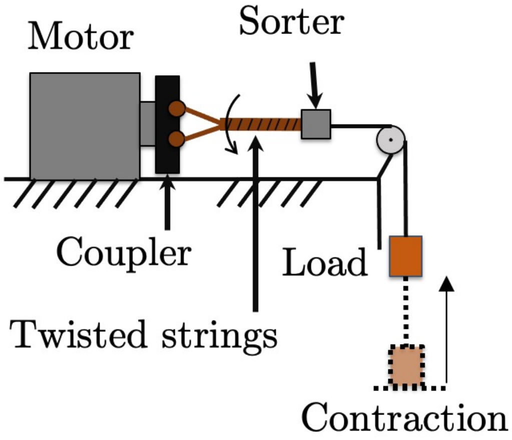

Figure 2.3: An illustration of a twisted string actuator (TSA) during actuation.

The length of the strings can be as long as desired and diameter of the strings can be changed for different performance metrics. The types of strings used for TSA can be changed to attain desired performance. Rigid strings have been predominantly used with TSAs, mainly due to the high force production. However, compliant SCP strings have recently been explored [60]. The compliance is particularly advantageous in wearable devices. The versatility of the TSA — being able to alter the configuration and the types of strings and the advantageous performance, makes the TSA highly attractive in the wearable device community.

There are two types of implementations of the TSA configurations: Variable twisting zone [34] and the constant twisting zone [85]. These types are described below.

Variable twisting zone TSA

The variable twisting zone is also known as the constant or fixed string length TSA. It requires a linear non-rotating rail that constrains rotation but allows translation as shown in Fig. 2.4. Constant string length has been used widely and the key defining characteristics is that the string length does not change during twisting.

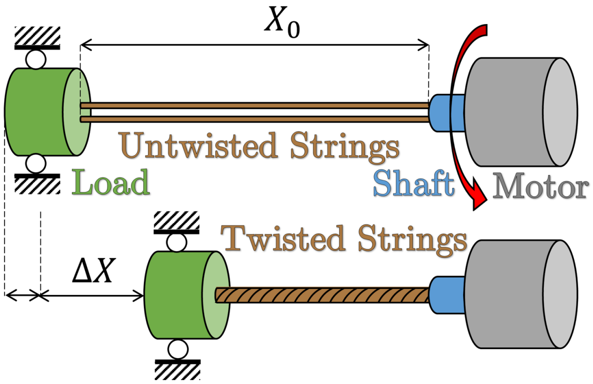

Figure 2.4: A schematic representation of the variable twisting zone TSA configuration.

Fixed twisting zone TSA

The fixed twisting zone TSA is also known as the variable string length. The variable string length implementation has the twisting zone fixed but during contraction, more string feeds into the zone as shown in Fig. 2.5. This requires a fixed sorter to allow strings to feed in but prevent twisted strings from passing through. Most of the existing TSA-based systems have employed a rail system (fixed string), with a sliding spacer [86]. This existing approach leads to devices with more rigid components, potentially deteriorating device comfort and safety.

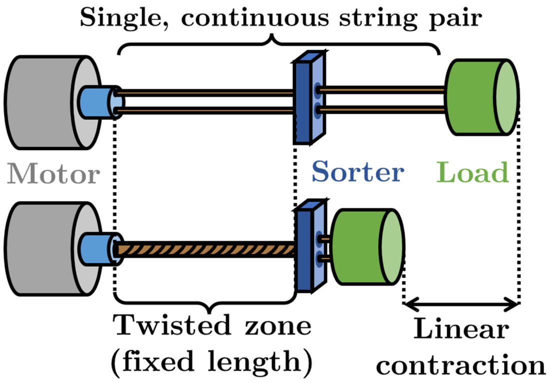

Figure 2.5: An illustration of the constant twisting zone TSA configuration.

CHAPTER 3

PERFORMANCE ANALYSIS OF TSA

3.1 Introduction

While TSAs and SMTAs are both motor-based actuation modes, their performances are vastly different due to their fundamental actuation mechanism. Unlike SMTAs, TSAs generate muscle-like motion, in that the generated force output varies non-linearly over the actuation range [76]. The choice of actuation while developing motor-based robots is often experience-based and not performed systematically. Besides knowing the performance metrics, understanding the trade-offs will ensure the choice of an actuation mechanism that fully leverages its performance while minimizing drawbacks. However, developing comparison framework for TSAs with other motor-based compliant actuators is still an open problem and may help in making an informed decision on the choice of actuation mechanism itself.

The difficulty in developing comparison framework for TSAs lies in the coupling of the models that determine their performance. While the models for both TSAs and SMTAs exist, there has been no work on developing a comparison framework. To effectively develop performance analysis of TSAs, a careful definition of metrics is needed in addition to a systematic synthesis of the governing models, ensuring that the coupling is handled effectively. It is challenging to select comparison metrics that allow for a fair comparison due to their inherent differences.

3.2 TSA Model Overview

The kinetostatic model of the TSA predicts its linear contraction under a given motor rotation. In this study, it is assumed that the TSA is constructed using two strings with approximately infinite stiffness, following existing literature [80, 82]. Relevant variables are depicted in Fig. 3.1.

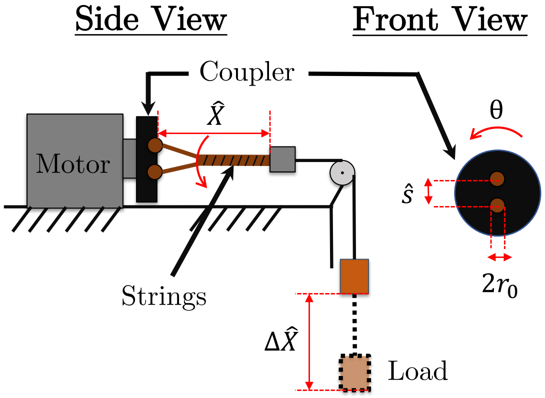

Figure 3.1: Schematic of the TSA during actuation.

When the lateral offset between the strings is not negligible, the length of the twisting zone L' differs from the initial length of the untwisted and unloaded strings, $\hat{L}$. In particular, $L' = \sqrt{\hat{L}^2 - \hat{s}^2/4}$, where $\hat{s}$ is the lateral offset between the two strings. The $\hat{(\cdot)}$ accent refers to all variables specifically for the TSA.

$$\hat{X} = \sqrt{\hat{L}^2\left(1 + \frac{\hat{F}_{ft}}{K}\right) - \left(\hat{\theta}\hat{r} + \frac{\hat{s}}{2}\right)^2}, \tag{3.1}$$

where $\hat{r}$ is the radius of the twisted strings, $\hat{F}_{ft}$ is the fiber tension in the strings, K is the normalized stiffness of a single string [75]. Several existing models approximated that $\hat{s} = 0$ [75, 87]; however, in this work, $\hat{s}$ is not negligible (see Sec. 3.6.1).

The radii of the strings increase as the string length is decreased [74]:

$$\hat{r} = r_0\sqrt{L'/\hat{X}}, \tag{3.2}$$

where r_0 is the initial radius of each of the strings. The number of rotations is $n = \theta/(2\pi)$. It is noted that r_0 depends on the number of strings used in the TSA. In addition, $\hat{F}_{ft}$ also depends on the number of strings used. Specifically, $\hat{F}_{ft} = \hat{F}\hat{X}_{\hat{\theta}=0}/N\hat{X}$, where $\hat{F}$ is the force exerted by the payload, $\hat{X}_{\hat{\theta}=0}$ is the loaded length of TSA with no rotations, N is the number of strings. In this study, it is assumed that the TSA is constructed using two strings ($N = 2$) with approximately infinite stiffness ($K \to \infty$) as used before [82].

The dynamic model of the TSA can be expressed as [87]

$$J\ddot{\theta} + b_\theta\dot{\theta} + \tau_{\mathrm{c}}\mathrm{sgn}(\hat{\tau}_{\mathrm{m}}) + \hat{\tau}_{\mathrm{t}} = \hat{\tau}_{\mathrm{m}}, \tag{3.3}$$

where J is the motor's moment of inertia, b_θ is its viscous damping coefficient, τ_{c} is its Coulombic friction constant, $\mathrm{sgn}(\cdot)$ denotes the sign function, $\hat{\tau}_{\mathrm{t}}$ is the twisting moment of the strings, and $\hat{\tau}_{\mathrm{m}}$ is the motor's torque output. $\hat{\tau}_{\mathrm{m}} = k_\tau i$, where k_τ is the torque constant, and i is the current input to the motor. $\hat{\tau}_{\mathrm{t}}$ can be expressed as [75]

$$\hat{\tau}_{\mathrm{t}} = \hat{F}\hat{r}(\hat{r}\theta + \hat{s}/2)/\hat{X}, \tag{3.4}$$

where $\hat{F}$ is the force exerted by the payload. Eq. (3.4) assumes the string compliance to be negligible. When the strings used have large diameter and the radial normalized stiffness is finite, string compliance is taken into consideration [88, 89].

3.3 TSA Performance Analysis

The performance analysis of TSA is conducted over four metrics, namely, linear contraction, linear velocity ratio, effective torque input, and force output. These metrics were selected due to their predominant use [76, 90, 91]. Performance analysis of TSAs is particularly challenging because of the coupled equations which govern how the aforementioned metrics evolve over the actuation range and time. Under steady-state conditions ($\ddot{\theta} = \dot{\theta} = 0$), and using Eq. (3.4), Eq. (3.3), $\hat{F}$ can be expressed as

$$\hat{F} = \frac{\hat{X}(\hat{\tau}_{\mathrm{m}} - \tau_c)}{\hat{r}(\hat{r}\theta + \frac{\hat{s}}{2})}, \tag{3.5}$$

where $\hat{\tau}_{\mathrm{m}} - \tau_c$ is the effective torque input. This is the torque that will contribute to useful work when the effect of friction is removed from the input torque. For a given TSA setup, there are three unknowns in Eq. (3.5): $\hat{F}$, $\hat{X}$, $\hat{\tau}_{\mathrm{m}} - \tau_c$. In this work, performance is analyzed for a given $\hat{F}$, then computing $\hat{\tau}_{\mathrm{m}} - \tau_c$ and $\hat{X}$. First, Eq. (3.5) is expressed such that for a given $\hat{F}$, only one of the two other metrics is unknown. It is mathematically impossible to solve one equation for two unknowns without additional constraints. For a given TSA, Eq. (3.5) is solved to compute a critical payload $\hat{F}_{\mathrm{critical}}$ where the input motor torque is equivalent to the stall torque τ_{ss} and the TSA can achieve a maximum contraction range $\hat{c}_{\mathrm{max}}$.

In this work, we restrict $\hat{c}_{\mathrm{max}} = 30\%$, which is a conservative upper limit of TSAs' linear strain [74, 75, 76]. From $\hat{c}_{\mathrm{max}}$, the minimum possible TSA length $\hat{X}_{\mathrm{min}}$ is computed. To prevent damage, this study assumes that the current input is limited to 20% of the manufacturer's provided stall current [92]. Thus, $\tau_{\mathrm{ss}} = 0.20\tau_s$, where τ_{ss} is the maximum allowable torque. $\hat{F}_{\mathrm{critical}}$ is computed as

$$\hat{F}_{\mathrm{critical}} = \frac{(\tau_{\mathrm{ss}} - \tau_{\mathrm{c}})\hat{X}_{\mathrm{min}}}{\hat{r}_{\mathrm{max}}(\hat{r}_{\mathrm{max}}\theta_{\mathrm{max}} + \hat{s}/2)}. \tag{3.6}$$

From Eq. (3.6), $\hat{F}$ can be divided into two regions using $\hat{F}_{\mathrm{critical}}$. $\hat{c}_{\mathrm{max}}$ and $\hat{\tau}_{\mathrm{m}} - \tau_c$ can then be computed in closed-form in these two regions.

3.3.1 Contraction range

The contraction range, noted as $\hat{c}_{\text{max}}$, of the TSA is considered to be 30% [76]. The TSA contraction, $\hat{c}$, is

$$\hat{c} = (\Delta\hat{X}/L') \times 100\%, \tag{3.7}$$

where $\Delta\hat{X} = L' - \hat{X}$ is the linear displacement of the payload. $\hat{X}$ is computed using Eq. (3.1). However, to extract the maximum TSA performance in terms of the output contraction, for a given $\hat{F}$, the minimum output length of the TSA can be computed as

$$\hat{X}_{\text{min}} = \begin{cases} (1-\hat{c}_{\text{max}})\hat{L} & \text{if } \hat{F} \leq \hat{F}_{\text{critical}}, \\ \hat{F}\frac{\hat{r}(\hat{r}\theta+\frac{\hat{s}}{2})}{\hat{\tau}_m-\tau_c} & \text{if } \hat{F} > \hat{F}_{\text{critical}}. \end{cases} \tag{3.8}$$

The above equations imply that if $\hat{F} \leq \hat{F}_{\text{critical}}$, then the TSA will be able to achieve $\hat{c}_{\text{max}}$ before the motor stalls. If $\hat{F} > \hat{F}_{\text{critical}}$, then the TSA will exhibit $\hat{c} < \hat{c}_{\text{max}}$, which can be computed using Eqs. (3.8) and (3.7). The computation of $\hat{\tau}_{\text{m}}$, which is used to compute $\hat{X}_{\text{min}}$ when $\hat{F} > \hat{F}_{\text{critical}}$, will be discussed in the subsequent sections.

From $\hat{X}_{\text{min}}$, the maximum number of rotations of the TSA, $\hat{n}_{\text{max}}$, is computed. For a given $\hat{F}$, $\hat{n}_{\text{max}}$ can be computed if L' and r_0 are known. Utilizing the value of $\hat{X}_{\text{min}}$ for different regions of $\hat{F}$ and solving Eqs. (3.1), (3.2), and (3.7) will yield $\hat{n}_{\text{max}}$. Knowing that $\hat{n}_{\text{max}}$ corresponds to the largest string radii and minimum length, and by rearranging Eq. (3.1),

$$\theta_{\text{max}} = \frac{1}{\hat{r}_{\text{max}}}\left(\sqrt{\hat{L}^2 - \hat{X}_{\text{min}}^2} - \frac{\hat{s}}{2}\right), \tag{3.9}$$

where $\hat{X}_{\text{min}} = (1-\hat{c}_{\text{max}})L' \implies \hat{X}_{\text{min}}^2 = (\hat{L}^2 - \hat{s}^2/4)(1-\hat{c}_{\text{max}})^2$ from Eq. (3.7). From Eq. (3.2),

$$\hat{r}_{\text{max}} = r_0\sqrt{\frac{L'}{\hat{X}_{\text{min}}}} = r_0\sqrt{\frac{1}{1-\hat{c}_{\text{max}}}}. \tag{3.10}$$

Therefore, $\hat{n}_{\max}$ can be expressed as

$$\hat{n}_{\max} = \frac{\sqrt{(1-\hat{c}_{\max})[\hat{L}^2(1-(1-\hat{c}_{\max})^2)+(1-\hat{c}_{\max})^2\hat{s}^2/4]}}{2\pi r_0} - \frac{\hat{s}\sqrt{1-\hat{c}_{\max}}}{4\pi r_0}. \tag{3.11}$$

Eq. (3.11) can also be adjusted to compute $\hat{n}$ for any desired $\hat{c}$.

3.3.2 Torque input

To extract the maximum TSA performance in terms of the input torque, for a given $\hat{F}$, the required input torque of the TSA can be computed as

$$\hat{\tau}_m - \tau_c = \begin{cases} \hat{F}\frac{\hat{r}(\hat{r}\theta+\frac{\hat{s}}{2})}{\hat{X}_{\min}} & \text{if } \hat{F} \leq \hat{F}_{\text{critical}}, \\ \tau_{ss} - \tau_c & \text{if } \hat{F} > \hat{F}_{\text{critical}}. \end{cases} \tag{3.12}$$

Eq. (3.12) implies that if $\hat{F} \leq \hat{F}_{\text{critical}}$, then the TSA will be able to achieve $\hat{c}_{\max}$ before the motor stalls. Since $\hat{X}_{\min}$ is known for this region of $\hat{F}$, $\hat{\tau}_m$ can be computed from Eqs. (3.8) and (3.12). If $\hat{F} > \hat{F}_{\text{critical}}$, then the TSA will stall before reaching $\hat{c}_{\max}$. Therefore, the required torque to exhibit $\hat{c}_{\max}$ will be τ_{ss}.

3.3.3 Linear velocity

The linear velocity of the TSA can be obtained by differentiating Eq. (3.1) with respect to time. The TSA's velocity is expressed as [74]

$$\dot{\hat{X}} = -\frac{1}{\hat{X}}\left[\left(\theta\hat{r}+\frac{\hat{s}}{2}\right)\hat{r}\dot{\theta} + \left(\theta\hat{r}+\frac{\hat{s}}{2}\right)\theta\dot{\hat{r}}\right], \tag{3.13}$$

where $\dot{\hat{r}}$ is the rate of change of the TSA's radius. $\dot{\hat{r}}$ can be computed through differentiation of Eq. (3.2). Assuming that $\dot{\hat{r}}$ is small [93], this allowed for further simplification of Eq. (9.4). For a given motor speed $\dot{\theta}$, if the motor does not stall before reaching $\theta_{\max}$, then the maximum linear velocity of the corresponding TSA can be written as

$$\dot{\hat{X}}_{\max} = -\frac{1}{\hat{X}_{\min}} \left(\theta_{\max} \hat{r}_{\max} + \frac{\hat{s}}{2} \right) \hat{r}_{\max} \dot{\theta}. \tag{3.14}$$

It is clear from Eq. (9.4) and (3.14) that $\dot{\hat{X}}$ depends on $\dot{\theta}$. It is ideal to eliminate this dependence. Therefore, instead of computing $\dot{\hat{X}}_{\max}$ directly, the ratio $\dot{\hat{X}}_{\max}/\dot{\theta}$ was computed.

3.4 Comparison Framework with SMTAs

SMTAs are similar to TSAs in that they are motor-based linear actuators that also allow remote actuation, leading to inertia reduction for robotic devices.

3.4.1 SMTA model and performance overview

The SMTA models can be readily derived from first principles. The $\tilde{(\cdot)}$ accent refers to all variables specifically for the SMTA. The variables of interest for SMTAs are shown in Fig. 3.2. The length $\tilde{X}$ of the SMTA can be computed by

$$\tilde{X} = \tilde{L} - \theta \tilde{d}/2, \tag{3.15}$$

where $\tilde{d}$ is the diameter of the spool, $\tilde{L}$ is the total string length when $\theta = 0$.

The dynamic model of the SMTA can also be expressed by Eq. (3.3). The twisting torque $\tilde{\tau}_{\mathrm{t}}$ of the SMTA is

$$\tilde{\tau}_{\mathrm{t}} = \tilde{F} \tilde{d}/2, \tag{3.16}$$

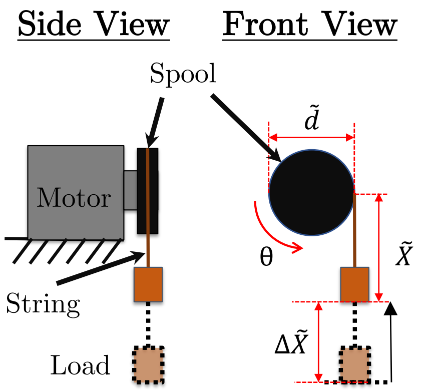

Figure 3.2: Schematic of the SMTA during actuation.

where $\tilde{d}/2$ is the perpendicular distance between the applied force $\tilde{F}$ and the motor's rotational axis. The total torque of the SMTA's motor, $\tilde{\tau}_{\mathrm{m}}$, can be computed using Eq. (3.3).

For completeness and to enhance understanding of the comparisons, similar metrics for the SMTA are defined as well. Under steady-state conditions, the output force, and input torque of an SMTA can be related as

$$\tilde{F} = \frac{\tilde{\tau}_{\mathrm{m}} - \tau_c}{\tilde{d}/2}. \tag{3.17}$$

For a given SMTA, Eq. (3.17) is solved to compute $\tilde{F}_{\mathrm{critical}}$ where $\tilde{\tau}_{\mathrm{m}} = \tau_{\mathrm{ss}}$ and the SMTA can achieve $\tilde{c}_{\mathrm{max}}$. The SMTA can theoretically obtain 100% contraction [65]. This study limits $\tilde{c}_{\mathrm{max}}$ to 90% to ensure safety in operation. $\tilde{F}_{\mathrm{critical}}$ is computed as

$$\tilde{F}_{\mathrm{critical}} = \frac{\tau_{\mathrm{ss}} - \tau_{\mathrm{c}}}{\tilde{d}/2}. \tag{3.18}$$

Consequently, $\tilde{F}$ can be divided into two regions using $\tilde{F}_{\mathrm{critical}}$. $\tilde{c}_{\mathrm{max}}$, $\tilde{\tau}_{\mathrm{m}}$, and $\dot{\tilde{X}}$ can then be computed in closed-form in these two regions.

Contraction Range

For any $\theta \in [0,\, 2\pi\tilde{n}_{\mathrm{max}}]$, the contraction of the SMTA, $\tilde{c}$, is

$$\tilde{c} = (\Delta\tilde{X}/\tilde{L}) \times 100\%, \tag{3.19}$$

where $\Delta\tilde{X} = \tilde{L} - \tilde{X}$ is the linear displacement of the SMTA's payload. $\tilde{X}$ is computed by Eq. (3.15). For a given $\tilde{F}$, $\hat{X}_{\mathrm{min}}$ can be derived as

$$\tilde{X}_{\mathrm{min}} = \begin{cases} (1-\tilde{c}_{\mathrm{max}})\tilde{L} & \text{if } \tilde{F} \leq \tilde{F}_{\mathrm{critical}}, \\ \tilde{L} & \text{if } \tilde{F} > \tilde{F}_{\mathrm{critical}}. \end{cases} \tag{3.20}$$

This implies that when $\tilde{F} \leq \tilde{F}_{\mathrm{critical}}$, the SMTA will obtain $\tilde{c}_{\mathrm{max}}$ before the motor stalls. Otherwise, the SMTA will not exhibit any contraction, since the motor will stall from the beginning of the actuation range.

Using Eq. (3.20), substituting Eq. (3.19) into Eq. (3.15) and solving for $\tilde{n} = \theta/(2\pi)$, $\tilde{n}_{\mathrm{max}}$ is

$$\tilde{n}_{\mathrm{max}} = \frac{\tilde{L}\tilde{c}_{\mathrm{max}}}{\pi\tilde{d}}. \tag{3.21}$$

Torque Input

The torque input $\tilde{\tau}_{\mathrm{m}}$ of the SMTA can be obtained by substituting Eq. (3.16) into Eq. (3.3). For a given $\tilde{F}$, $\tilde{\tau}_{\mathrm{m}}$ can be derived as

$$\tilde{\tau}_{\mathrm{m}} - \tau_c = \begin{cases} \tilde{F}\frac{\tilde{d}}{2} & \text{if } \tilde{F} \leq \tilde{F}_{\mathrm{critical}}, \\ \tau_{ss} - \tau_c & \text{if } \tilde{F} > \tilde{F}_{\mathrm{critical}}. \end{cases} \tag{3.22}$$

This implies that when $\tilde{F} \leq \tilde{F}_{\mathrm{critical}}$, the SMTA will obtain $\tilde{c}_{\mathrm{max}}$ before the motor stalls. In this case, $\tilde{\tau}_{\mathrm{m}}$ can be computed using Eq. (3.22). Else, the SMTA will not exhibit any contraction, since the motor will stall from the beginning of the actuation range.

Linear Velocity

The linear velocity of the SMTA was obtained by differentiating Eq. (3.15) with respect to time

$$\dot{\tilde{X}} = -\dot{\theta}\tilde{d}/2. \tag{3.23}$$

3.4.2 Comparison

Comparisons with SMTAs were performed to understand and synthesize insights from the TSA performance analysis. The comparisons were conducted in two ways: 1) across the actuation range, and 2) peak performance at maximum rotations.

To facilitate the comparison, the following ratios are defined: $\Phi = \hat{X}/\tilde{X}$, $\Lambda = \dot{\hat{X}}/\dot{\tilde{X}}$, $\Psi = \hat{\tau}_\mathrm{m}/\tilde{\tau}_\mathrm{m}$ and $\Gamma = \hat{F}/\tilde{F}$. In particular, Φ is obtained directly from Eq. (3.1) and Eq. (3.15). Similarly, Λ is computed from Eq. (9.4) and Eq. (3.23). It is noted that the torque difference is only due to the last term in Eq. (3.3) for identical motors — motor dynamics are the same. Therefore, Ψ can be expressed as

$$\Psi = \frac{2\hat{r}(\hat{r}\theta + \hat{s}/2)}{\tilde{d}\hat{X}}. \tag{3.24}$$

Γ is obtained from Eq. (3.5) and Eq. (3.17). However, due to the different scaling of the motor dynamics, they cannot be eliminated from the computation. To circumvent this challenge, the maximum force is used for comparison. Γ is given by

$$\Gamma = \frac{\tilde{d}\hat{X}}{2\hat{r}(\hat{r}\theta + \hat{s}/2)}. \tag{3.25}$$

For small $\hat{s}$, there is a singularity when $\theta = 0$. By observation, it can be seen that $\Gamma = 1/\Psi$. As it can be noted, $\Phi, \Lambda, \Psi, \Gamma$ are dependent on θ.

3.5 Simulation Results

3.5.1 Procedure

In this study, micrometal (MM) motors (Pololu: 3071, 4787, 3072) were considered for both TSAs and SMTAs. To simulate their performances, the properties of the motors were obtained from the manufacturer [92]. $\hat{s} = 7.7$ mm, $\tilde{d} = 8.8$ mm, $r_0 = 0.15$ mm, and $\hat{L} = \tilde{L} = 18.4$ cm to be consistent with the experiment (see Sec. 3.6.1). $\ddot{\theta}$ was assumed to be 0 and b_θ was calculated when there was no external load on the motor, so $b_\theta = i_{\text{fr}} k_\tau / \dot{\theta}_{\text{fr}}$, where $i_{\text{fr}} = 0.150$ A is the motor's free-run current. k_τ is the motor torque constant, was estimated using the manufacturer provided current-torque curve and was $k_\tau = 0.323$ kg·cm/A. $\dot{\theta}_{\text{fr}} = 1100$ RPM is the motor's free-run speed. τ_c was also computed using the no load current as $\tau_c = i_{\text{fr}} k_\tau$.

3.5.2 TSA performance

Contraction Range

The maximum displacement of the TSA was 5.67 cm ($\hat{c}_{\text{max}} = 30\%$) and the displacement increased nonlinearly. The average displacement per unit rotation ($\Delta X/n$) was 0.047 cm/rotation. However, $\hat{c}_{\text{max}}$ decreased when the load was increased (Fig. 3.3(a)). For example, for the TSA with 10:1 gear ratio motor, $\hat{c}_{\text{max}} = 30\%$ with loads up to 0.3 kg, after which the $\hat{c}_{\text{max}}$ decreased. $\hat{c}_{\text{max}}$ decreased due to a decrease in $\hat{\theta}$ — a limited number of motor rotations $\hat{\theta} \leq \hat{\theta}_{\text{max}}$ were applied before $\hat{\tau}_{\text{m}} \geq \tau_{\text{ss}}$.

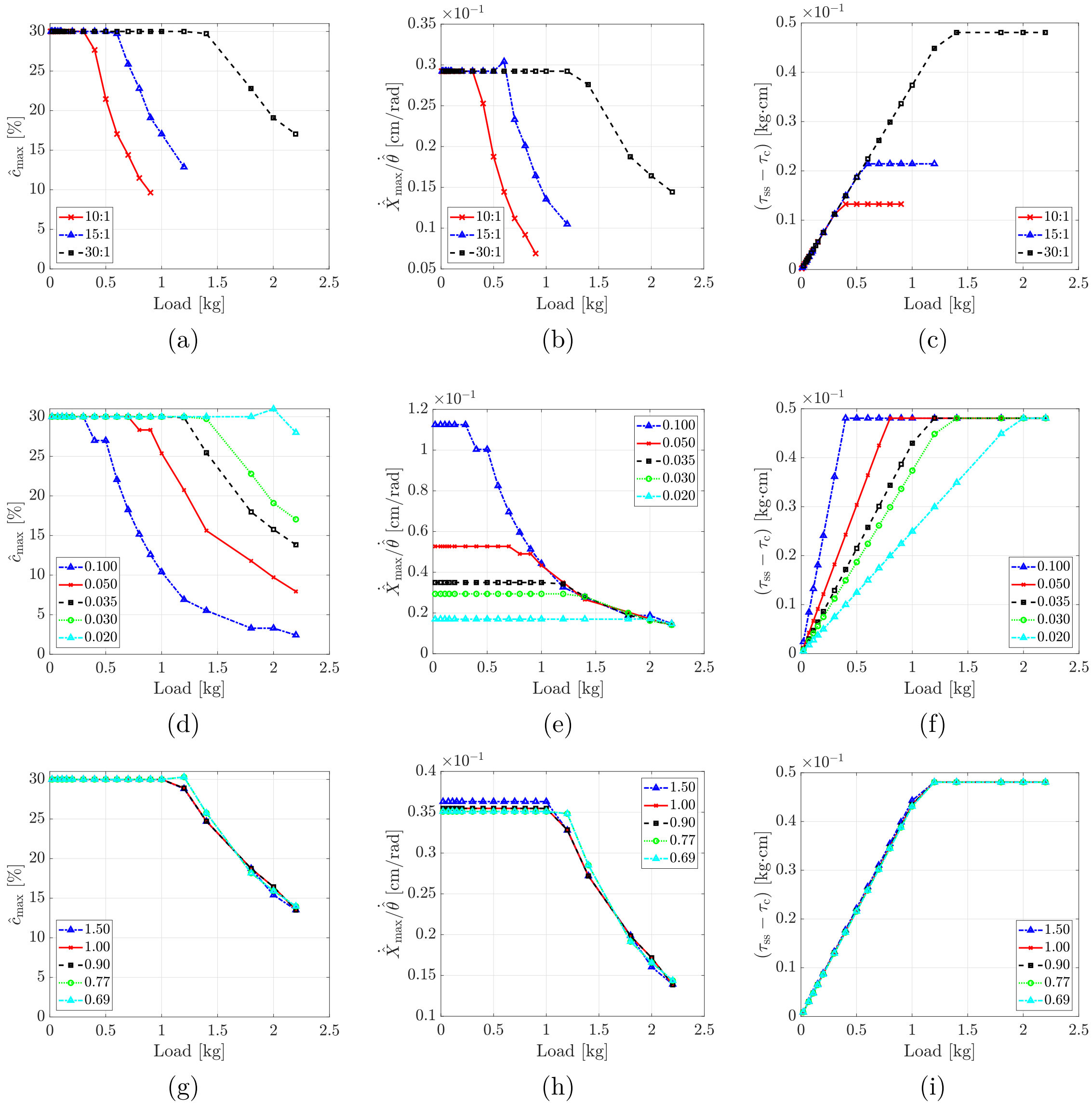

Figure 3.3: (a)–(b) Shows TSA performance for motors of three gear ratios: (a) Maximum contraction, (b) ratio of maximum linear velocity to motor rotational speed, and (c) maximum effective torque input of TSAs. (d)–(f) Shows the effect of changing radius of strings on the performance of TSA on: (d) $\hat{c}_{\max}$, (e) $\dot{\hat{X}}_{\max}/\dot{\hat{\theta}}$, and (f) $\tau_{\mathrm{ss}}-\tau_{\mathrm{c}}$ of TSAs using the 30:1 motor. (g)–(i) Shows the effect of changing string offset, $\hat{s}$, on the performance of TSA on: (a) $\hat{c}_{\max}$, (b) $\dot{\hat{X}}_{\max}/\dot{\hat{\theta}}$, and (c) $\tau_{\mathrm{ss}}-\tau_{\mathrm{c}}$ when the 30:1 motor is utilized.

Linear Velocity

As previously mentioned, the linear velocity is not computed directly, but instead the ratio $\dot{\hat{X}}_{\max}/\dot{\theta}$ is calculated. Increasing the load decreased the ratio $\dot{\hat{X}}_{\max}/\dot{\hat{\theta}}$

(Fig. 3.3(b)). For TSAs, the ratio ranges were around 0.007–0.029 cm/rad for the 10:1, 15:1 and 30:1 motors. It is noted that a zero linear velocity ratio would be achieved when higher loads were used, at the cost of further decreased contraction.

Torque Input

The effective torque input removes the contribution of the the Coulombic friction. This approach ensures that there is limited dependence on motor characteristics on comparisons. The effective torque input for TSAs, shown respectively in Fig. 3.3(c), increased linearly with increased load until saturations were reached. The range of the torque input for TSAs was 0.0013–0.0131, 0.0043–0.0214, 0.0064–0.048 kg·cm for the 10:1, 15:1, and 30:1 motors, respectively. The rate of increase of torque per unit load was 0.043 kg·cm/kg for TSAs.

Force Output

As shown in Fig. 3.3(a)–(c), the maximum force outputs of the TSAs increased as the gear ratios increased. With 10:1, 15:1 and 30:1 motors in TSAs actuated loads up to 0.9, 1.2, and 2.2 kg, respectively. In addition, $\hat{F}_{\text{critical}}$ was 0.31, 0.50, 1.1 kg for the 10:1, 15:1 and 30:1 motors, respectively.

Effect of String Bundle Radius

The effect of the radius on the TSA performance has been investigated. Increasing $\hat{r}_{\text{max}}$ (equivalently increasing $\hat{r}$) decreases $\hat{F}_{\text{critical}}$ (Eq. (3.6)). Consequently, $\hat{c}_{\text{max}}$ will start decreasing sooner. This is evident from Fig. 3.3(d). As the string radius increased from 0.02 cm to 0.10 cm, $\hat{c}_{\text{max}}$ decreased at lower load. The decrease in $\hat{F}_{\text{critical}}$ is slightly more than the square of the radius as shown in Eq. (3.6). The effect of the radius on the speed ratio ($\dot{\hat{X}}_{\text{max}}/\dot{\theta}$) is shown in Eq. (3.14). $\dot{\hat{X}}_{\text{max}}/\dot{\hat{\theta}}$ is directly proportional to approximately the square of $\hat{r}_{\text{max}}$ (Eq. (3.14)). Increasing the radius from 0.020 cm to 0.100 cm, the speed ratio increases (Fig. 3.3(e)). The increase in the effective torque is directly proportional to approximately the square of the radius (Eq. (3.12)). Increasing the radius increases how quickly the stall torque is achieved (Fig. 3.3(f)).

Effect of String Offset

Fig. 3.3(g) demonstrates that increasing the offset slightly decreases the critical load when stall is achieved. Increasing the offset increases the linear speed ratio before the critical force is attained but there is minimal impact in the behavior after the critical force (Fig. 3.3(h)). The effective torque demonstrates minor variations as the offset is increased (Fig. 3.3(i)).

3.5.3 SMTA performance and comparison

Two types of comparisons were performed to analyze TSAs' performance against SMTAs, comparison of 1) the performances across the actuation ranges and 2) the peak performances of both actuators.

Performance Across the Actuation Range

Firstly, the variation of contractions of TSAs and SMTAs are compared. As evident from Eq. (3.1) and Eq. (3.15), the displacement of the SMTA linearly increased with increasing rotations, whereas for TSA, the displacement increased nonlinearly. As shown in Fig. 3.4(a), Φ was smaller than one across the actuation range which demonstrated that the SMTA performs better when contraction is compared.

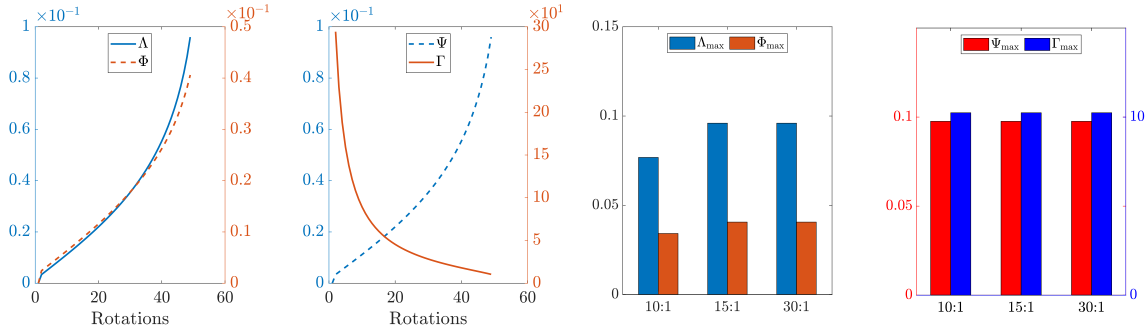

(a) (b) (c) (d)

Figure 3.4: (a)-(b) Comparison during the actuation cycle of the ratios, with (a) showing the variation of Λ and Φ with motor rotations, and (b) showing the variation of Ψ, Γ with motor rotations for the 15:1 motor. (c)-(d) Comparison of the TSA to SMTA using values at $\hat{n}_{\max}$ for $\Lambda_{\max}$, $\Phi_{\max}$, $\Psi_{\max}$, and $\Gamma_{\max}$. It is noted that Λ, Φ, and Γ above one are desirable and Ψ below one is desired.

Secondly, $\dot{X}_{\max}/\dot{\theta}$ for both actuators were compared. $\dot{\hat{X}}_{\max}/\dot{\theta}$ of SMTAs were constant with increased rotations (Eq. (3.23)), whereas in TSAs, $\dot{\hat{X}}_{\max}/\dot{\theta}$ increased nonlinearly with increasing motor rotations (Eq. (3.14)). As shown in Fig. 3.4(a), Λ was smaller than one across the actuation range which demonstrated that SMTA has better performance when linear velocities are compared.

Thirdly, the effective torque inputs applied to the actuators were compared. The effective torque input to the SMTA was constant with increased rotations whereas for the TSAs, effective torque input increased nonlinearly. This behavior is deduced from Eq. (3.22) and Eq. (3.12), respectively. Ψ, as shown in Fig. 3.4(b) exhibited increasing values that are lower than unity. This behavior shows that the effective torque increase of the SMTA is much faster than that of TSA over the actuation cycle. It is desirable that the effective torque input increase is smaller so that the motor does not stall sooner. Γ decreases with increasing motor rotations showing that at smaller rotations, the TSA performs much better than SMTA.

Peak Performance

Firstly, the contraction ranges of the actuators were compared. The average displacement per unit rotation ($\Delta X/n$) was 2.63 cm/rotation and 0.047 cm/rotation for SMTAs and TSAs, respectively. Similar to $\hat{c}_{\mathrm{max}}$, as shown in Fig. 3.5(a), $\tilde{c}_{\mathrm{max}}$ decreased when the load was increased. When both the TSA and SMTA were constructed from the 10:1 gear ratio motor, TSA's $\hat{c}_{\mathrm{max}} = 30\%$ with loads up to 0.3 kg while the SMTA's $\tilde{c}_{\mathrm{max}} = 90\%$ with loads only up to 0.1 kg. When the load was 0.135 kg, $\hat{c}_{\mathrm{max}} = 30\%$ and $\tilde{c}_{\mathrm{max}} = 0\%$. In Fig. 3.5(a), the decrease in $\hat{c}_{\mathrm{max}}$ was due to a decrease in $\hat{n}$ — a limited number of motor rotations $\hat{n} \leq \hat{n}_{\mathrm{max}}$ were applied before $\hat{\tau}_{\mathrm{m}} \geq \tau_{\mathrm{ss}}$.

Secondly, $\dot{X}_{\mathrm{max}}/\dot{\theta}$ of the actuators were compared. Similar to TSAs, $\dot{\tilde{X}}_{\mathrm{max}}/\dot{\theta}$ of SMTAs in Fig. 3.5(b), showed that increasing the load decreased $\dot{\tilde{X}}_{\mathrm{max}}/\dot{\theta}$. For SMTAs, $\dot{\tilde{X}}_{\mathrm{max}}/\dot{\theta}$ of all motors had a range of 0–0.44 cm/rad. Although SMTAs attained higher $\dot{\tilde{X}}_{\mathrm{max}}/\dot{\theta}$, the ratios were attained at much lower loads than TSAs. For example, when the load was 0.09 kg and for the 30:1 motor, $\dot{\tilde{X}}_{\mathrm{max}}/\dot{\theta} = 0.44$ cm/rad and $\dot{\hat{X}}_{\mathrm{max}}/\dot{\theta} = 0.043$ cm/rad. When the load was increased to 0.11 kg, $\dot{\hat{X}}_{\mathrm{max}}/\dot{\theta}$ remained to be 0.043 cm/rad, but $\dot{\tilde{X}}_{\mathrm{max}}/\dot{\theta}$ became 0.

Thirdly, the effective torque inputs applied to the actuators were compared. Sim-

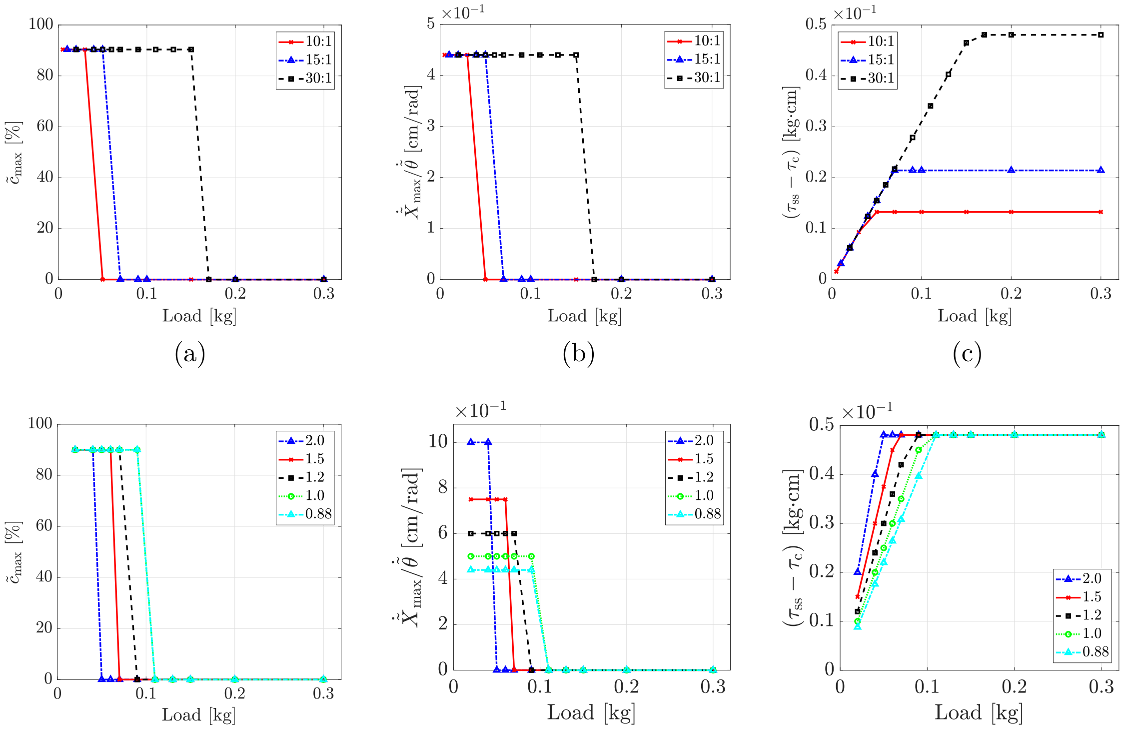

(a) (b) (c)

(d) (e) (f)

Figure 3.5: The performance of the SMTA where (a) Shows $\tilde{c}_{\max}$, (b) shows $\dot{\tilde{X}}_{\max}/\dot{\tilde{\theta}}$, and (c) shows $\tau_{ss} - \tau_c$ of SMTAs with three different motors at various loads. The effect of changing the diameter of the spool, $\tilde{d}$, on the performance of SMTA on: (d) $\tilde{c}_{\max}$, (e) $\dot{\tilde{X}}_{\max}/\dot{\tilde{\theta}}$, and (f) $\tau_{ss} - \tau_c$ of SMTAs constructed from using 30:1 motor at various loads.

ilar to TSAs, the effective torque input for SMTAs, shown in Fig. 3.5(c), increased linearly with increased load until saturations were reached. The effective torque input range was 0.0022–0.013, 0.0044–0.021, 0.0088–0.048 kg·cm for the 10:1, 15:1, and 30:1 motors in SMTAs, respectively. Although both actuators achieved similar maximum effective torque inputs, the rate of increase of effective torque per kilogram of load was 0.44 for SMTAs. A lower rate was desirable. These results indicated that TSAs were 2.6 times better than SMTAs in terms of the rate of torque increase per kilogram of load.

Lastly, the force outputs of the actuators were compared. Due to the higher rate of torque increase, SMTAs stalled at lower loads. This is observed in the critical force for TSA and SMTA. $\hat{F}_{\text{critical}}$ was 0.31, 0.50, 1.1 kg for the 10:1, 15:1 and 30:1 motors respectively whereas $\tilde{F}_{\text{critical}}$ was 0.03, 0.05, 0.11 kg for 10:1, 15:1 and 30:1 motors in SMTA. The maximum force outputs of the actuators also increased as the gear ratios increased for both TSAs and SMTAs.

In addition to comparison of the TSA and SMTA on the performance for each motor and load, comparisons for ratios on the maximum performance values for each load and motor were conducted. Fig. 3.4(c) and (d) shows the performance of the TSA when the maximum values were used to compute Φ_{max}, Λ_{max}, Γ_{max}, Ψ_{max}. Since Γ has a singularity when $\theta = 0$ (see Eq. (3.25)), Γ_{max} was computed when $\theta = \hat{n}_{\text{max}}$. As shown in Fig. 3.4(c), Φ_{max}, Λ_{max} were always less than unity for all motors, demonstrating that SMTA had a better performance in linear contraction and linear velocity. However, Ψ_{max}, Γ_{max} as shown in Fig. 3.4(d), were always greater than unity for all tested motors demonstrating that TSA had a better performance in force production and effective torque input for all the motors tested. Further, Φ, Ψ, Γ, Λ are consistent for all motors, demonstrating that there is minimal dependence on motor characteristics for the findings in this study.

Effect of Spool Diameter on SMTA Performance

Increasing $\tilde{d}$ decreases $\tilde{F}_{\text{critical}}$. Consequently, an increase in $\tilde{d}$ results in the motor attaining stall quicker (Fig. 3.5(d)–(f)). When $\tilde{d}$ was increased from 0.88 cm to 2.0 cm, $\tilde{F}_{\text{critical}}$ decreased. As shown in Fig. 3.5(d), $\tilde{c}_{\text{max}}$ is similar, with the load to achieve stall being lower. In Fig. 3.5(e), increasing $\tilde{d}$ increases $\dot{\tilde{X}}_{\text{max}}/\dot{\tilde{\theta}}$. This is to be expected as increasing $\tilde{d}$ increases the linear speed. Finally, as validated with the simulation in Fig. 3.5(f), $\tilde{d}$ is directly proportional to $\tau_{\text{ss}} - \tau_{\text{c}}$.

3.6 Experimental Results

3.6.1 Experimental setup

As shown in Fig. 3.6, the experimental setup for both TSAs and SMTAs consisted of a rectangular aluminum frame, with the motor fixed at the top. The TSA and SMTA were constructed from the MM motor with a gear ratio of 30:1 (Pololu: 3072). The nominal voltage was 6 V, $\dot{\theta}_{\text{fr}} = 1100$ RPM, and $\tau_s = 0.450$ kg·cm. To prevent damage to the motor, a DRV8871 motor driver limited the current draw of the motor to be 20% of its stall current. The motor's speed was adjusted using pulse-width modulations (PWM). An Adafruit INA260 sensor was used to measure the motor's current. The displacement was measured using a magnetoresistive position sensor (Honeywell SPS-L225-HALS). The magnet and its holder, used to track the strain, had a mass of 20 g. One end of the strings was attached to the motor and the other end was attached to the magnet assembly, which was then attached to the payload. The friction between the magnet holder and the frame was assumed to be negligible. In this study, $\tilde{d} = 8.8$ mm, $\hat{s} = 7.7$ mm, $r_0 = 0.15$ mm, and $\hat{L} = \tilde{L} = 18.4$ cm.

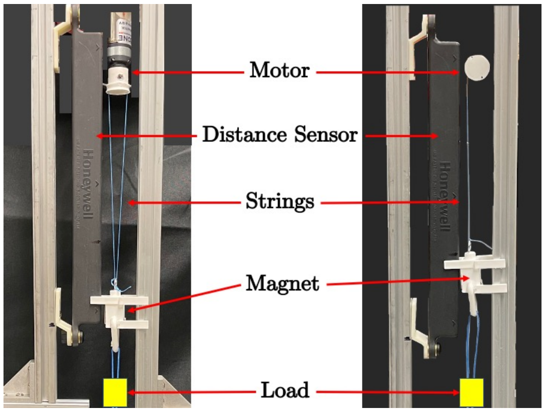

Figure 3.6: Experimental setup with (left) TSA and (right) SMTA.

3.6.2 Procedure

Firstly, a small load was attached to a given actuator. Secondly, three cycles of motor twisting input sequence consisting of monotonically increasing followed by monotonically decreasing rotations was applied to the actuator. Thirdly, the load was increased and the procedure was repeated until the motor stalled. $n_{\max}$ applied to the TSA and SMTA were determined experimentally such that $c_{\max}$ were approximately 30% and 90% at their lowest loads, respectively.

3.6.3 TSA performance

TSA exhibited $\hat{c}_{\max}$ approximately 30% for loads up to 1.2 kg and 16% under a 1.4 kg load (Fig. 3.7(a)). The SMTA exhibited $\tilde{c}_{\max}$ of 90% at low loads, which decreased as the load was increased — when the load was 0.148 kg, the contraction was 70%. This decrease in contraction may have been due to slight unwinding of the string from the spool due to the relatively heavy loads that induced torques on the motor's shaft. When the load was beyond 0.158 kg, the motor would not rotate. The TSA was able to actuate around 8 times the maximum load that the SMTA could actuate.

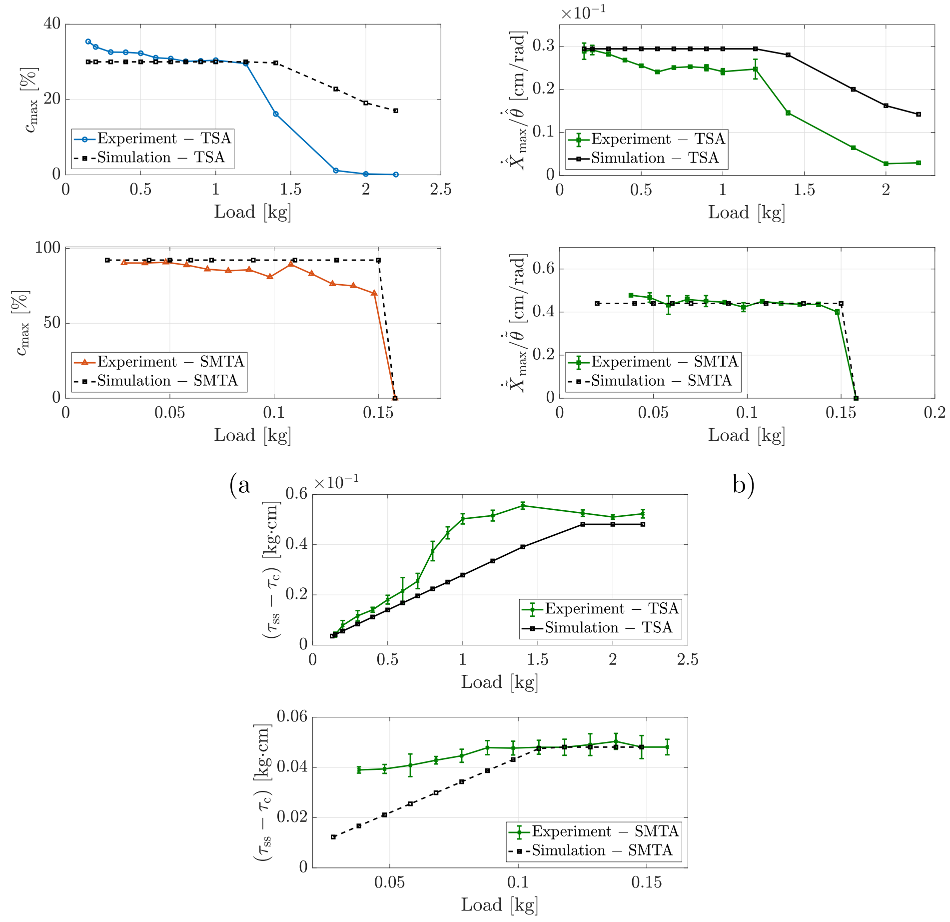

(a b)

(c)

Figure 3.7: Comparison of experimental and simulated results of TSA and SMTA made with a 30:1 gear ratio motor where (a) is contraction, $c_{\max}$, (b) velocity ratio, $\dot{X}_{\max}/\dot{\theta}$ and (c) effective torque, $\tau_{\text{ss}} - \tau_{\text{c}}$.

$\dot{X}_{\max}/\dot{\theta}$, and $\tau_{\text{ss}} - \tau_{\text{c}}$, for TSA and SMTA is shown in Fig. 3.7(b) and Fig. 3.7(c) respectively. The linear velocity was computed using a finite impulse response differentiator of order 50. The torque was computed by multiplying the measured current by the motor's torque constant of $k_\tau = 0.323$ kg·cm/A, which was estimated from the manufacturer's datasheet [92]. $\dot{\hat{X}}_{\max}/\dot{\hat{\theta}}$ of the TSA was 0.0013–0.028 cm/rad. $\dot{\hat{X}}_{\max}/\dot{\hat{\theta}}$ for the SMTA range was 0–0.478 cm/rad. Thus, the SMTA exhibited $\dot{X}_{\max}/\dot{\theta}$ of more than an order of magnitude than that of the TSA but at much lower loads.

$\tau_{\text{ss}} - \tau_{\text{c}}$ range was 0.0042–0.056 kg·cm for TSA. For SMTA, $\tau_{\text{ss}} - \tau_{\text{c}}$ range was 0.039–0.0503 kg·cm. When the load was 0.15 kg, $\dot{\tilde{X}}_{\max}/\dot{\tilde{\theta}} = 0.30$ cm/rad and $\dot{\hat{X}}_{\max}/\dot{\hat{\theta}} = 0.027$ cm/rad; $\tau_{\text{ss}} - \tau_{\text{c}} = 0.048$ kg·cm for SMTA and $\tau_{\text{ss}} - \tau_{\text{c}} = 0.0042$ kg·cm for TSA. The observed fluctuations in $\dot{X}_{\max}/\dot{\theta}$ may have been due to the noise from current measurements or differentiating the linear position measurements.

The efficiencies were computed from experimental data where the SMTA exhibited higher efficiency compared to TSA. When the load was 1 kg, the efficiency was 67% for TSA and when the load was 0.1 kg, the efficiency was 95%

3.7 Discussion and Conclusion

$\tau_{\text{ss}} - \tau_{\text{c}}$ demonstrated good alignment of simulation with experiment. In simulation, the TSA and SMTA both showed maximum effective torques of 0.048 kg·cm. In experiments, the TSA and SMTA showed maximum effective torques of 0.056 kg·cm and 0.050 kg·cm respectively. The slightly higher experimental results could have been a result of underestimating the Coulombic friction of the motor.

The experimental results and the simulation results show good agreement for the ratio $\dot{X}_{\max}/\dot{\theta}$. The TSA and SMTA maximum $\dot{X}_{\max}/\dot{\theta}$ in the experiment were 0.498 cm/rad and 0.028 cm/rad, respectively, for the 30:1 motors. In simulation, as shown in Fig. 3.3(b) and Fig. 3.5(b), the 30:1 motors exhibited $\dot{X}_{\max}/\dot{\theta}$ of 0.44 cm/rad and 0.043 cm/rad for the SMTA and TSA, respectively. $\dot{\tilde{X}}_{\max}/\dot{\theta}$ is slightly high initially since at the low loads, the SMTA exhibits higher rotational speeds which likely introduced measurement errors. $\dot{\tilde{X}}_{\max}/\dot{\theta}$ then became approximately 0.42 cm/rad. However, $\tilde{c}_{\max}$ for SMTA showed some discrepancies in simulation and experiment. In experiment, as shown in Fig. 3.7(a), the SMTA showed a mildly varying contraction as the load increased for the 30:1 motor — a contraction range of 90% at low loads, which decreased to 70% when the load was 0.148 kg. The contraction further decreased to 0% when the load was greater than 0.148 kg. In the simulation, the 30:1 motor showed a contraction of 90% at low loads until a load of 0.09 kg was achieved. The contraction decreased to 0% with loads greater than 0.11 kg, as shown in Fig. 3.5(a). The difference between the simulated and experimental results may have been due to the assumption of infinite string stiffness, and the noise from the sensors and data processing. It may have been due to the sensitivity of existing TSA models to the string radius [74].

A part of the aforementioned analysis has been utilized to design a wearable robotics glove [78] where considerations such as range of motion (ROM) for finger closing, minimum speed of the actuation, sufficient grip force were critical. Specifically, for the design of the glove the selection criteria was as follows; (1) Actuation mechanism should provide a sufficient range of motion (ROM) for complete finger closing; (2) The minimum speed of the actuation mechanism must result in finger motion speed comparable to nominal values; (3) Sufficient grip strength should be obtained; and (4) The actuation mechanism drive and control units can be easily attached to the forearm. (1) is related to the contraction range of the actuation mechanisms, (2) is the linear velocity, (3) is the force output and (4) is related to the configuration of the actuation mechanism. It can be shown that SMTA and TSA both satisfy (1), (2) but only TSA satisfy (3) and (4). As a result, for the glove TSA were used as the actuation mechanism.

It is important to note that in TSAs, the contraction and payload drive the stress experienced by the strings. At high contraction and lower loads, TSAs are expected to exhibit different lifetime than low contraction at high loads. TSAs are expected to have lower lifetime as compared to SMTAs. A detailed experimental analysis on the string lifetime in TSAs has been conducted in this study [94].

In this chapter, a model-based framework that allows for the analysis of key performance metrics of TSAs is proposed. Further, the performances of TSAs were compared with SMTAs in terms of linear contraction, linear speed, force output, and effective torque input. The performance comparisons were conducted in simulations and experiments, using TSAs and SMTAs constructed from the same type of motors. The results indicated that TSAs performed better in terms of force output and effective torque input, whereas SMTAs performed better in terms of contraction ranges and speeds. The findings were consistent both in simulations and experiments. Future work will include more accurate modeling that considers the finite stiffness of the strings and more types of motors and strings. Additionally, the performance of SMTAs and TSAs will be compared in practical application where the performance of a robotic device driven by an SMTA and a TSA using the same type of motor will be compared.

Part II

Design and Characterization of Devices

CHAPTER 4

TSA-BRAG

4.1 Introduction

BRAG is a Biomimetic Robotic Assistive Glove that is driven by TSAs. TSAs remove the need for rigid linkages and TSA-based devices can be untethered and powered by a battery. The goal of this work was to reduce the number of rigid components, ensuring that the system was compliant and soft.

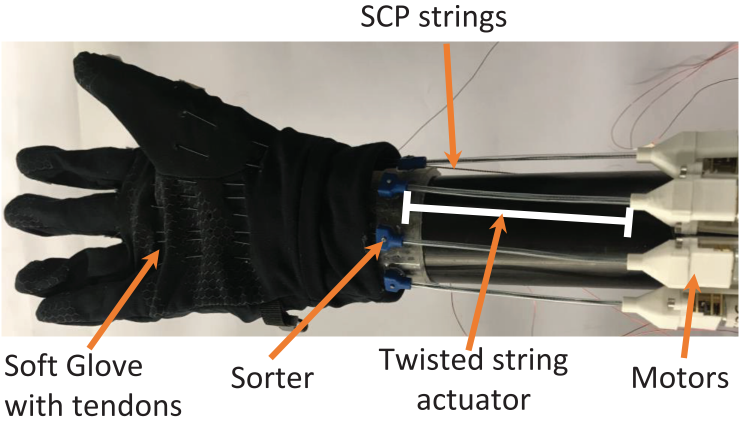

Figure 4.1: BRAG is actuated by 4 TSAs is shown being worn by a 3D-printed hand model. SCP strings are installed on the dorsal side of the glove.

BRAG was designed, and controlled to pick everyday objects by using a passive robotic hand (Fig. 4.1). In BRAG the variable length TSA was implemented, eliminating the rigid railing system. The assistive device used SCPs for sensing and passive actuation. The SCPs are characterized to show their capabilities in sensing, and showing consistency over multiple cycles. This work also showed the evolution of the resistance of the SCPs as the picking progresses. Repeating picking tasks allows for the evaluation of the consistency of position sensing and the quantification of the robot glove performance in successfully assisting tasks.

Additionally, the choice of actuators is informed by the detailed comparisons of TSA and spooled-motor configuration performed in Chapter 3. Due to limited studies that quantify TSA performance over spooled-motor configurations, it is challenging to find motors to optimize footprint, torque and speed. Further, SCP strings were used for both sensing and passive force for restoring fingers to open palm position. Finally, our work limits the use of rigid components in the palm to minimize interference with sensations during object manipulations.

4.2 Design Considerations

Considerations of TSA-BRAG were as follows: (1) TSAs should provide a sufficient range of motion (ROM) for complete finger closing; (2) The minimum speed of TSAs must result in finger motion speed comparable to nominal values; (3) Sufficient grip strength should be obtained; and (4) The TSA drive and control units are compact and can be easily attached to the forearm.

TSA-BRAG was designed so that it exhibited a combination of compliance, strength, and compactness attributes. The design considerations from the previous paragraph had the following basis and implications for the proposed TSA-BRAG system:

First, the range of motion should be sufficient to lead hand to fully close. Full hand-close will enable BRAG to perform effective motion generation and object grasping. The ROM was obtained based on the kinematics of the fingers. Specifically, the displacement of each phalange from straight position and joint angles can be measured.

The functional angular ROM of phalanges are often chosen between 0° and 73°, 86°, 61° for metacarpophalangeal (MCP), proximal interphalangeal (PIP) and distal interphalangeal (DIP) respectively [95]. The diameters of the MCP, PIP, DIP are chosen as 30 mm, 20 mm, and 15 mm respectively. The ROM for all fingers was computed using the maximum angles for the three finger joints (MCP, PIP, DIP) and the diameters of the different fingers. Taking the measurements from the central axis of the fingers, the tendon length change is driven by the rotational angle and the thickness of the finger [96]. This approach captured the tendon change for every rotation. In BRAG, the ROM was determined to be between 4-8 cm, for different fingers of a medium-sized male.

Second, hand close motion for all fingers must not be unnatural or take too long to execute. Human beings produce finger movements that are in the range of 2–12 Hz [97]. A frequency of 0.33 Hz during hand closing was selected for this work. This frequency is equivalent to 3 seconds for fully closing the hand. The linear and rotational speeds of the motor was determined by using the spool radius for use in BRAG design.

Third, the grip strength must be sufficient. Sufficient grip strength will enable performance of wide range of ADL, augmentation of strength, or rehabilitation tasks.

Fourth, the system should be compact, comfortable and not completely block sensations. Compactness is essential in ensuring that users can comfortably use the glove for an extended period of time. Taking into account the forearm length and the maximal ROM, the minimum contraction from the TSA is computed. Users should still be able to perceive partial sensations with the usage of soft glove.

4.3 BRAG Device Design

The BRAG system, shown in Fig. 4.1, was based on the Red Stone Gloves (Amazon: B06ZY5G3ZC). The glove was selected for its softness, comfort and breathability. The thin fabric of the glove allowed for sensations to be picked by the hand even when the glove was worn. Previous designs have opted to leave the fingertips uncovered by the gloves to ensure that the sensations were not affected [98]. In this approach, however, thin fabric was chosen so that the user could have a consistent and partial haptic feedback when the glove was in use.

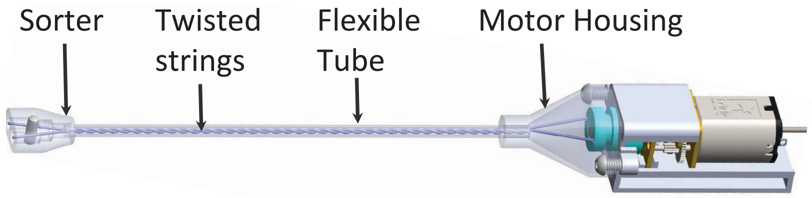

Figure 4.2: TSA single motor assembly, showing the sorter and the flexible tube that houses the strings in the twisting zone.

Fig. 4.2 shows one TSA assembly. A flexible tube covers the twisting zone, ensuring that there was no interference during operation or avoid irritation with the skin. The motion from the TSAs to the user's fingertips was transferred by the strings embedded in the glove. The strings were manually embedded into the glove with consistent spacing. While the symmetry of the embedded strings was important, given how thin and deformable the glove material was, the precision became less consequential. Fig. 4.3(a) shows the fabric stretch due to the strings when the TSA was contracting. Moving the strings to the outside of the glove, as shown in Fig. 4.3(b) did not alleviate the issue. Fig. 4.3(c) and (d) show the solution — by adding nylon plates at the dorsal side of the fingers, the fabric deformation was solved. The nylon also minimized the friction experienced by the routed tendons. This ensured that when grasping, the fingers would be performing the grasp and not the tendons. The twisting zone was also fitted with a flexible tube to ensure that there was no irritation on the users skin during usage.

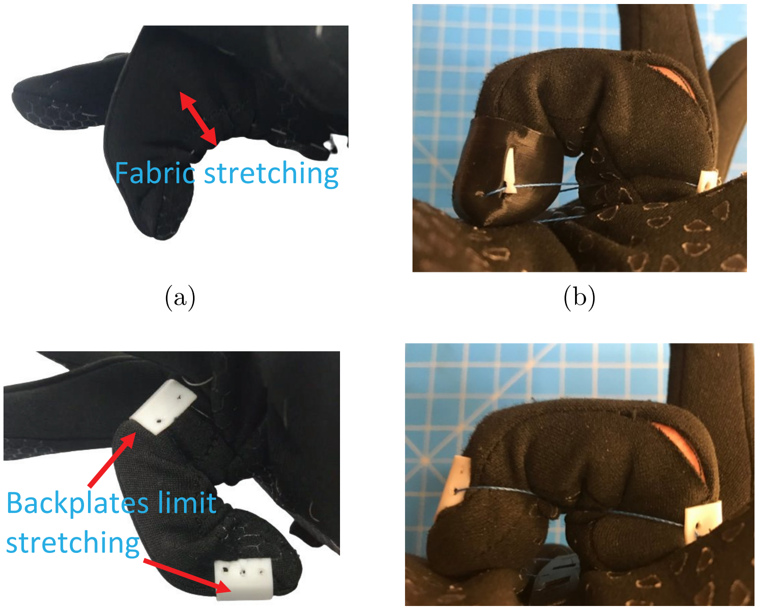

(a) (b)

(c) (d)

Figure 4.3: (a) Stitch and embedding that resulted in the fabric stretching when force is applied to tendons. (b) Strings attached using thermoplastic polyurethane at the fingertip show interference with the grasping. (c) Improved design of embedding showing limited fabric stretch with the use of backplates. (d) Using the backplates alleviates issue even when the strings are not embedded in fabric.

The system was also fitted with an SCP string on the dorsal side of each finger for measuring the distance changes for a better estimation of the pose of the assistive glove. Previous work has shown that resistance can be used to track the length of an SCP actuator [99, 100], with a demonstration on implementation on a grasper [60]. More information on the sensing performance of the SCP strings and the characterizations of the force production are available in section 4.5.1.

The actuation unit was attached to the forearm region using two elastic velcro straps that could be adjusted to fit the forearm of the user. These bands held to the arm tightly enough to resist the contraction force produced by the TSA and keep the system mounted on the user's arm. The 4 TSAs were able to fit on the forearm, as shown in Fig. 4.1 where BRAG is worn by a 3D printed robotic passive hand.

4.4 TSA Design

4.4.1 Choice of TSA configuration

To achieve this, TSAs with variable string length with a sorter mechanism were adopted, as shown in Fig. 4.2. The sorter was placed between the load and the motor to change the length of the twisting zone of the string. Twisting will only occur between the motor and sorter. It was important that the sorter exhibit minimal friction with the strings. A metal rod was implemented at the site of sorting the strings which minimized the friction. The separation between the motor and the sorter changed the length of the twisting zone. This strategy allowed for the removal of the rail for spacer travel, and further allowed for the ease of adjustment of travel. The flexible tube can be easily changed by sliding out the sorter, allowing for a length modification to accommodate different twisting zone lengths. The design made it easier to have the glove comfortably fit for people with different forearm sizes. In this study, KastKing braided fishing lines (KastKing: KLIBRDSP-327YBL40) were used due to their strength and resistance to abrasion.

4.4.2 Adjustment of the twisting zone

The choice of TSA architecture was driven by the goal of having a setup that could have the twisting zone changed on demand. This design adaptability allowed for

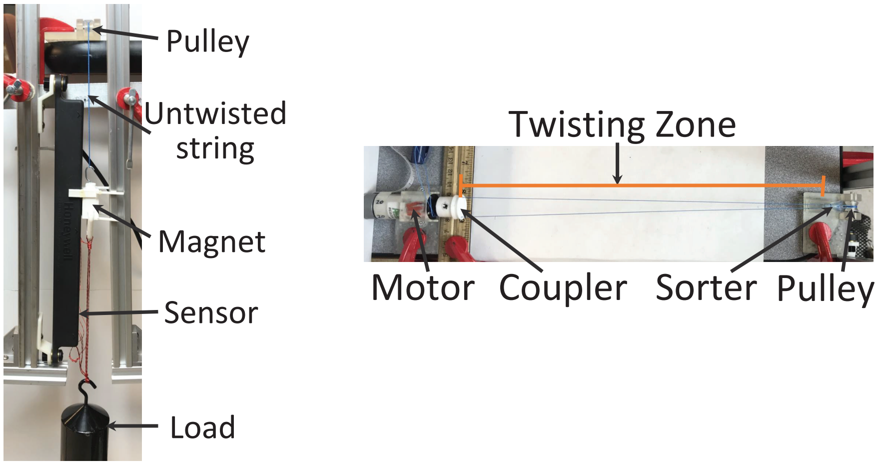

(a)

(b)

Figure 4.4: Twisting zone test experimental setup. Test were performed under the same load, with only the twisting zone varied. (a) front view, and (b) top-view of the setup.

BRAG to be used easily with users who have different requirements. As a result, an investigation was performed to determine the behavior of the displacement as the twisting zone changed. Six twisting zones were tested, with the displacement and the motor rotations recorded. Fig. 4.4 is a depiction of the experimental setup. The position sensor (Honeywell SPS-L225-HALS) was used to measure the displacement during twisting. This sensor had a sensing range of 225 mm and resolution of 0.14 mm. It used magnetoresistive arrays to determine the position of a magnet that was affixed to a translating object. A magnet assembly, consisting of a holder and a magnet, was attached to the end of the strings. The sensor positions were acquired with ADS1115 16-Bit ADC through the Arduino, which also kept track of the rotations of the motor and time duration. All twisting experiments were performed under the same load.

The contraction for each twisting zone was also computed to show what the behaviour was for the different twisting zones. The contraction was obtained by measuring the total linear displacement of the load, where the contraction was defined

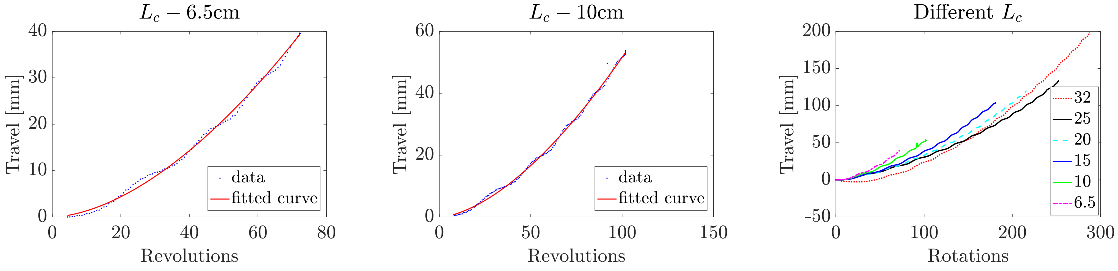

(a) (b) (c)

Figure 4.5: (a) The displacement behavior when the twisting zone is set to 6.5 cm (b) when the twisting zone is 10 cm and (c) displacement for TSAs with different twisting zones. For all cases, the 30:1 motor was used for running the test.

as

$$\Delta p = \frac{p_{\mathrm{f}} - p_{\mathrm{i}}}{L_{\mathrm{t}}} \times 100\%, \tag{4.1}$$

where p_i was the initial position of the magnet, p_f was the final position of the magnet and L_t was the length of the twisting zone summed with the maximum possible travel. When the twisting zone was 32 cm, the maximum possible travel was the length of the magnet sensor, 225 mm. As the twisting zone decreased, so did the maximum possible length of travel, as shown in Fig. 4.5 – (a) and (b) show that the range and the number of rotations were increased as the twisting zone increased. Fig. 4.5(c) shows that for all the tested twisting zones, the range increased as the twisting zone was increased. Further, Table 4.1 shows the increasing range as the twisting zone was increased.

Table 4.1: Parameter identification results for load displacement for fixed twisting zones, where $\mathrm{f}(x) = \mathrm{a}x^{\mathrm{b}}$ with x = rotations.

L_c [cm]	a	b	error [mm]	Range [mm]
6.5	0.02578	1.713	0.4437 ± 0.3744	39.6141
10	0.02766	1.635	0.5225 ± 0.4308	53.6414
15	0.01594	1.689	0.5473 ± 0.5166	103.6441
20	0.01432	1.679	0.9425 ± 0.6166	119.7387
25	0.01606	1.630	1.3387 ± 0.7457	133.0488
32	0.00239	2.002	1.4344 ± 1.2027	199.5258

4.5 BRAG System Design

4.5.1 Hardware design

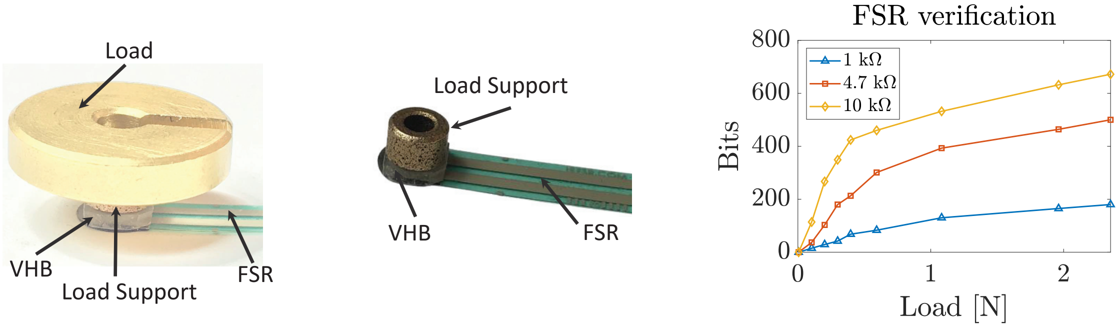

(a) (b) (c)

Figure 4.6: Force testing (a) FSR testing setup, (b) FSR testing setup without any load applied. (c) FSR testing results for different reference resistances.

The choice of the sensors to be used for TSA-BRAG was driven by the overall goal of realizing a compact and compliant system. Two sensing inputs were considered, namely force sensing and displacement sensing. More details on the sensing input considerations are presented:

1. **Force Sensing** — The force sensitive resistor (FSR) (Pololu: 1695) was adopted for force sensing for its compactness. The sensitivity was dependent on the reference resistance used in the voltage divider that connected to the FSR. Three reference resistors were tested. While decreasing the reference resistance increased the sensitivity at low loads, the lowest reference resistor made it harder to discern any difference in the applied force and noise. In addition, the performance of the FSR also depended on the type of surface in contact with the sensor. A rigid object contact performed poorly. Fig. 4.6(a) and (b) show the setup for testing with very high bond (VHB) double sided tape (McMaster:

76665A88) incorporated to improve the performance during testing. The results are shown in Fig. 4.6(c). The sensors were tested for their performance prior to being incorporated to the assembly.

2. **Displacement Sensing** — To determine the pose of the assistive device, SCP strings were chosen. The flex sensor was not used due to the increased width, which may complicate the integration. Furthermore, the SCPs are elastic and deformable — elasticity allowed SCPs to act as a spring. This added benefit meant that there was no need for an additional passive actuator for finger extension. To effectively utilize SCP strings in the assistive glove, three properties were essential:

    (a) *Sensing range* — The sensing range has to be comparable to the maximum ROM of the fingers. This ensured that position of the finger could be tracked throughout the entire ROM.

    (b) *Nature of the behavior* — Understanding whether the correlation between stretch and resistance was hysteretic or not would help with better implementation. Controlling hysteretic systems composed of smart materials require an involved controller design and compensation [101].

    (c) *Force production* — The force produced by the SCP string was important for two reasons: (1) the magnitude of the force should be small enough such that minimal residual forces were transmitted to the fingers of the users, making the experience uncomfortable over long periods of usage. (2) The force should be high enough so that it was capable of overcoming the force from extending the fingers and restored fingers to straight neutral position.

The following experiments were performed for the characterization of the SCP

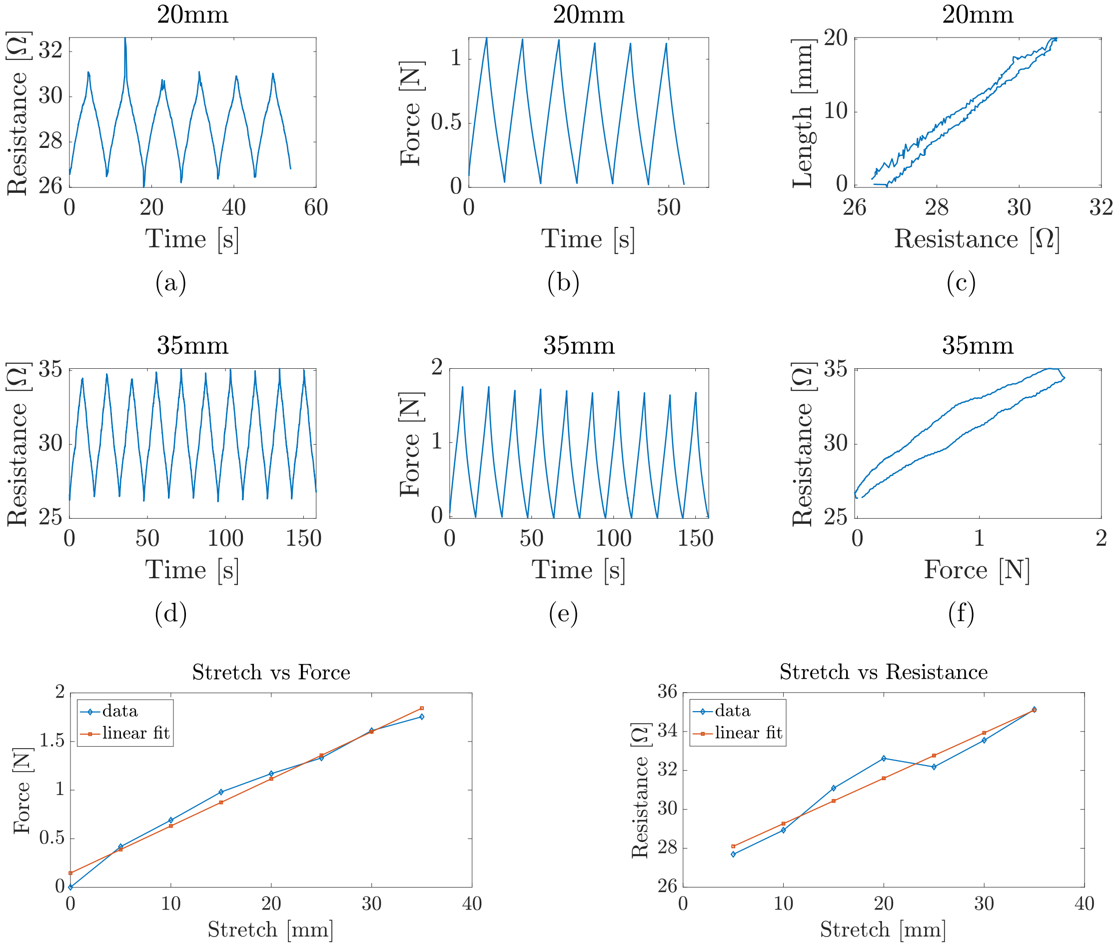

(a) (b) (c)

(d) (e) (f)

(g) (h)

Figure 4.7: The variation of SCP string properties as it is stretched. (a) The resistance change under stretching to 20 mm stretch for 6 cycles (b) force changes with times when performing stretching for 6 cycles. (c) The relationship between resistance and length. (d) The resistance variation when the SCP string is stretched to 35 mm and repeated for 10 cycles. (e) The transient force behavior of the SCP during stretching. (f) The force and resistance behavior for the SCP string when stretched to 35 mm. (g) The average maximum force for each stretch performed and (h) The average maximum resistance changes when the SCP has been stretch to different lengths.

string. The distal end of the SCP string was attached to a load cell (LSP-2, Transducer Techniques), while the other end was attached to the bottom of a magnet holder of the position sensor (Honeywell SPS-L225-HALS). While the motor was activated in the spooled-motor configuration, the SCP string stretched. The magnet allowed for the tracking of the position and the load sensor allowed for force measurements. The load and resistance values were collected using an Arduino Mega. The stretch and the force of a 3-ply SCP string were measured simultaneously as the SCP string was stretched to different lengths from 5 mm to 35 mm. Each step of the stretch increase was repeated five times. The un-stretched length of the SCP string was 21 cm and the diameter was 0.81 mm.

The results from these tests are shown in Fig. 4.7; (a) shows the the variation of resistance over time for a stretch of 20 mm, with (b) showing the force variation over time and (c) showing the resistance change as the stretch was induced. Fig. 4.7(d)–(f) shows the resistance variation with time, force variation with time and resistance change as force was increased for the stretch of 35 mm. The data shows that for each stretch, the resistance was stable for the 5 repeated cycles. In addition, the resistance–length behavior was mildly hysteretic hysteric. The force–resistance also exhibited hysteresis. Further, it demonstrates that the force generated will not be too high to induce discomfort during usage. These findings demonstrated that the SCP strings can be reliably used for sensing by monitoring the resistance changes. Fig. 4.7(b) and (e) show that the force was also stable for the repeated cycles. In addition, Fig. 4.7(g) and (h) shows the aggregated force and resistance for different stretches, respectively. Linear models were fitted for both and the model parameters are shown in Table 4.2. The force–stretch showed a linear positive correlation — as the force was increased so did the stretch, with the maximum force being 1.7 N. Fig. 4.7(h) shows the change in resistance as the stretch was increased. The resistance–stretch correlation also shows a linear behavior. The range was 8 Ohms for this SCP string.

Table 4.2: Represents the parameters identified from the aggregate force and resistance.

Type	p_1	p_0	error	Range
Force	0.0485	0.1461	0.0653 ± 0.0455	1.7548
Resistance	0.2332	26.9343	0.4892 ± 0.3082	35.1300

4.5.2 Electrical design and control

BRAG v1

The fingers could be controlled in two modes to generate motions and complete grasping tasks: 1) fingers were activated sequentially, one finger after the other until the hand accomplished a fist configuration; 2) all fingers were actuated at the same time. The design consisted of 4 TSAs. The number of TSAs was chosen such that a wide range of grasping configurations could be obtained and enough independence was achieved among all fingers. The thumb, index, and middle fingers had independent controls as they were the dexterity fingers and required separate actuation to complete common ADL and tasks [102, 103, 104]. Then the ring and pinkie fingers were coupled together.

BRAG was driven by TSAs with 30:1 gear motors (Polulu: 3072) for two reasons: 1) the motor was lightweight and the footprint was small. It had a cross-section of 10×12 mm and a depth of 40 mm; 2) the load range was bigger for contraction above 25 %. The motors were fitted with magnetic encoders (Polulu: 3081). Arduino Mega was used to read the encoder data and the motors were driven by an Adafruit Motor Shield (Adafruit product 1438). In this study, the motors ran off a power supply; however, the system will be battery-powered in future studies.

BRAG v2

The fingers can be controlled in two modes to generate motions and complete grasping tasks: (1) fingers were activated sequentially, one finger after the other until the hand accomplished a fist configuration; (2) all fingers were actuated at the same time.

The design consisted of 4 TSAs. The number of TSAs was chosen such that a wide range of grasping configurations could be obtained and enough independence was achieved among all fingers. The thumb, index, middle and ring fingers had independent controls as they were the dexterity fingers and required separate actuation to complete common ADL and tasks [102, 103]. The little finger was not actuated.

BRAG was driven by TSAs with 30:1 gear motors (Polulu: 3072). The motors were fitted with magnetic encoders. Arduino Nano was used to read the encoder data and the motors were driven by an Adafruit Motor Shield (Adafruit product 1438). In this study, the motors ran off a power supply; however, the system will be battery-powered.

BRAG follows the general control scheme shown in Fig. 4.8. By modifying the desired resistance, the glove will track changes in resistance. The stretch for a given resistance ($S(R)$) was obtained by inverting the model obtained from stretching data as shown in Fig. 4.7(h), with parameters shown in Table 4.2. For the SCP tested,

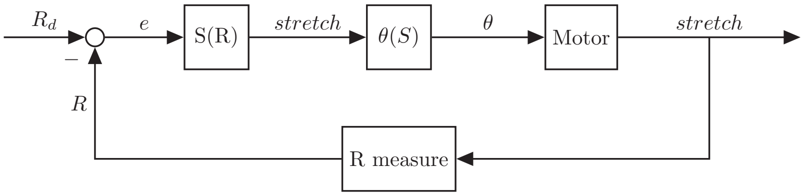

Figure 4.8: Control Scheme. $R(S)$ and $S(\theta)$ were obtained from experimental data. $S(R)$ and $\theta(S)$ are an inversion of those models.

$S(R) = \frac{R-28.9343}{0.2332}$. This is obtained from experiments. To obtain the required number of motor rotations of the desired stretch, a model was identified using the displacement and motor rotations behavior, $S(\theta)$. Intuitively, this model will depend on the twisting zone. Fig. 4.5(a)-(c) shows the differences in the behavior of the displacement profile for increasing twisting zone. Fig. 4.5(a)-(b) shows the travel profile for two different twisting zones, and Fig. 4.5(c) shows the behavior of the displacement profiles for all the twisting zones that were tested. Parameters for models that fit the data were identified and shown in Table 4.1. The error is small, considering the range of the displacement. As shown in the motor experiments in Fig. 4.9(e), the contraction for the string used was 40%. This information was used to set the twisting zone to 10 cm for the glove. For the desired twisting zone, $\theta(S)$ was obtained by inverting $S(\theta)$. When the twisting zone was 10 cm, $\theta(S) = \frac{S}{0.02766}^{\frac{1}{1.635}}$. Following this scheme allowed for the usage of a remote hand, with BRAG mimicking the movement of the hand. To show consistency in the resistance measurements for a better control implementation, the desired resistance was fed through using a button. Using the button allowed for the performance of the picking test for five times for each pick while keeping track of the resistance for each pick.

4.6 Experiments

4.6.1 BRAG v1

To test the performance of the proposed TSA-BRAG system, three sets of experiments were performed, namely, motion generation, grasping with a 3D printed robotic hand, and tests with an able-bodied wearer. The experimental results are shown in Fig. 4.10.

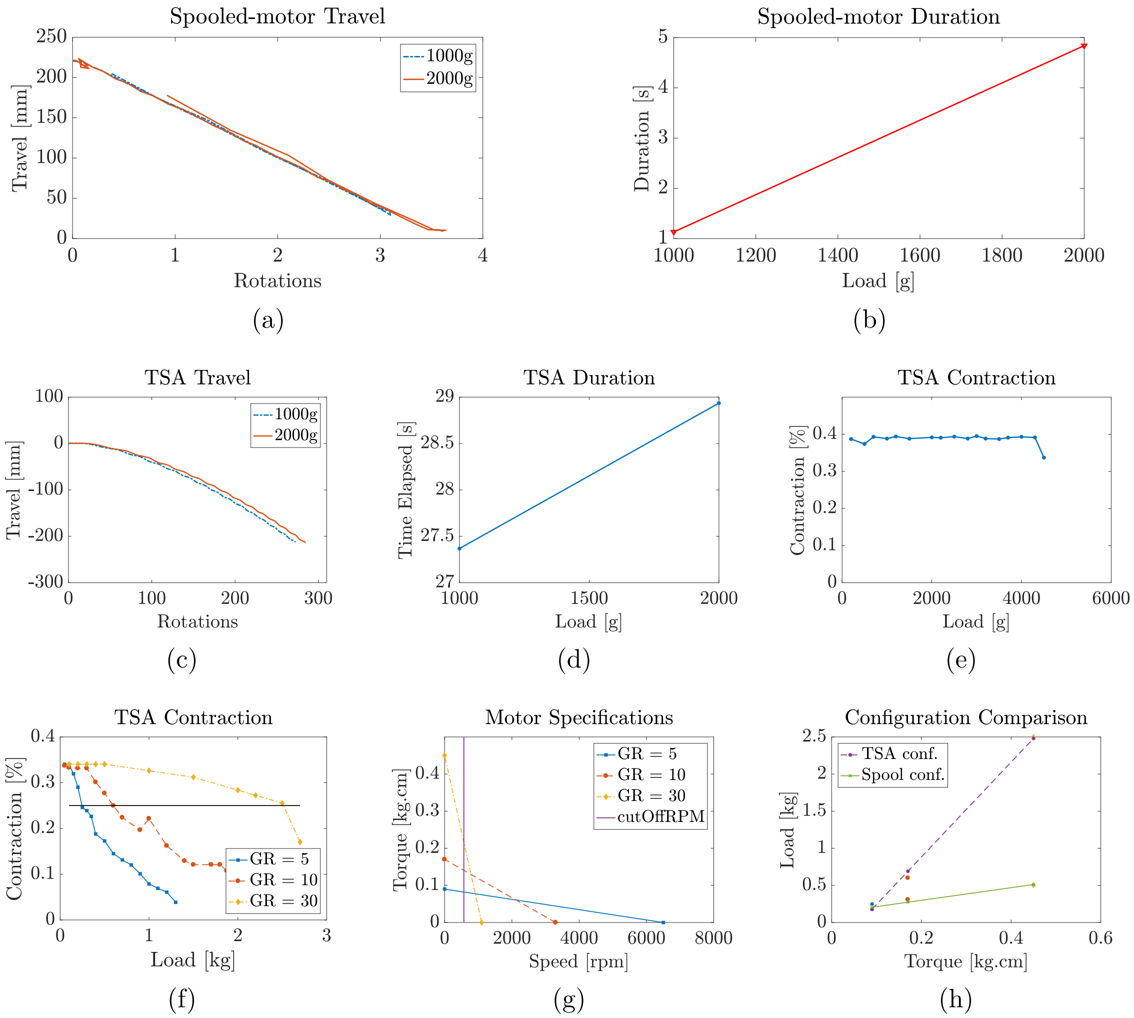

Figure 4.9: (a) A schematic for the spooled motor test setup. (b) The transient travel behavior using the spooled-motor configuration. (c) The variation of the time to complete the travel for the specified loads. (d) The travel of the TSA configuration for two loads. (e) The time duration that elapsed for the loads that are tested in the TSA configuration and (f) shows the contraction performance over varying loads. The 20:1 GR motor was used for the data presented in (a)-(f). (g) The contraction of the motors under different load conditions. (h) Motor specification, no load speed and stall torque for motors (i) Performance comparison of spooled and TSA configuration for motors.

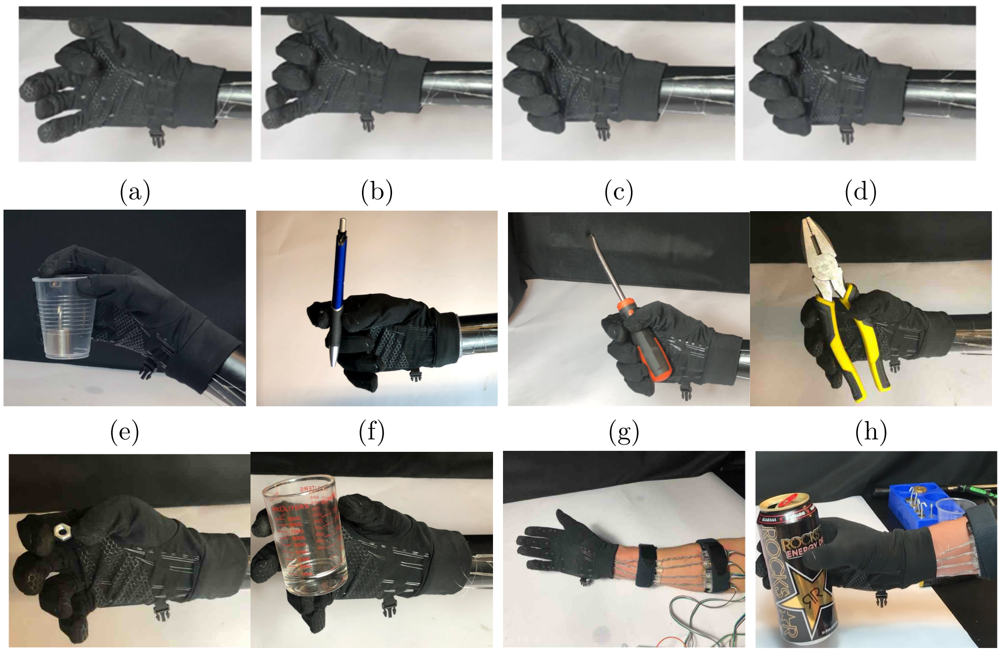

(a) (b) (c) (d)

(e) (f) (g) (h)

(i) (j) (k) (l)

Figure 4.10: (a)-(d) demonstrate hand close sequence, first step on the left and progressing rightwards, demonstrating the independent control of each finger. (e)-(j) Everyday object that were successfully picked using TSA-BRAG on a 3D printed robotic hand. (k) BRAG fitted onto an able-bodied user. (l) An able-bodied wearer conducted grasping tests with assistance from the TSA-BRAG system.

The first set of experiments demonstrated that motions could be achieved with the assistive glove on a 3D printed robotic hand, as shown in Fig. 4.10(a)-(d). This experiment was separated into two modes. The first mode consisted of actuating all fingers at once, generating a grasping motion used for power grasping or picking up large objects like a cup or pliers. The second mode actuated all fingers individually, one actuator at a time, to demonstrate individual motion of the fingers. This strategy could be important to perform tasks like picking up small objects or typing.

The second set of experiments demonstrated the ability to pick up common objects with the 3D printed robotic hand, as shown in Fig. 4.10(e)-(j). With TSA-BRAG worn by the 3D printed hand model, everyday items were picked up, including a plastic cup, a pen, a screwdriver, pliers, a small nut, and a glass cup. The heaviest object picked up was the pair of pliers (430 g), though the max grip strength was likely much higher since the TSAs had shown to be capable of lifting up to 2500 g.

The third set of experiments demonstrated that the TSA-BRAG device could assist motion to an able-bodied person's hand without the person activating their muscles, as shown in Fig. 4.10(k)-(l). An electromyography (EMG) sensor attached to the user showed that there was negligible signal changes during finger motion aided by the TSA-BRAG device. Therefore, no force was exerted by the muscles of the human subject during the test. The TSA-BRAG further assisted the wearer to grasp an empty can. This demonstrated the ability of TSA-BRAG in cases such as object grasping, force augmentation, and rehabilitation. The human study conducted in this study was approved by the Institutional Review Board at the University of Nevada, Reno.

4.6.2 BRAG v2

Fingertip force measurements

The first performance metric to be characterized is the fingertip force. The fingertip force is an essential measure of calibrating the amount of force that assistive gloves can produce and how successful they will to perform activities of daily living [105]. The fingertip force was measured using the setup shown in Fig. 4.11(a). The fingertip was measured using a load cell (LSP-2, Transducer Techniques), with the routing going through a pulley. The force was measured from two configurations; when the palm was all open or when the fingers were half open, as shown in Fig. 4.11(b)-(c). The maximal fingertip force reaches 8 N, which is sufficient to perform tooth brushing –

the highest fingertip force (6.37 N) needed for one study conducted in [106]. BRAG only weighs 186 grams including all electronics except the power supply.

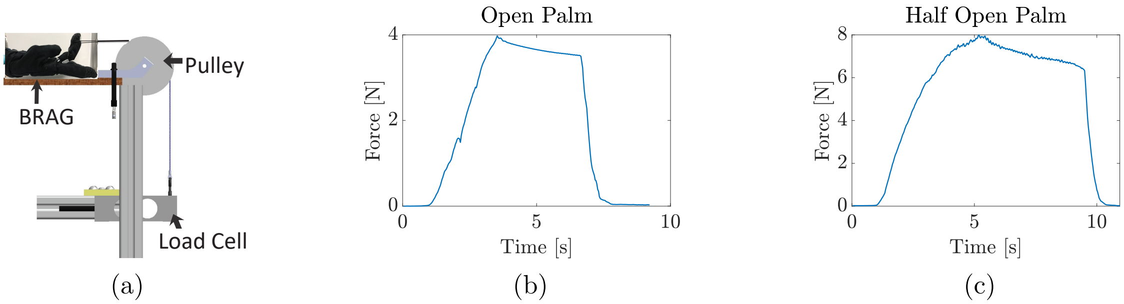

Figure 4.11: (a) Fingertip force setup, half open arrangement. The maximum fingertip force when measured from (b) Open palm position and (c) when the palm is half open

Grasping Performance

To test the performance of the proposed TSA-BRAG system, two sets of experiments were performed, namely, motion generation, and grasping with a 3D printed robotic hand. The objects for grasping were chosen to accomplish the six basic types of prehension grasping – cylindrical, tip, hook/snap, palmar, spherical and lateral grasps [107]. The experimental results are shown in Fig. 4.12(a)-(h). Items picked include a combination of common items like toothbrush and screwdriver. In addition, the items consisted of different outer surfaces and some were lightweight and others heavy. The characteristics of the items that were picked are summarized in Table 4.3.

Each pick and place experiment was conducted multiple times while keeping track of the resistance change as the grasp was performed. Keeping track of the resistance allowed for the verification of motion generations. The multiple trials allowed for the demonstration of the consistency of the resistance readings in the system. The transient of the resistance behavior during picking is shown in Fig. 4.12(i)-(k) for the

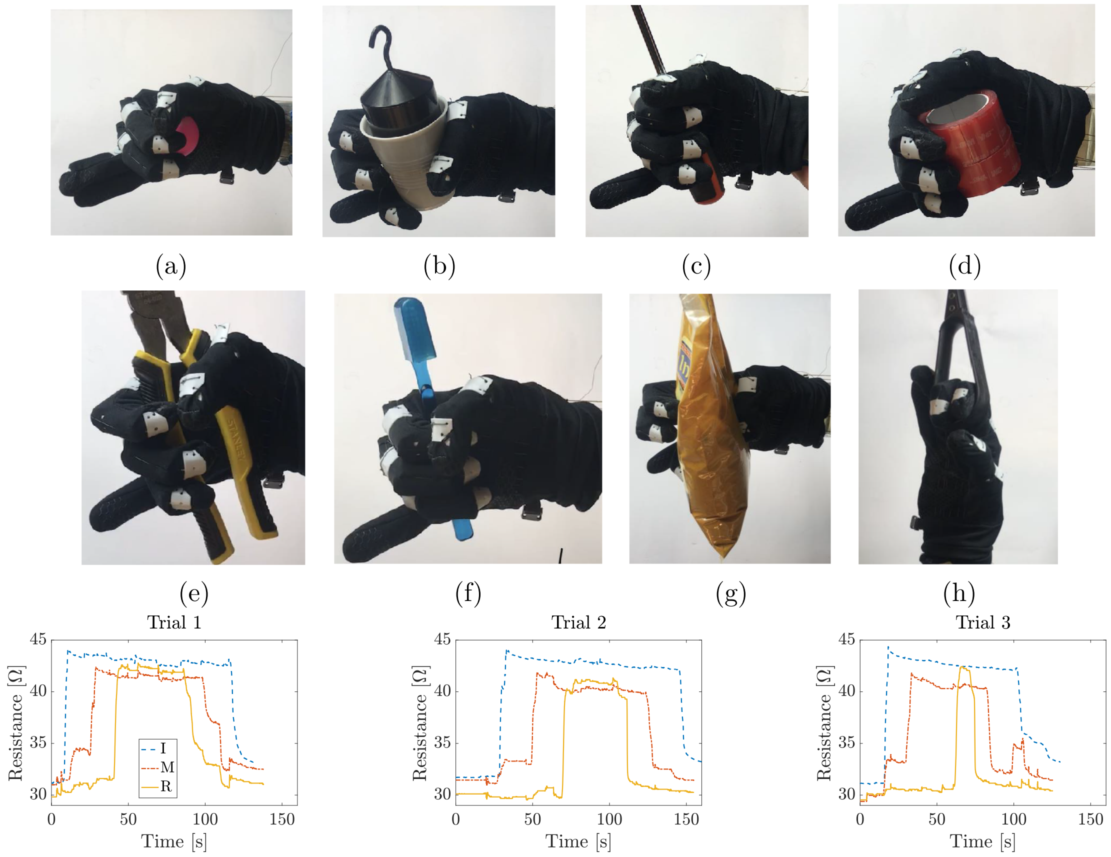

(i) (j) (k)

Figure 4.12: (a)-(h) show successful picks of everyday objects, demonstrating the capability to pick both heavy, light and different exterior surfaces. (i)-(j) show the transient resistance changes of the SCP string during the picking of a screw driver, with three attempts shown, where I is the index finger, M is the middle finger and R is the ring finger.

first 3 trials performed for the screwdriver test. In this setup, the fingers were actuated sequentially one after the other, as seen from the graph. Picking the screwdriver did not warrant the movement of the thumb. The mean and the standard deviation of the resistance for all the fingers during the picking (5 repetitions) is depicted in Table 4.4. The mean for all the trial is highly correlated and has a small spread. All the standard deviations are below 2.2 Ω, which demonstrates the consistency of resistance repetitions during the picking exercise.

Table 4.3: Picking performance of BRAG for different everyday objects

Object	Weight [g]	Surface and Type
Screwdriver	82.7	rubber, rigid
Plastic cup (1kg load)	1002.3	shinny, soft
Tumeric	408.9	shinny, soft
Pliers	427.7	rubber, rigid
VHB	63.5	shinny, rigid
Scrapper	53.7	clothe, soft
Toothbrush	8.4	shinny, rigid
Ping pong	2.2	shinny, rigid

From the data, it can be observed that the range predominantly varies from 7.7 Ω to 12.4 Ω. This variation was attributed to the difference in the starting length. Stretching the SCP strings appreciably meant that the minimum resistance was increased and as a result the range varied. In addition, the data also shows that the picking tasks can be differentiated by monitoring the resistance. For instance, the thinnest item picked was the toothbrush and as result, the resistance was higher – the finger had to close almost all the way. Conversely, the VHB had the biggest diameter – hence the expectation was that the resistance values should be lower. The mean resistance values for the fingers for toothbrush were 46.726, 47.582, 48.058 Ohms for the index, middle, and ring fingers, respectively. The resistance values for the VHB were 45.234, 42.410, 43.804 Ohms for index, middle and ring finger respectively. Evidently, the VHB shows lower resistance values compared to the toothbrush pick events.

The experimental results show that resistance measurements were stable and correlated to the diameter of the objects picked. For smaller objects the resistance was higher.

The time for full hand closure from open position varied between 4 seconds and 9 seconds. This corresponds to a frequency between 0.25 Hz and 0.11 Hz. It can be seen from Fig. 4.11(b) that it took 4 seconds (0.25 Hz) to achieve maximum force from

Table 4.4: Resistance behavior for all active fingers when BRAG performed picking tasks of everyday objects.

Finger	Range [Ω]	Mean (μ_R) [Ω]	Standard Deviation (σ_R) [Ω]
Screwdriver			
Index	12.322	43.650	1.460
Middle	11.686	42.450	1.042
Ring	12.224	42.044	0.591
VHB			
Index	10.5320	45.234	0.9738
Middle	8.9340	42.410	2.1426
Ring	11.8620	43.804	1.4437
Tumeric			
Index	7.792	45.842	1.8095
Middle	8.218	43.534	0.8429
Ring	8.1240	42.780	0.5548
Toothbrush			
Index	9.7840	46.726	0.3370
Middle	10.3460	47.582	0.7377
Ring	12.1560	48.058	0.3946
Scrapper			
Index	3.880	41.980	1.5631
Middle	7.888	44.350	1.2121
Pliers			
Index	9.2220	46.786	0.1210
Middle	9.4160	45.014	1.4753
Ring	9.628	44.756	1.4020
Plastic cup with 1kg			
Index	9.3920	45.052	0.5159
Middle	11.3900	45.262	1.7112
Ring	12.3120	44.904	2.0529
Ping pong			
Index	8.3600	46.07	0.3106
Middle	8.5760	44.39	1.5672

the open palm position. The bandwidth is between 0.11 Hz and 0.25 Hz. While the target full hand closure was 3 seconds, the variation is attributed to the dissipative sources like friction of the tendons in the fabric and the motor housings.

4.7 Discussion and Conclusion

This chapter presented the first comparative study on the TSA and motor-spool configurations. This study showed that TSAs could generate more than 5 times load output than motor-spool configuration. Furthermore, this chapter presented a new compact, high performance, soft glove that was powered with TSAs. The proposed TSA-BRAG system eliminated the rigid railing required for the non-rotating ends. Preliminary experiments were presented to validate TSA-BRAG's assistive capabilities for ADL, like grasping everyday objects. Preliminary findings confirmed that BRAG performed well with motion generation and grasping tasks with a passive robotic hand and an able-bodied human wearer.

Limitations of this study and future directions for improvements are discussed below:

- This study used ultra-high molecular weight polyethylene strings for the TSA configurations. These strings were rigid and in-extensible. This could potentially decrease the compliance of the device. Furthermore, TSAs were not back drivable, so any unwanted movement may result in over contraction and the user unable to resist the motion. In the next version of the TSA-BRAG, we plan to use compliant strings like coiled nylon polymer strings to improve device compliance [108, 50]. Our recent study found that SCP strings-based TSAs were compliant and enabled position self-sensing [109].
- Embedding fishing lines into the glove potentially limits the glove movement due to friction. The friction can be non-trivial, especially in regions with high stitch count and crossing over of rubber grips on the palm of the glove. There is a need to investigate methods to reduce friction. In addition, the effect of the

symmetry of the tendons around the fingers can be studied.

- Three different motors were considered in the performance comparisons of the TSA and motor-spool configurations. Similar experiments will be conducted for other new types of motors. In our future studies, we will also develop a dimensionless ratio that can help quantify the expected performance of TSAs and motor-spool configurations. Examples of normalization can be the power required normalized with gear ratio. Other important metrics, such as energy efficiency, will also be studied and compared.
- The fingertip force is an important metric to quantify the performance of assistive robotic gloves. In this study, only the performance of the finger motion and grasping were realized. A study on the fingertip forces will be conducted, which will enable the analysis of the fingertip forces useful for grasping and other tasks.
- The TSA-BRAG system employed a full-hand design, while existing studies mostly used open-palm designs. The thumb, index and middle finger should have individual motions, as these fingers work together to create the greatest surface area manipulation [102], and are referred to the dexterity/precision digits in other studies because of the role they play in understanding objects in space [103, 104]. A more in-depth analysis will be conducted to study the impact of the glove has on sensations through more human-studies.
- Lastly, the TSA-BRAG system was designed to be compact, high performance, and compliant. One more property that previous studies have shown to be critical is comfort. In this study, a human test was conducted to demonstrate that the TSA-BRAG could effectively work with and assist/augment human subjects in grasping tasks.

CHAPTER 5

AWARD: AN ACTIVE WEARABLE ASSISTIVE AND RESISTIVE DEVICE

5.1 Introduction

This chapter presents the design and characterization of AWARD that was driven by TSAs and operated in both assistive and resistive modes, the first of its kind. As shown in Fig. 5.1, four TSAs controlled flexion and two TSAs controlled the extension. The flexion TSAs were composed of stiff and SCP strings while the extension TSAs were made of only stiff strings. AWARD was embedded with four force-sensing resistors (FSRs).

5.2 Development of AWARD

5.2.1 Design considerations

AWARD was designed to be compliant, lightweight, compact, and exhibit two modalities — assistive and resistive modes. To ensure compliance, a thin soft-fabric glove was used. This glove allowed for the embedding of tendons for finger actuation. TSAs were used for actuation, ensuring that the device was lightweight and compact. In wearable devices, compactness is important — it ensures that devices fit on users' forearms and that the devices are lightweight, allowing for extended usage. The weight was minimized by reducing the number of the TSAs by coupling the motions of the fingers — the extensions of the little and the ring fingers were controlled by the

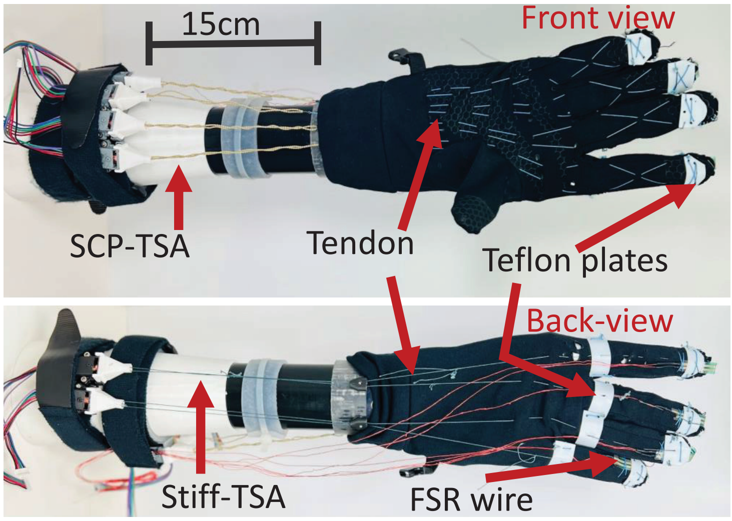

Figure 5.1: The design of an Active Wearable Assistive and Resistive Device (AWARD), (a) showing the front view of the device with the threading and Teflon plates that were used, and (b) showing the stiff twisted string actuators (TSAs) in the back view.

same motor. The extensions of the middle and the index fingers were also coupled together. The minimization of the TSAs did not significantly sacrifice the dexterity of the device.

In addition, to ensure efficient transition between assistive and resistive modes, the device was fitted with FSRs that provided real-time force measurements. Furthermore, conductive SCP strings were used in the TSAs for flexion of the fingers, allowing the resistance of the SCP strings to be tracked. The resistance allowed a further position tracking modality. This extra sensing information could correct the displacement when there was considerable backlash.

5.2.2 TSA configurations

Fixed twisting zone TSA

The advantages of the fixed twisting zone TSA are twofold; 1) it eliminates the necessity of a non-rotating translating rail, simplifying design and assembly to robotic devices, and 2) it enables the possibility of having two sections with strings of two different diameters. There has been limited work exploring the possibility of using two sections for the TSA that have two different diameters. Existing studies have explored the usage of a rigid rod in the twisting zone to increase the twisting diameter [110]. However, including a rigid rod decreases the compliance of the TSA and limit the application to wearable devices. For AWARD in particular, strings that were embedded in the soft fabric glove were of smaller diameter to reduce irritation of the user and reduce friction. Larger diameter, conductive strings were used in the twisting zone. In this work, the SCP strings were used for the non-embedded strings to facilitate the realization of length sensing and more compliance.

In the fixed twisting zone TSA configuration, the displacement is given by [110]

$$\Delta x = \sqrt{L_t^2 + \theta^2 r^2} - L_t, \tag{5.1}$$

where L_t is the fixed twisting zone, r is the radius of the string, and θ is the motor angle. In this model, the strings in the twisting zone and the sliding zone are of the same diameter. When the strings in the sliding zone and the twisting zone have different diameter strings, Eq. (5.1) is updated.

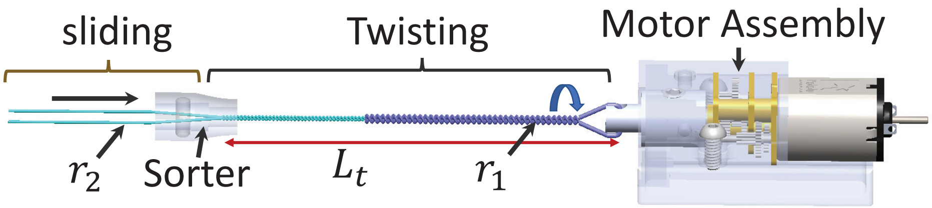

Figure 5.2: Schematic of a TSA with strings of two different radii with twisted strings in the twisting zone. In this setup, $r_2 < r_1$. Strings with radius r_2 are embedded to the soft glove and the smaller diameter minimizes friction and irritation that users would perceive.

Two-section, two-diameter TSA

The model when strings in the two sections have two different diameters is developed. In Fig. 5.2 the variable notations are shown, where r_1 is the radius of the strings initially in the twisting zone and r_2 is the radius of the untwisted strings in the sliding section. The displacement due to the contraction of the string of radius r_1 is [75]

$$\Delta x_1 = L_t - \sqrt{L_t^2 - \theta^2 r_1^2}, \tag{5.2}$$

when the initial length of strings with radius r_1 is equal to the length of the twisting zone, L_t. Since the length of strings with radius r_1 is fixed, the variable-twisting-zone TSA model is used to compute the displacement. Initially, there will be no strings of radius r_2 in the twisting zone. As Δx_1 increases, strings with radius r_2 will be fed into the twisting zone and twisted to result in further displacement. The displacement due to strings with radius r_2 is given by

$$\Delta x_2 = \sqrt{\Delta x_1^2 + \theta^2 r_2^2} - \Delta x_1. \tag{5.3}$$

In Eq. (5.3), we assume that both strings experience the same uniform motor rotations. If the strings are made from different materials and/or different diameters, the rotational stiffnesses will be different. For a rotational system without damping or inertia, the applied external torque can be expressed as $\tau = k\theta$, where k is the torsional stiffness and θ is the rotational angle. For a circular specimen of uniform cross section, the torsional stiffness is given by $k = GJ/L$, where G is the material rigidity modulus and $J = \pi D^4/32$ is the second moment of area. D is the diameter of the specimen. The rotational angle is then given as $\theta = 32\tau L/G\pi D^4$. For two separate strings of different stiffnesses, it can be shown that the total displacement, Δx, is given by

$$\Delta x = \theta_1 \sqrt{r_1^2 + \left(\frac{k_1}{k_2}\right)^2 r_2^2}, \tag{5.4}$$

where θ_1 is the motor angle, k_1, k_2 are string stiffnesses.

The experimental setup for the characterization of the two-section–two-diameter TSA is shown in Fig. 5.3(a). The setup used a position sensor (Honeywell SPS-L225-HALS) to measure the displacement of the load as the motor twisted the strings. The findings of the TSA are shown in Fig. 5.3(b) and (c). Fig. 5.3(b) shows the variation of displacement with rotations for the SCP-TSA. The SCP string was 14.5 cm and the twisting zone was 16 cm. The contraction range was therefore about 20%. The variations exhibit mild plateaus on the largest contraction.

The 5-ply, corresponding to 0.98 mm, was used. At 700 g constant load, the 5-ply produced the necessary range for full finger flexion. Previous works have shown that increasing the diameter of the SCP strings increases the force output [111]. Fig. 5.3(c) shows the changing resistance as the motor rotations increased for the SCP-TSA. The resistance of the SCP-TSA changed from about 17 Ω to about 12 Ω. The fluctuations in the resistance measurements were caused by the complex material and micro and macroscopic configurations of the SCP strings [76]. Twisting the SCP strings led to an increase in the area thereby resulting to a decrease in resistance [112].

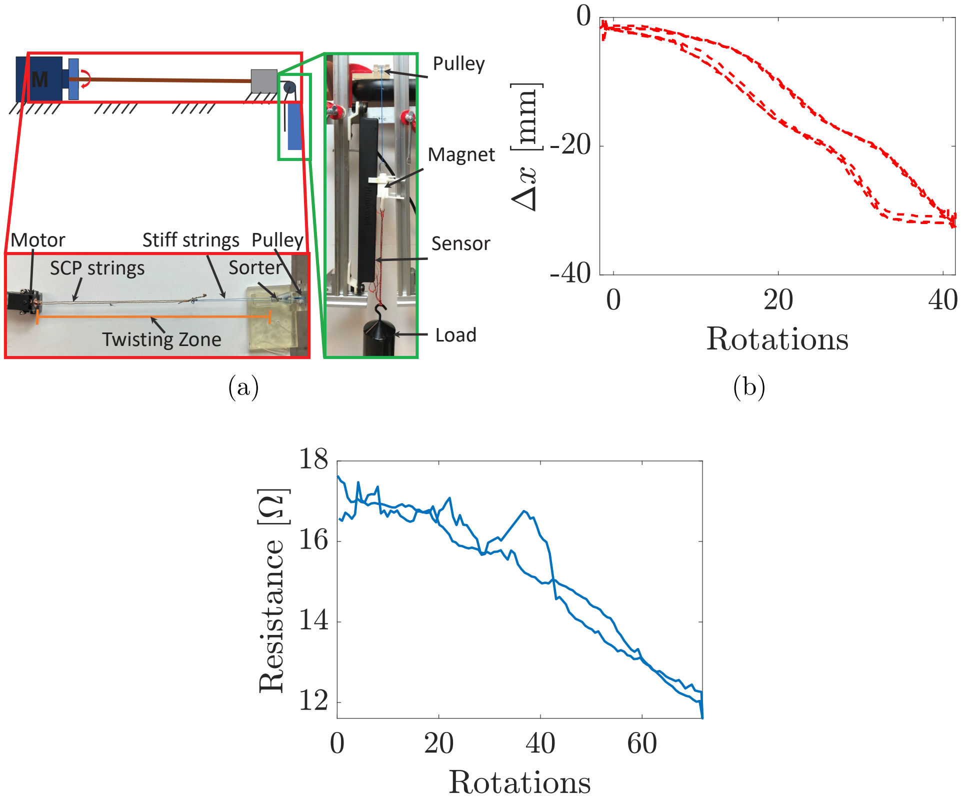

(a) (b) (c)

Figure 5.3: The characterization of the SCP-TSA; (a) Shows the experimental setup. The top left shows the overall schematic of the setup. The bottom left shows the top view and the right picture shows the front view of the setup components. (b) Shows the cycles of increasing rotations showing the variation of the displacement, and (c) shows the variation of resistance as the motor rotations changed.

5.2.3 Threading designs

The threading considerations were centered around limiting fabric deformation of the soft glove, withstanding high forces and consistently achieving desired finger joint actuation. Lightweight polyester, amoron biking gloves (Amazon: B08BZDT93Z) were chosen for their softness. Kastking SuperPower braided fishing line (Amazon: B00C6OUDX2) was embedded in the glove to actuate the fingers. This string was 0.30 mm in diameter and had a maximum load of 18.2 kg with minuscule stretch when forces were applied. The strings were smooth and minimized friction with the fabric glove [113].

The relative position of the embedded fishing line to the finger determined the amount of torque that the finger experienced. Previous works used fishing lines on the side of the fingers [114]. Although this approach left a majority of the finger free for interaction with the environment, the mechanical advantage reduced and could require high-torque motors. To reduce fabric deformation and improve force distribution, thin Teflon plates (0.8 mm) were added in the finger posterior. These plates were placed on two locations: 1) the joint between the medial and proximal phalanges of fingers and 2) on the fingertips of the anterior of the hand. However, such approaches resulted in the glove being uncomfortable to wear and required prior knowledge about the knuckle dimensions for improved fit. The Teflon on the posterior of the fingertip eliminated the need for plastic rings [115].

In addition, as shown in Fig. 5.1 front-view, a criss-cross design was utilized to enhance finger facing-tension forces [115], which limited fabric deformation and allowed joints to move independently. The combination of the Teflon plates and the criss-crossing design ensured that AWARD could withstand high forces with limited fabric deformation. The assistive and resistive modes of AWARD were predicated on the ability of the glove to withstand high forces.

5.2.4 Sensor selection

Force sensor selection

A sensor with a compact form factor, low hysteresis, and high force output range was needed — simplifying assembly and allowing accurate and repeatable dynamic force measurements.

The FSR (FSR UX 402 [34-00125], Interlink Electronics) was chosen. It had a force output range of 0.5 N to 150 N, with continuous force resolution and low hysteresis. The calibration of the FSR was conducted by recording the voltage output when increasing load was applied. The voltage and force showed a nonlinear response. An 8$^{\text{th}}$ order polynomial model was fitted to the experimental data and showed an average error of 0.1917 N. The order was chosen considering the accuracy and the model complexity. The model is

$$\begin{split} F(V) = p_1V^8 + p_2V^7 + p_3V^6 + p_4V^5 + p_5V^4 \\ +p_6V^3 + p_7V^2 + p_8V + p_9, \end{split} \tag{5.5}$$

where F_1 is the force output, p_1=0.1395, p_2=$-$1.878, p_3=10.52, p_4=$-$31.58, p_5=54.86, p_6=$-$55.14, p_7=29.8, p_8=$-$5.521 p_9=1.216.

Higher-order polynomials have been implemented in force sensing [116]. Calibration was only performed on one FSR, however the manufacturer claimed part-to-part deviation of within 5% [117] eliminated the need to perform calibration on all sensors.

Supercoiled Polymer displacement sensor

The SCP strings were selected for their dual nature — working as the TSA strings and as a displacement sensor. SCP strings are conductive silver-coated multi-thread nylon filaments that exhibit variable resistance due to length change. Further, SCP strings increase compliance, thereby increasing safety in wearable devices. The SCP strings were selected for their ease of diameter customization, and the ability to obtain stable resistance values. The sensing properties of the SCP string-based TSA have been recently studied in our group including modeling, transient behavior [118] and applications in robotic devices. The stretch properties and the resistance variation were characterized for application in soft wearable devices [119].

The SCP displacement sensor provided an added sensing modality in addition to the motor rotations. While using encoders in motor-based actuation has been widely used, backlash from the gearboxes poses a challenge in ensuring repeatability. Since the resistance changes are only affected by the change in length, this measurement could be used to further inform the position of the fingers.

5.2.5 Electrical design

AWARD was driven by the Teensy®4.1 micro-controller due to the high number of I/O pins and high clock speed. The micro-controller read six quadrature encoders, controlled six motors requiring twelve pulse-width modulation (PWM) pins. Four of the motors (30:1 [ServoCity: 638103]) drove the TSAs for flexion and two of the motors (50:1 [Servocity: 638102]) drove TSAs for extension. Higher gear ratio motors were used for extension to maximize resistive forces. The micro-controller also read four analog-digital converters (ADCs) from the four FSRs and read a further four resistances from the four SCP-TSAs for the flexion of the fingers. ADC values were obtained using an ADS1115 16-bit ADC.

5.2.6 AWARD

AWARD weighs only 198.1 g, including all the actuation units but without the power supply. It can achieve different movements when the TSAs were actuated. AWARD provided assistance in addition to offering resistance to user motion. The thumb was not actuated for this version of AWARD. It is important to note wire harnesses were temporarily removed for characterizations of AWARD.

5.3 Experimental Characterization

The experimental characterization of AWARD constituted a set of three experiments: 1) motion test that verified the attainable device movements, 2) performed static force tests, and 3) conducted dynamic force tests.

The motions that were attained by AWARD were tested using the monotonically increasing and decreasing input motor rotations shown in Fig. 5.4(a). Fig. 5.4(b) and (c) demonstrates the motion of AWARD with the input motor rotations in Fig. 5.4(a). The variations of the length and the resistance with motor rotations are shown in Fig. 5.4(d). It was shown that there was a correlation between the changing resistance with the changing length. While this variation was not strictly monotonically increasing or decreasing, transient models to capture this behavior were recently developed[118].

A set of three static finger positions were selected for static force testing. The three positions were: when the fingers were almost fully opened (P_1), when the fingers were half-way open (P_2), and almost fully closed (P_3), as shown in Fig. 5.4(e)–(g). These positions were consistent for both extension and flexion force testing. To ensure

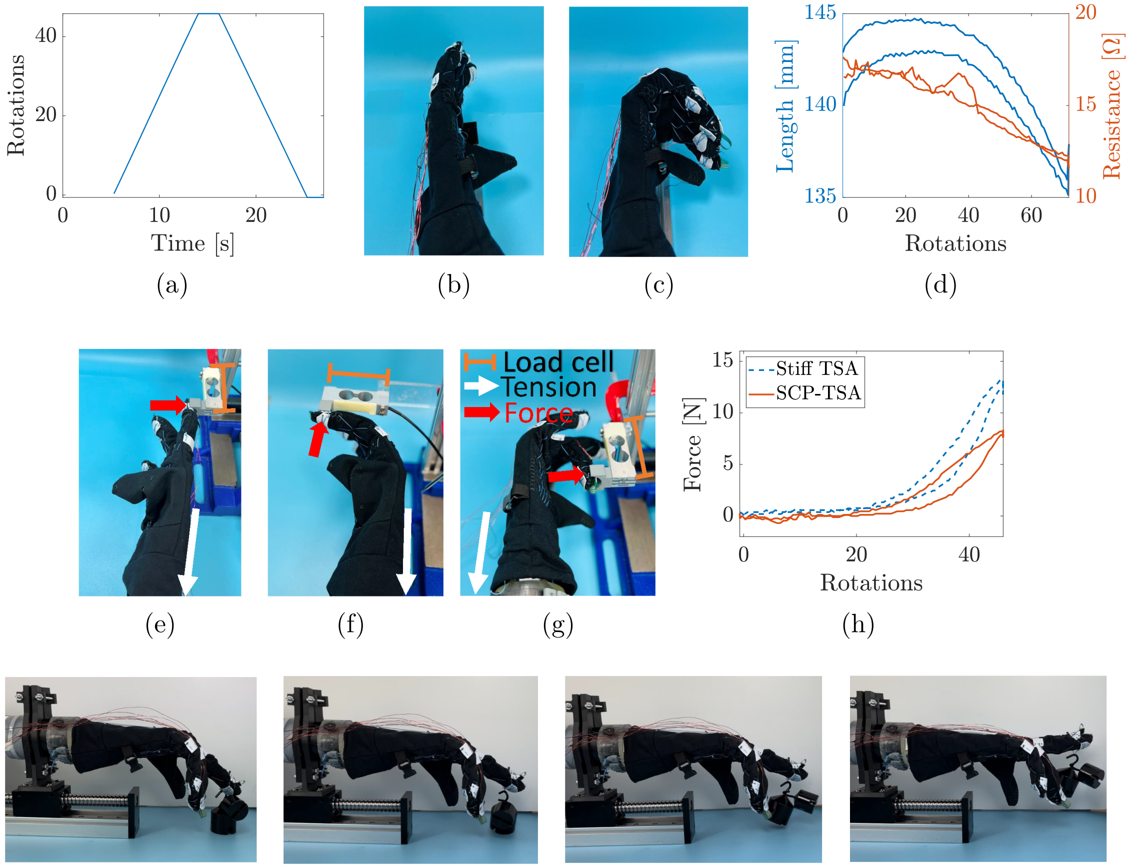

(a) (b) (c) (d)

(e) (f) (g) (h)

(i) (j) (k) (l)

Figure 5.4: (a) The motor input rotations for the actuation of AWARD. (b) and (c) are the motions of AWARD in two different time instants when in flexion. The setup for extension force experiments with (e) showing position P_1, (f) showing position P_2, (g) showing position P_3 in extension force testing and (h) showing the variation of force with motor rotations for both the stiff string TSA and SCP-TSA, (i)–(l) shows AWARD lifting a 300 g load at different time instants in extension.

consistency, these positions were achieved by actuating the TSAs to establish the number of rotations needed to reach each position. For example, the flexion of the little finger required 6, 20, 45 rotations for P_1, P_2, P_3, respectively. In extension, the little-ring fingers required 55, 37, 4 motor rotations for P_1, P_2, P_3, respectively. When AWARD was fully open, the flexion TSAs were at zero motor rotations while the extension TSAs were at maximum motor rotations. The reverse was true when AWARD was fully closed.

Testing was performed using a mannequin, to decouple involuntary finger movements. In Fig. 5.4(e), position P_1 is shown with the load cell (LSP-5, Transducer Techniques) rigidly attached to a static frame and the finger resting on a 3D printed attachment connected to the load cell. The attachment ensures that the fingers do not slide up or down on the load cell during the experiments. Fig. 5.4(f) and (g) show positions P_2 and P_3 for extension. The TSA was actuated, allowing the fingertip to push against the load cell as indicated by the arrows. For each finger, the height of the load cell was adjusted to align the load cell and the finger. The attachment stage consisted of a lead screw mechanism to easily adjust the position of the hand mannequin. For all positions, the fingertip forces were recorded as the TSAs were activated. For each location, three trials were conducted, with each trial consisting of two cycles of increasing and decreasing motor rotations. The variation of the force with motor rotations is shown in Fig. 5.4(h). It is shown that the SCP-TSA exhibited slightly less maximum force output. The compliance of the SCP strings resulted to this force differences.

The dynamic resistive loading experiment was conducted by actuating the TSAs on the posterior of AWARD while the finger was attached to a load of 300 g. The actuation of AWARD at different time instants during the resistive loading is shown in Fig. 5.4(i)–(l). Fig. 5.4(i) shows the time instant before the finger started lifting the load and Fig. 5.4(l) shows the time instant when the load completely rested on the finger.

The summary of the average peak forces in the different locations for flexion and extension are shown in Table 5.1, where σ is the standard deviation. A maximum force output of 15.63 N was achieved in flexion in P_1 for the middle finger. While this force had a small standard deviation of 0.17 N, it was markedly higher than other

Table 5.1: Force [N] performance of AWARD on both flexion and extension

	P_1	σ_1	P_2	σ_2	P_3	σ_3
Flexion						
Little	5.28	0.08	6.45	0.12	7.69	0.59
Ring	6.04	0.07	3.38	0.21	8.04	0.39
Middle	4.18	0.29	4.40	0.68	15.63	0.17
Index	7.42	0.68	6.42	0.06	8.66	0.42
Extension						
Little, Ring	8.54	0.30	8.52	1.15	9.78	1.67
Middle, Index	10.40	0.10	13.55	0.96	12.82	2.67

forces in this position. This was likely due to the lengths of the phalanges for the middle finger being long and providing a higher mechanical advantage. The highest maximum force in extension of 12.82 N was observed for the middle-index fingers in position P_1. However, there was a high standard deviation for this position showing the high variation in the forces in the different trials performed. In addition, the force outputs were consistent in flexion tests. The middle and index fingers consistently displayed higher force values than the ring and little fingers in flexion and extension.

Table 5.1 shows that the forces were higher in position P_2 during extension compared to flexion. The force output at each fingertip varied depending on the finger joint angles and whether the tendon was on the anterior or posterior of the hand. On the anterior side, the decomposition of the forces resulted in force components pointing toward the inside of the hand, reducing the effect of friction on the tendons. In contrast, on the posterior, the cables were pressed into the mannequin, increasing the friction and reducing the effective force on the fingertips.

5.4 Conclusion

In this work, we have presented the design and characterization of AWARD, detailing the design decisions and analysis of the sub-components of the device. Key features of AWARD are the ability to operate both in assistive mode and resistive mode while being compact, soft and lightweight. Using TSAs that have strings of different materials improved the properties of TSAs, including compliance and the ability to act as a sensing modality.

CHAPTER 6

AWARD V2

6.1 Introduction

This chapter presents the system design improvements of AWARD that were conducted in addition to the work presented in Chapter 5. The implementation of hardware design improvements including the design and fabrication of a printed circuit board (PCB) and incorporating more sensing modalities that allows for the usage of AWARD without needing motion capture systems is presented.

6.2 AWARD Hardware Overview

In addition to the sensing highlighted in Chapter 5, the following sensors were added in second version. Inertial Measurement Units (IMUs, LSM6DSM [STMicroelectronics: LSM6DSMTR]) were utilized to enable the measurement of finger joint angles. Measuring joint angles allow AWARD to be used without the need for motion capture systems during calibration or during normal usage as predominantly used in existing literature [35, 36]. The LSM6DSM IMUs were selected for their compact form factor (2.5 mm × 3 mm), high accuracy and stability [120].

In addition, current measurement sensors (ACS70331 [Digikey: 620-1923-ND]) were installed to help in understanding the torques that were applied by motors during the actuation of TSAs. The ACS70331 was selected for its high sensitivity and high bandwidth [121].

6.3 Sensor Selection

6.3.1 SCP displacement sensor and FSR

The reader is referred to Chapter 5.2.4 where the choice of SCPs and FSR is motivated. The FSRs allowed for the force control of the fingers, especially during the resistive mode of AWARD.

6.3.2 Inertial Measurement Units (IMU)

The IMUs were chosen to allow for the use of AWARD without needing lab-based motion capture systems [35, 36] like Vicon, OptiTrack, Qualys, electromagnetic sensors [37], or vision-based approaches to estimate the bending angles of the fingers. In addition, the small footprint of IMUs allowed for the fabrication of a similarly small footprint PCB that allowed the IMUs to fit on the finger width without making the device bulky.

While IMUs have been predominantly used in lower body exoskeletons like hip assistance for gait detection [122], the usage in actuated wearable gloves has been limited. For instance, these sensor gloves were only used to estimate finger joint angles of healthy users without active actuation to the devices [123, 124]. The usage of IMUs might be considered to have a high degree of uncertainties due to drift and errors, but previous studies that used IMUs demonstrated good performance. In addition, there has been studies that quantified the performance of IMUs as an estimation for the angle between two moving IMUs that demonstrated low degree of errors [125].

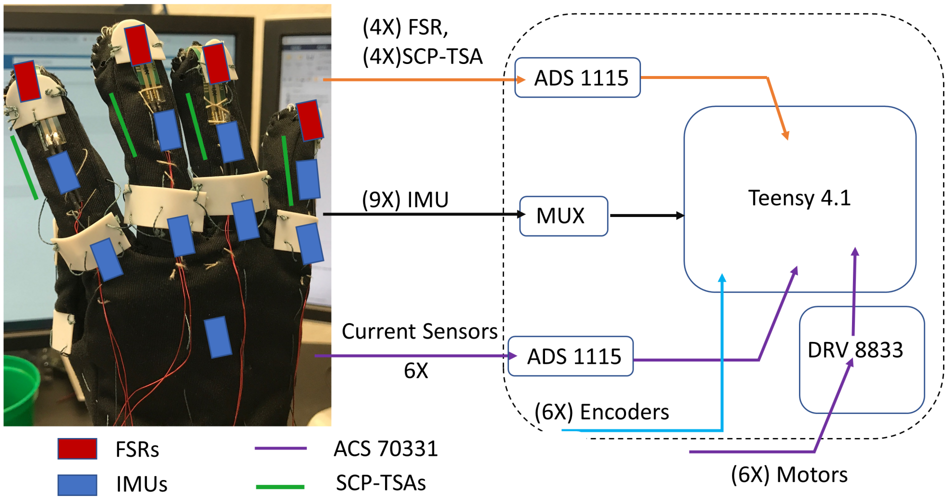

Figure 6.1: The full architecture of AWARD, showing the relationship between all the components.

6.3.3 Electrical design and system integration

The full architecture of the electrical design of AWARD is shown in Fig. 6.3. As shown in the architectural setup, the number of signals and measurements that were necessary for AWARD were high. AWARD was driven by the Teensy®4.1 micro-controller due to the high number of I/O pins, high clock speed and compact form factor. Despite the high number of I/O pins, the pins were not sufficient to read all the necessary sensors and control the motors. As a result, a sixteen channel Multiplexer/Demultiplexer (MUX, [DigiKey: CD74HC4067SM96]) was used to expand the needed I/O pins.

The micro-controller read six quadrature encoders, controlled six motors requiring twelve pulse-width modulation (PWM) pins. The micro-controller also read four analog-digital converters (ADCs) from the four FSRs and four resistances of the four SCP-TSAs for the flexion of the fingers. Additionally, the micro-controller read six current measurements from the six motors. ADC values were obtained using an ADS1115 16-bit ADC (Amazon: B00QIW4MGW). Finally, the micro-controller also

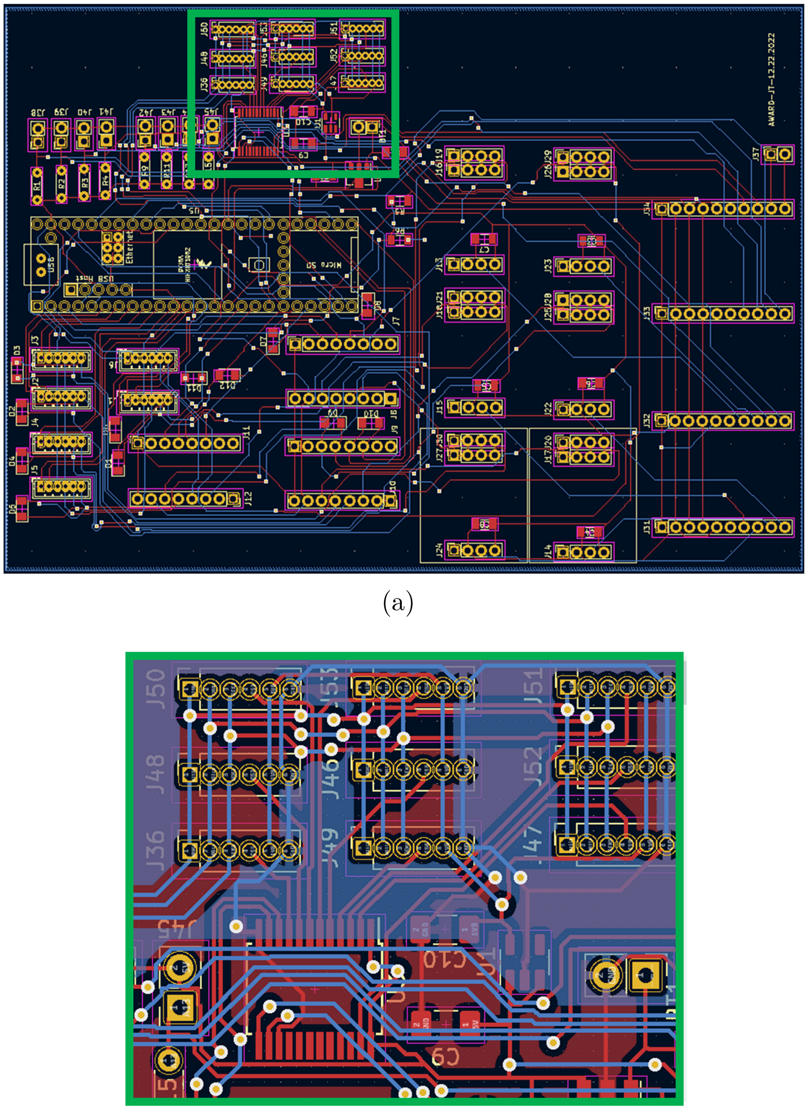

(a)

(b)

Figure 6.2: The Inertial Measurement Unit (IMU) printed circuit board (PCB) based on the LSM6DSM package. (a) Shows the physical assembled PCB, and (b) Shows the KiCad schematic of the PCB. The dimensions of the physical PCB were 13.95 mm × 8.53 mm.

read nine IMUs.

The schematic of PCB of AWARD is shown in Fig. 6.2, with Fig. 6.2(a) showing the full model PCB. The PCB had 19 unique electrical components and 89 total components. Fig. 6.2(b) shows a zoomed-in section of the PCB that contained the

Multiplexer/Demultiplexer and the IMU connections. The master physical AWARD PCB is shown in Fig. 6.3, where the key components are highlighted. It is important to note that the footprint of the PCB as shown in Fig. 6.3 can be reduced significantly when breakout boards are not used. The breakout board enabled straightforward debugging and swapping of components when needed during the development. When the actual integrated components are used the board can be shrunk by approximately 80%.

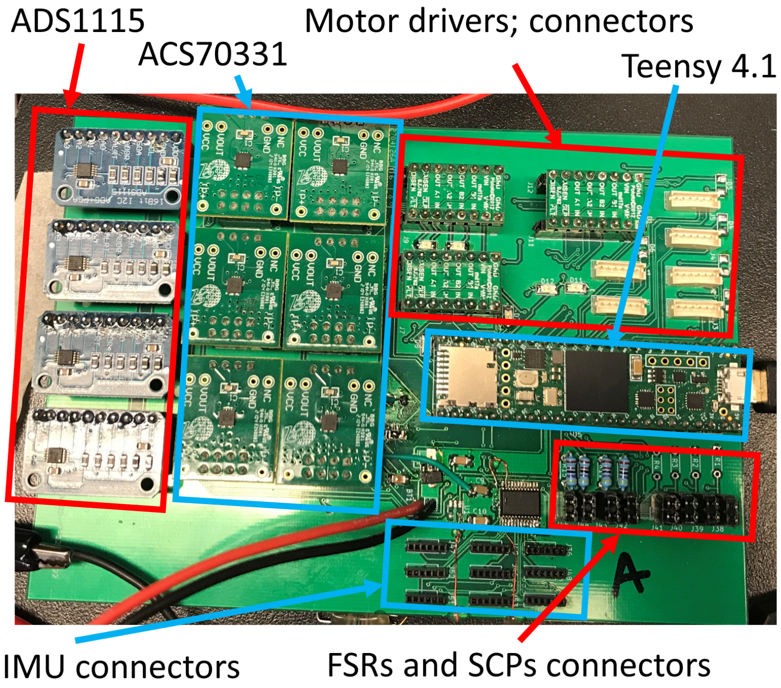

Figure 6.3: The PCB of AWARD electronics. The PCB measured 105 mm × 148 mm.

Due to lack of compact IMU PCBs that could fit into the width of the fingers without interfering with the movement of the fingers, a custom IMU PCB was fabricated. The PCB for the IMUs was fabricated to ensure the footprint fits the fingers is shown in Fig. 6.4. In Fig. 6.4(a), the physical PCB board is shown and in Fig. 6.4(b), the KiCad model of the PCB is shown. The compact form factor of LSM6DSM IMU package made assembly challenging. The IMU PCBs were then attached to AWARD using designed assembly holes, which allowed the PCBs to be sewn directly to the fabric as shown in Fig. 6.5.

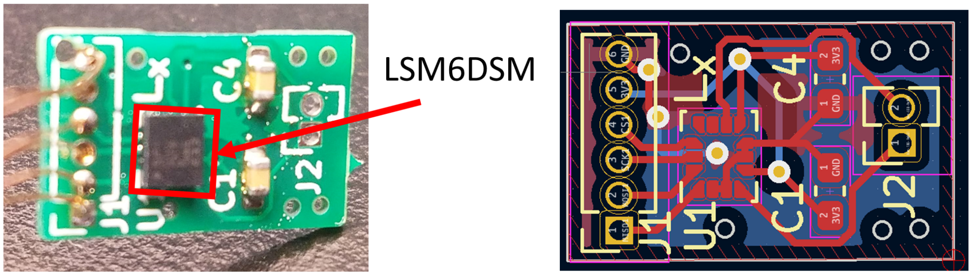

(a) (b)

Figure 6.4: The IMU PCB based on the LSM6DSM package. (a) Shows the physical assembled PCB, and (b) Shows the KiCad schematic of the PCB. The dimensions of the physical PCB were 13.95 mm × 8.53 mm.

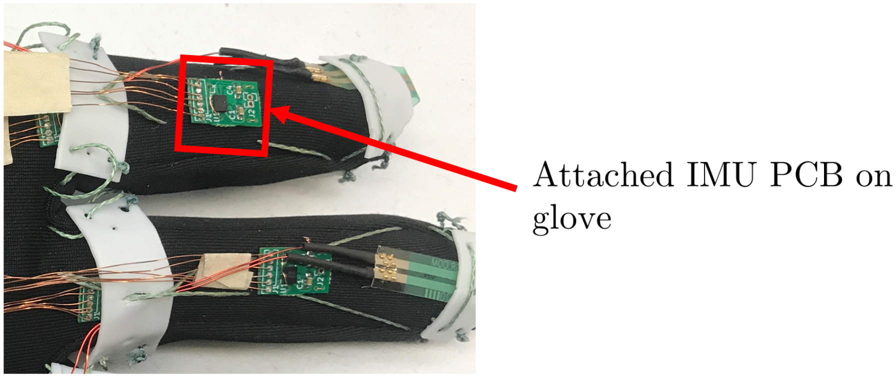

Figure 6.5: The IMU PCB attached to AWARD. The PCB was sewed to the glove fabric by using 36 AWG copper wire to ensure it was securely attached.

6.4 Sensor Readings

6.4.1 FSRs and SCPs

The readings for the FSRs and the SCPs were transferred using the I2C communication protocol. The values of the FSRs and SCPs were acquired through the usage of the voltage divider configuration then converted to ADC in ADS1115 16-bit chip.

For the FSR, applying pressure changed the resistance. For the SCP, when the length was changed, the resistance changed as well. In both cases, it was critical to select the reference resistance, R_f so that the output voltage of the divider both had a high range and high sensitivity. Therefore, it was essential that the choice of the reference resistance was taken with great care. Specifically,

$$R_f^{\mathrm{scp}} = \sqrt{R_{\mathrm{max}}^{\mathrm{scp}} R_{\mathrm{min}}^{\mathrm{scp}}} \tag{6.1}$$

where $R_{\mathrm{max}}^{\mathrm{scp}}$ is the maximum possible resistance when the SCP was fully stretched and $R_{\mathrm{min}}^{\mathrm{scp}}$ is the minimum resistance of the SCP when it was at rest length. The same relation applies for the FSR. Eq. (6.1) was obtained by maximizing the difference of the voltage out of the voltage divider at low resistance and at high resistance of the sensor.

6.4.2 IMU

The nine IMUs were read by using the SPI protocol in the Teensy®4.1. Each IMU was selected quickly using the chip select pin that allowed the specific IMU to be read. This was repeated every time an IMU was read. For the same finger, the frequency of turning on and off the IMUs was conducted at 100 Hz. It is important that the chip select pin is only low during the reading of a selected IMU. Therefore to ensure that the correct IMU was read and that there was no data corruption due to trying to read multiple IMUs on the same bus, it was key that pull-up resistors be installed. The pull-up resistors were pulled to 5V with resistors of 10 kilo-ohms.

6.4.3 Printing data

The control of AWARD required that the computations be performed in real time. However, it was still essential to record the data for post processing and performance analysis. Therefore the sensor information was streamed to the serial monitor using USB. When this approach was used, due to the large amount of sensor information that was being streamed, the control loop was affected. As a result, the on-board SD card on the Teensy®4.1 was used to record the device sensor data.

6.5 IMU Calibration

Calibration of the IMUs were performed before data collection to determine the bias values for accelerations and gyro rates. Calibration was conducted by placing the finger in a fully extended position on a horizontally flat surface. The average of 500 values for each IMU were recorded as the bias values. These values were hard-coded and also stored in EEPROM of the micro-controller to be subtracted from measured values for all measurements. Calibration was then disabled in the software.

The state of each finger was achieved by using the sensing information installed in the glove which included IMUs, SCPs, current draw from the motors, encoder positions and the force measurements from FSRs. In this section, an outline of the process to obtain the measured values is explained.

First, the method to obtain the finger joint angles is explained. The angles were obtained through the utilization of the IMUs that were installed at the back of the finger. Four IMUs were used as shown in Fig. 6.6. These IMUs were then used to

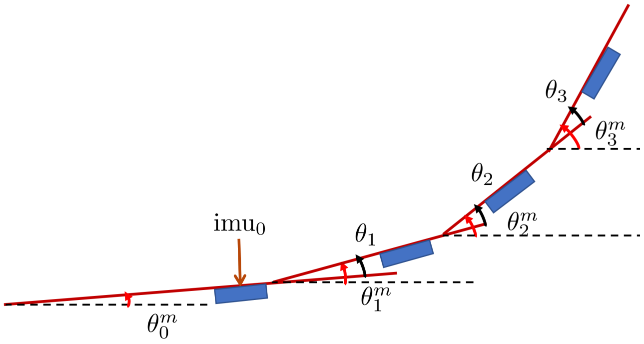

Figure 6.6: A schematic representation of the IMU locations. θ_i^m is the measured angle and θ_j is the joint angle. The IMUs measure the angle relative to the horizontal.

compute the finger joint angles. In particular,

$$\theta_j = \theta_{i+1}^m - \theta_i^m, \tag{6.2}$$

where $j \in (1,2,3)$ and $i \in (0,1,2)$. To enable real time measurement of the angles using the IMUs, it was important to implemented a method that showed fast response. In this effort, the Madgwick library which computes Euler angles from accelerations and gyro rates of the IMU was implemented [126]. However, the response of the angle computation was slower, as shown in Fig. 6.7. Instead, the basic complimentary filter was implemented, which resulted in a faster response as shown in Fig. 6.8. The raw accelerations have been plotted showing when the change was initiated and how the computed angle compared from that change. In Fig. 6.7 the raw accelerations have not been shown, however different frequencies have been shown. The expectation was that increasing the update frequency of the filter should increase the response, but it demonstrated the opposite effect. Tweaking the library didn't yield positive results.

As a consequence of the performance difference, the basic complimentary filter was implemented for all the experiments to compute the Euler angles. An example of the sensor information that were collected are shown in Fig. 6.9.

Second, the external torque was computed directly from the measured motor

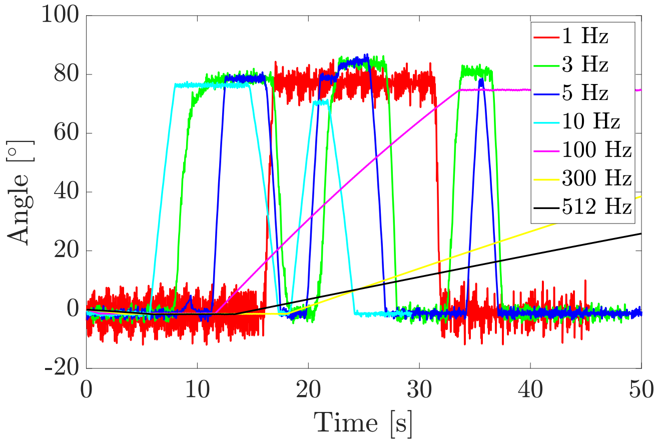

Figure 6.7: Sensitivity response of Euler angle computation using Madgwick filter with different update frequencies. Increasing the update frequency decreases the sensitivity.

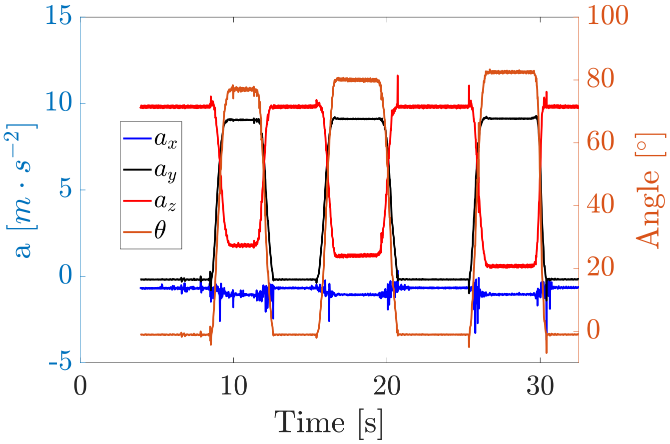

Figure 6.8: Computing Euler Angles using a basic complimentary filter demonstrated fast responsiveness.

current. In addition, the force from the FSR was computed directly from FSR measurements. An example of the angles measured using IMUs is shown in Fig. 6.9(a). In Fig. 6.9(b) the angles are shown with respect to time, demonstrating the duration of the test and the fast response of angle measurements.

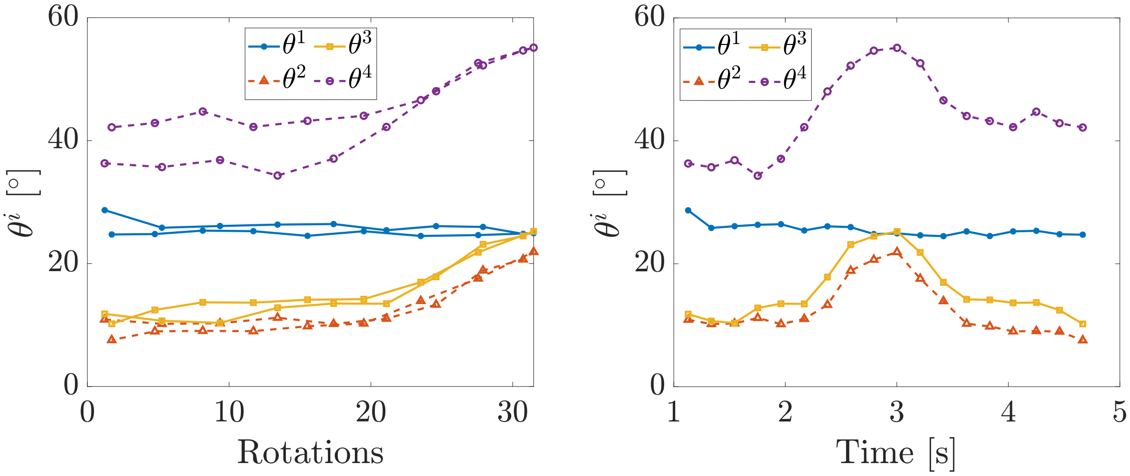

(a) (b)

Figure 6.9: IMU readings. (a) Shows the reading from the four IMUs on the phalanges plotted against number of rotations. (b) Angles of the phalanges plotted with respect to time.

CHAPTER 7

WEARABLE ROBOTIC WRIST ORTHOSIS

7.1 Introduction

This chapter presents the design of a compact and compliant wearable wrist orthosis that uses both stiff fishing lines and compliant SCP strings, as shown in Fig. 7.1. The orthosis has three DOF, providing pronation or supination (PS), flexion or extension (FE), and adduction or abduction (AA). The SCP strings are used to track the movement of the wrist by monitoring the resistance changes during actuation. The chapter further shows that the range of motion provided by the device is comparable to the necessary range of motion to efficiently perform ADLs. Lastly, the chapter demonstrates the ability to induce actuation in a human subject, with no muscle activation from the healthy user.

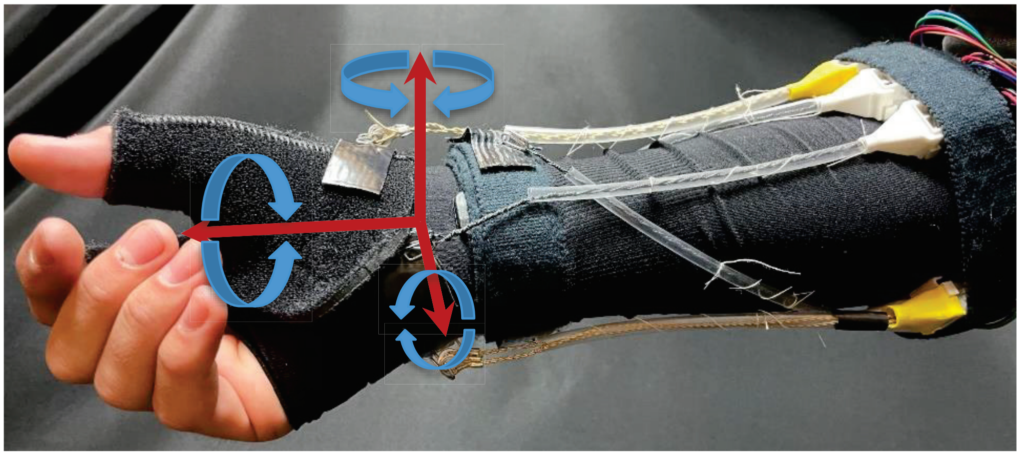

Figure 7.1: The proposed wrist device that allows for the actuation of three DOF of the wrist being worn by a human subject. Flexion/extension and pronation/supination are moved with TSAs with stiff fishing lines and adduction/adbuction is moved with TSAs with compliant SCP strings.

7.2 TSA Design

7.2.1 TSA configuration

The fixed string length TSA configuration were adopted to minimize string friction effects from the fixed sorter. The distal end of the TSAs were rigidly attached to the device to eliminate the need for a fixed non-rotating rail. In this approach, the strings were not embedded into the sleeve which allowed for the twisting of strings. Instead, strings were routed using tubes that were attached to the sleeve. The distance of the TSAs motors from the wrist to the forearm was adjusted to ensure that the correct range of motion was achieved through the contraction of the TSAs.

7.2.2 Design guidelines

The wrist orthosis was designed to be compact, compliant, and capable to produce the range of motion necessary to perform ADLs. The tension requirements for the strings used were 17.5 N, 11.6 N, and 3 N for FE, AA, and PS, respectively. These tensions were calculated using the torque requirements for ADLs [22, 25] and the wrist measurements of a 25 year old male, with the diameter of the wrist of 6 cm and thickness of 4 cm [22]. Additional design guidelines are discussed as follows:

First, the strings to be used must be able to produce force outputs that are, at minimum, larger than the aforementioned requirements.

Second, to minimize non-compliant materials on the device, the fishing lines and SCP strings were chosen to be used. However, to maintain high force output, the diameter of the SCP strings was carefully picked by performing an increasing constant

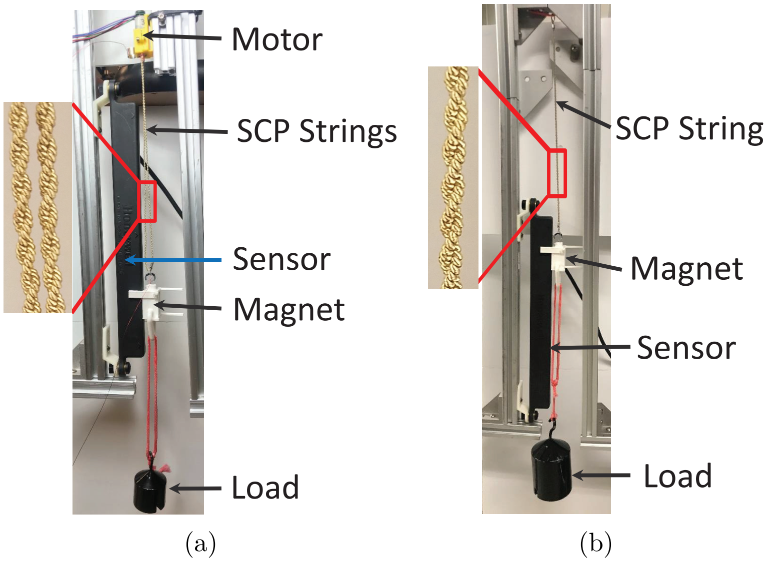

(a) (b)

Figure 7.2: The SCP string compliance testing setup: (a) Testing setup for two SCP strings under the TSA configuration (b) Experiment setup for single SCP strings testing. Both tests are performed under constant loading conditions.

loading experiment to determine the maximum force that can be supported. For SCP strings, the diameter was varied by changing the ply number. SCP string diameters of 1.12 mm, 1.62 mm, 2.00 mm, and 2.25 mm which corresponds to 5-ply, 10-ply, 15-ply, and 20-ply, respectively, were tested. In addition, it was necessary to ensure that the compliance exhibited by the SCP strings was not excessive. A high degree of compliance will require a higher contraction ratio to allow for SCP strings to fit on the forearm.

Third, it was imperative that the range of motion (RoM) produced by the device be comparable to the RoM necessary to perform ADL. The size of the twisting zone was adjusted to ensure that the contraction of the TSAs produced the required RoM. Using the setup shown in Fig. 7.2(a), the resistance of the SCP strings was measured as the TSAs contracted.

7.2.3 SCP string sizing and characterization

For each string diameter, a constant load was applied with the change in length recorded. The SCP strings were loaded until they were close to failure and break. The failure load was determined by loading three consecutive SCP strings to failure, with the testing load around 150 g less than the failure load. The load was increased from 50 g to 3.7 kg. The experimental setup is shown in Fig. 7.2(b). One end of the SCP string was attached to a fixed end, with the proximal end attached to the magnet holder of the position sensor (Honeywell SPS-L225-HALS). The bottom of the magnet holder was used to attach the loads. The sensing range was 225 mm and had a resolution of 0.14 mm. The sensor used magnetoresistive arrays to accurately determine the position of a magnet that was affixed to a translating object. The experiment was also performed with two SCP strings in the TSA configuration setup, as shown in Fig. 7.2(a). The findings of the compliance testing for the SCP strings are shown in Fig. 7.3. As shown in Fig. 7.3(a) and (b), increasing the ply increased the load the strings can support. Fig. 7.3(b) also shows that the maximum stretch increased as the load and ply were increased. The average percentage stretches were 15.48%, 22.33%, 40.20%, 44.40% for the 5-ply, 10-ply, 15-ply, and 20-ply, respectively. These performances were for different maximum loading conditions. However, it was important that the stretch was not too large, as in the 15-ply and 20-ply ones, since it reduced the overall contraction of the SCP strings. While larger diameter SCP strings produce high force outputs, the torque requirements become large. Furthermore, the 5-ply SCP strings did not produce sufficient force output. As a result, the 10-ply was selected in this study.

In addition, the degree of repeatability of the SCP strings – that is to return to the original position after stretching, is essential. If the SCP strings do not return to the

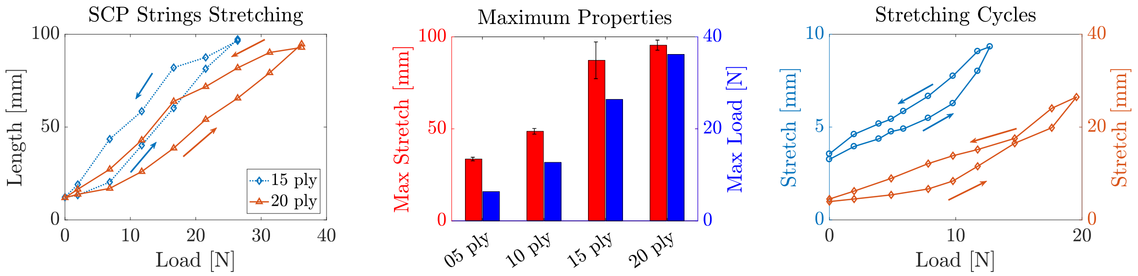

(a) (b) (c)

Figure 7.3: The stretch characterization of the SCP strings: (a) shows the stretching of SCP strings as the load was being increased then decreased, (b) shows the maximum load and maximum stretch supported just before failure occurred, and (c) shows the stretch characterisation of two 10-ply SCP strings of different resting lengths: stretching when an SCP string was gradually loaded to 1300 g and then unloaded, and when an SCP string was gradually loaded to 2000 g and then unloaded.

original length, this will necessitate a higher contraction ratio. Fig. 7.3(c) shows the results from the loading and unloading of two 10-ply SCP strings, up to 1300 g and up to 2000 g. When loaded up to a maximum load of 1300 g, the maximum stretch was 4.34% of the original length, with a permanent stretch of 0.295 mm. When loaded to the maximum load of 2 kg, the maximum stretch was 12.31% of the original length and a permanent stretch of 0.548 mm. The permanent stretch was minimal, and the high degree of returning to the original starting length after stretching was further shown by the complete loading loops.

7.3 Orthosis Design

7.3.1 Flexible tube

The wrist orthosis was driven by TSAs. Embedding strings directly onto the sleeve was not ideal — it would increase friction during twisting. String twisting was required since the fixed string length TSA configuration was used and all strings were in the twisting zone. The end of the strings were attached above the wrist, allowing for the rotation of the wrist when the strings contract. The design components of a single TSA assembly are shown in Fig. 7.4. Inspired by the work in [127], the TSA was installed in a flexible tube. The flexible tube helped with reducing the friction and wear on the the sleeve as the strings twist. The tube cannot be too rigid to restrict movement of the wrist in PS and cannot be too flexible to get crumbled. The PS tube was routed under the FE and AA TSA lines, as shown in Fig. 7.1. Two flexible tubes with a low turning radius and high flexibility were used (McMaster Carr: 3902N288, 1944T76) of outer diameter of 5 mm and 6 mm. The tube was attached to the sleeve using a sewing thread. Notice that the flexible tube did not go all the way to the attach hook. This clearance allowed for the contraction of the TSA which induced motion to the wrist. In addition, given that the wrist was a complex joint, this arrangement ensured that the wrist were not constrained and allowed for free movement when ADLs were performed.

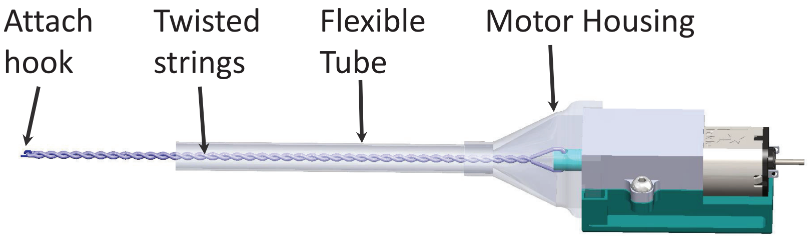

Figure 7.4: Single TSA motor assembly, showing the design of the housing and the inclusion of the flexible tube. The tube was designed to be shorter than the length of the strings to allow for the translation when twisting occurred.

7.3.2 TSA motor

The choice of the TSA motor was driven by the ability of the motor (1) to provide enough torque for the loads required for ADLs and (2) operate fast enough that it does not make the movements of the wrist too slow and unnatural. Using stiff strings (0.7 mm diameter, Piscifun Onyx Braided Fishing Line), the contraction and time duration was measured for a 30:1 gear ratio motor (ServoCity: 638103). As shown in Fig. 7.5(a), the motor could actuate more than 30 N of load when the stiff strings are used. The time duration was large, with the actuation starting at 20 seconds at low loads, rising to over 40 seconds. Fig. 7.5(b) shows the transient resistance change when two 10-ply SCP strings were utilized in the TSA. The length of the SCP string was 20 cm, and the SCP string was under 700 g load. Since lower time duration was ideal, the 15:1 motor (Pololu: 4785) was used in this study.

7.3.3 Motor placement

The placement of the motors on the forearm and the location of the attachment points for the strings on the wrist could greatly affect the actuation performance. Two possible configurations for the actuation were considered: single-motor actuation and double-motor actuation.

In single-motor configuration, motors and attachment points are located at the midpoint of the wrist for each DOF. This means that for each DOF, two motors will be activated, with one contracting and the one opposite side extending. Fig. 7.6(a) shows the side placement of the single-motor configuration, with the attachment point and the motor located centrally on the forearm on both the flexion/extension and the adduction/abduction. As shown in Fig. 7.6(b), motor M_1 and M_4 actuate flexion and

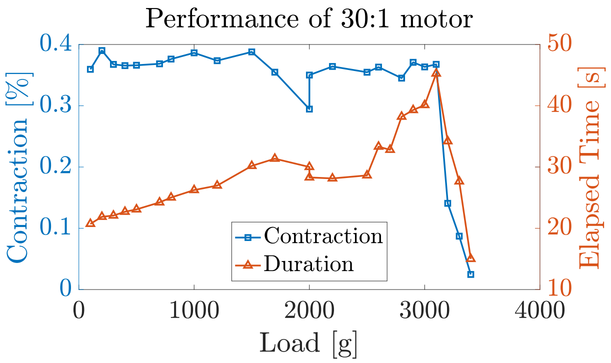

(a)

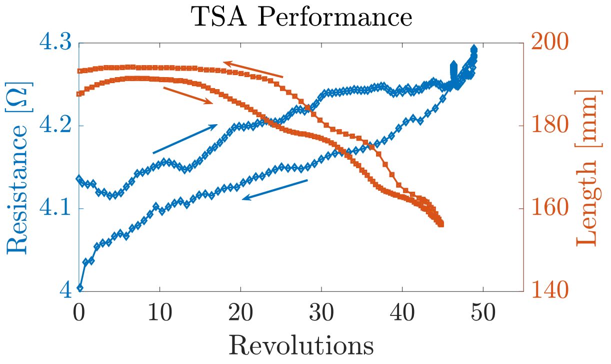

(b)

Figure 7.5: The load performance for a 30:1 gear ratio motor. (a) Using stiff fishing lines, the 30:1 gear ratio motor could actuate with high contraction up to 30 N of load but required a longer time duration. (b) Using 10-ply SCP strings, the change in resistance as the motor were activated.

extension while M_2 and $M3$ activate adduction and abduction.

In the double-motor configuration, motors are offset from the center axis by some value p and the attachment points are offset by d from the central axis, as shown in Fig. 7.6(c). This arrangement allows for the activation of each DOF by the simultaneous actuation of four motors – two motors for flexion and two motors for abduction. This arrangement allows for the usage of four motors for the same DOF. As shown in Fig. 7.6(d), M_1, M_2 activated flexion and M_3, M_4 activate extension. Equivalently, M_1, M_4 activated adduction and M_2, M_3 activated abduction. This configuration allows for the reduction of the forces being required for the motors to produce for the

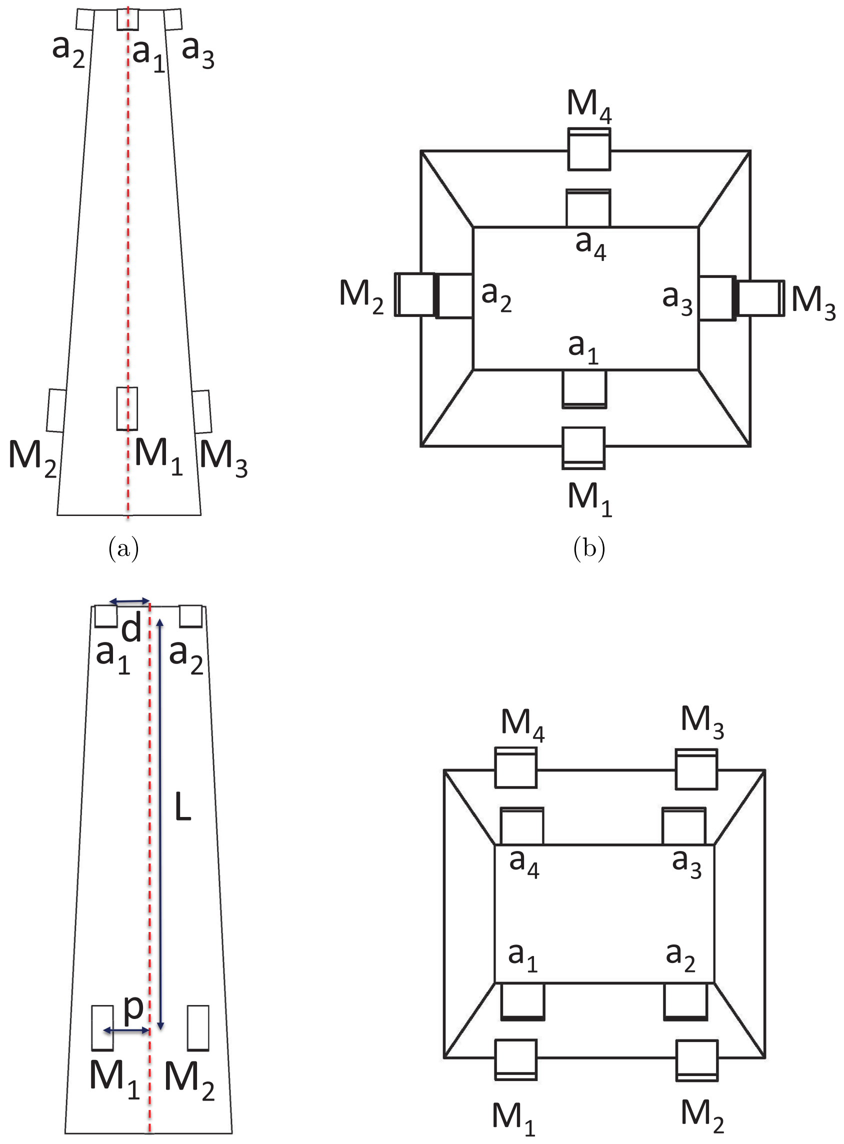

(a) (b)

(c) (d)

Figure 7.6: The placement configurations, showing the location of the motors on the forearm. (a) side view of the single-motor configuration, (b) top view of the single-motor configuration, (c) side view of the double-motor configuration, and (d) the top view of the double-motor configuration.

TSAs.

The impact of the offset in the double-motor activation configuration is analyzed in the following: From Fig. 7.6(c), the angle from the vertical of the motor and the attachment points can be defined as:

$$\theta = \tan^{-1}\left(\frac{p-d}{L}\right), \tag{7.1}$$

where d is the offset of the attachment point from the centerline of the the wrist, p is the shift of the motor from the centerline and L is the separation of the attachment points from the motors.

It is clear from Eq. (7.1) that when $p = d$, $\theta = 0$. Taking the force produced by the motor to be F and the force required to perform ADLs for each DOF as F_{req}, it can be shown that

$$F = \frac{F_{\text{req}}}{2\cos(\theta)}. \tag{7.2}$$

When θ is zero, F becomes exactly half of F_{req}. For $\theta \leq 60°$, F is less than F_{req}. As a result, having this configuration reduces the forces experienced by the strings.

It is important to note that both configurations uses the same number of actuators. The PS DOF is unaffected by the choice of the two designs. While clearly advantageous in reducing the forces in the strings, the single motor configuration was implemented instead of the double motor configuration. Stiff strings (Piscifun Onyx Braided Fishing Line) are utilized for the FE and the PS – force output is not a limitation. SCP strings are used in the AA movement as less force output is required. Furthermore, TSAs with SCP strings could have position self-sensing capability.

The placement of the TSA for the PS DOF was achieved by angling the motors 45° to the horizontal and a half a helical revolution from the attachment point. All motors were located a distance L from the attachment points. Increasing the number of helical revolutions from the attachment point increased the torque requirements.

7.3.4 Attachment mechanism

All motors were attached to the forearm through a velcro (hook-and-loop fastener) strap. The motor housing was designed to have a velcro strap clearance at the bottom. This approach not only allowed for ease of wearing and taking off the device but also allowed for the simplicity in adjusting the location of the motors around the forearm. This characteristic allowed for the ease of the device to fit with patients of different forearm diameters. The thumb and index finger wear (North Coast Medical) contained the loops all over the body (soft end of the velcro). The motor attachments were then securely attached to the back of the hooks (hard end of velcro). These assemblies were attached to the designed locations on the wrist. The utilization of the hook-and-loop for both the motor attachments and the motor fasteners enabled the simplicity in changing the motor or attachment locations. In fact, the two actuation configurations could be easy achieved in the same device by shifting the attachment point locations and positions of the motors. Below the motor velcro strap, a small strap of EcoFlex (00-30) was used. The EcoFlex was compliant and helped increase the friction between the motor strap and the forearm. The increased friction eliminated the sliding of the motors when torques and forces were applied to the wrist.

7.3.5 Electrical design and control

TSAs are advantageous due to their compliance and flexibility in application of forces from a distance. One of the main limitations is that TSAs are unidirectional force application devices. Since bi-directional movement of the wrist was required for all DOF for the performance of ADLs, two motors were then used for each set of movements. The control scheme ensured that the coupling between the two motors was accurately controlled in relation to the DOF. When one TSA was contracting, the second TSA was extending at the same rate to ensure that there were no residual forces experienced by the strings. In addition, the resistance of the SCP strings could be used to estimate the adduction/abduction movement.

The length of the strings as the motor is activated is given by:

$$X = \sqrt{L^2 - (\theta r)^2}, \tag{7.3}$$

where r is the radius of the strings, $\theta = 2n\pi$ with n the number of motor rotations. From Eq. (7.3), the displacement change can be defined as $\Delta X = L - X$. This displacement change can then be matched for both TSAs that actuate each DOF. In particular,

$$\Delta X = r_{\text{wrist}} \Delta \beta, \tag{7.4}$$

where β is the angle of the wrist for the specific DOF and r_{wrist} is the radius of the specific DOF being actuated.

While ΔX can be achieved by specifying the number of rotations, there was no sensor installed to measure the angle of the wrist. As a result, for this iteration of the orthosis, an open-loop control was used. Closed-loop control will be implemented for the adduction/abduction in future iterations of the device. The resistance measured from the SCP strings will be used as the feedback signal. The correlation between resistance and length will be used as a ground truth to confirm the travel specified by the number of rotations. A reliable method to read the resistance was tested. The control unit was driven by a Teensy®4.1 Development Board. The board was chosen for the high clock speed and high number of PWM pins that are required to read and control 6 encoders and read resistance measurements from two SCP strings.

7.4 Experiments

The performance of the orthosis was tested in two experiments; 1) measuring the range of motion of the three DOF using a customized forearm prosthetic and 2) performing tests on a healthy human subject to show the ability of the device to induce motion without muscle activity.

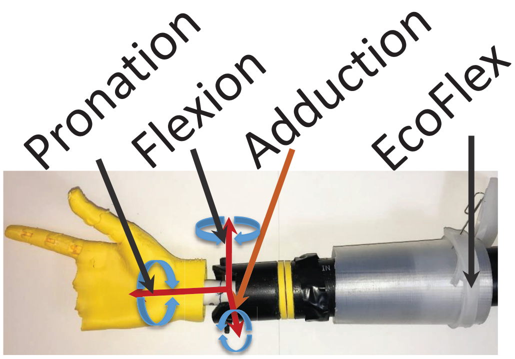

Figure 7.7: Measuring the range of motion (RoM) for all the degrees of freedom using the prosthetic forearm.

7.4.1 Range of motion

The range of motion tests demonstrated that the necessary ADLs can be performed. Testing using a prosthetic forearm (Fig. 7.7) was key to decouple the DOF which ensured that the testing was performed for the specific motion and helped avoid involuntary interference of a human test subject.

Table 7.1: Range of motion results orthosis

Degree of Freedom	Overall [°]	Positive [°]	Negative [°]
Flexion/Extension (FE)	115.1	63.4	52.1
Adduction/Abduction (AA)	74.1	35.2	38.2
Pronation/Supination (PS)	-	65.2	52.7

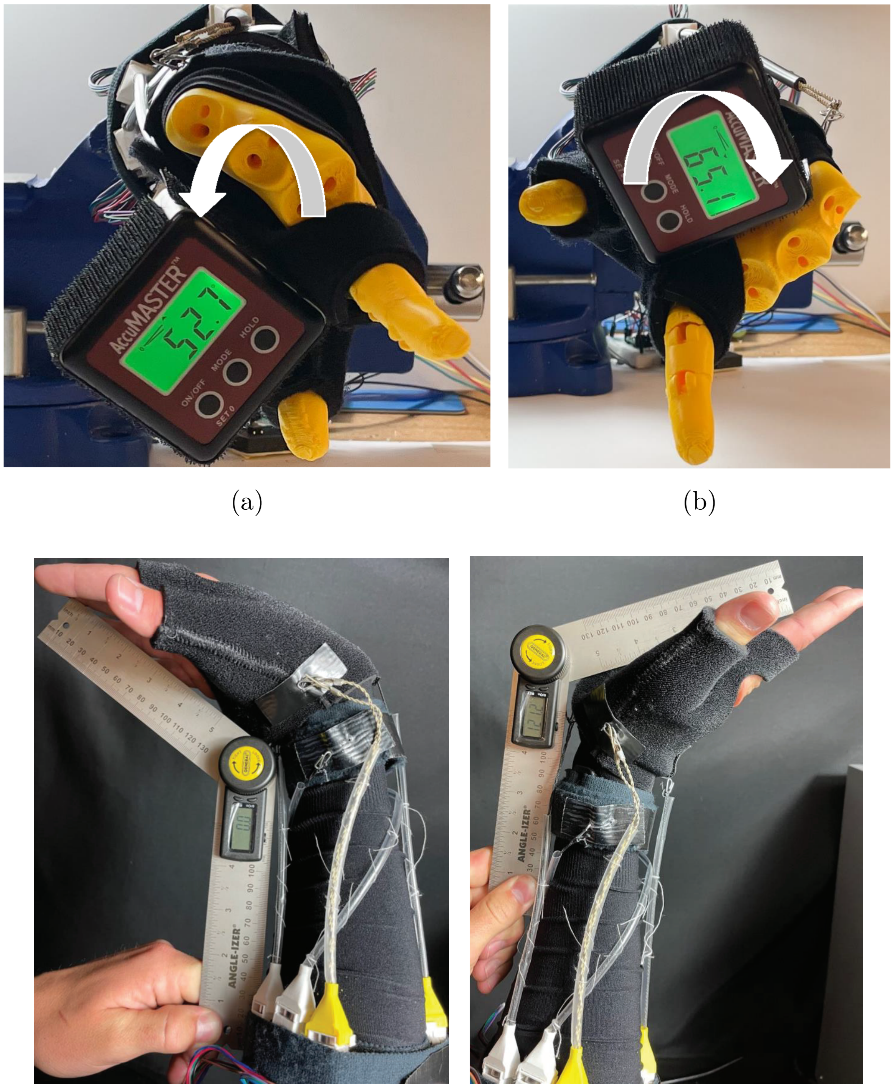

(a) (b)

(c) (d)

Figure 7.8: (a) Measuring pronation, (b) measuring supination. Both PS are measured from neutral axis, when the inclinometer is reading 0°. Measuring RoM starting from (c) maximum flexion to (d) maximum extension, with device worn by a human subject.

For all the DOF, starting at the neutral position, the positive and negative motion were performed and recorded. The PS DOF were measured using an AccuMaster inclinometer, starting from neutral position, supination range was measured (Fig. 7.8(a)) as well as pronation (Fig. 7.8(b)). The range of motion for all the DOF are not symmetric [128], as shown in Table 7.1.

The last process was to measure the range of motion from the maximum negative angle to the maximum positive motion. The overall RoM for FE was 115.1° and 74.1° for AA.

7.4.2 Human subject test

This test demonstrated that the orthosis was capable of providing the necessary motion to the wrist with the passive tension being produced. Fig. 7.8(c) and (d) shows an overall range of 121.2° for the FE DOF when the device was worn by a human subject. In the setup, the human subject was vertically oriented. The overall RoM was 19.8° in AA, and 78.2° in PS. Neglible EMG signals showed that human subject was not activating muscles when the RoM was measured. The human subject study conducted was approved by the Institutional Review Board (IRB) at the University of Nevada, Reno.

7.5 Conclusion

This chapter presented the *first* wearable orthosis device that actuated all three DOF of the wrist using TSAs — FE and PS used stiff fishing lines, while AA utilized the compliant SCP strings. The range of motion of the orthosis was sufficient to perform necessary ADLs [129, 130]. Further, it was shown that the device can actuate while donned by human test subject.

Part III

Modeling and Control of AWARD

CHAPTER 8

MODELING OF AWARD

8.1 Introduction

To facilitate the control and state estimation of AWARD, it is essential that both the kinematic model and the dynamic model be well understood. For this purpose, the model for a finger was derived. Since the configuration of the fingers are similar, deriving the models for each finger allowed for the application of the model to all the fingers and hence AWARD. Previous studies have applied a similar approach in the derivation of kinematic and dynamic models [36, 131].

8.2 Finger Modeling

It is challenging to utilize a closed form model when modeling soft wearable devices. This is in part due to the difficulty in measuring the device to body forces and torques. In addition, wearable devices are prone to slipping and sliding on the users limb (a phenomenon called migration). Further, the deformation of the fabrics or soft materials used can be difficult to model. Despite these challenges, modeling is performed to provide a basis of the control. Key parameters were identified using data collected from the device due to the difficulty of knowing these parameters in advance. The kinematics model is presented first and then the dynamic model is outlined.

8.2.1 Kinematics model

Each finger was modeled as a serial kinematic chain with three revolute joints and three links representing the DIP, PIP and the MCP joints, as shown in Fig. 8.1. The thumb was modeled as two serial chains. It is noted that the rotational joint at the MCP has a single degree of freedom — the adduction/abduction of each finger was assumed to be small enough that it was negligible. This assumption was valid since the mannequin test bed setup only had one rotational degree of freedom. In addition, when the embedded tendons were located as close as possible to the center-line, non-planar motion was limited. Previous studies have also used this assumption [132]. The Denavit–Hartenberg (DH) parameters and the subsequent DH table were then used to derive the forward kinematics. In this way, the position of the finger tip was computed when the finger joint angles were known. A hand model was then constructed by combinations of finger models representing each finger motion.

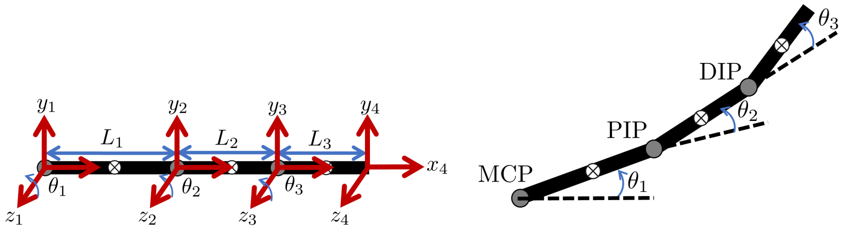

(a) (b)

Figure 8.1: The schematic of the kinematic definition of a single finger. (a) The locations for the frames that allow the usage of DH approach to kinematics. (b) The configuration showing the parameters used to derive the dynamics of each finger.

The DH convention was used for the location of the frames as shown in Fig. 8.1(a) when the finger is at its fully extended state. Fig. 8.1(b) shows the finger after some arbitrary actuation. The DH table derived from these frames is shown in Table 8.1.

Table 8.1: The DH parameters from the frames shown in Fig. 8.1.

Link	a_j	d_j	α_j	θ_j
1	L_1	0	0	$\theta_1^\star$
2	L_2	0	0	$\theta_2^\star$
3	L_3	0	0	$\theta_3^\star$

The forward kinematics is then computed by

$$\boldsymbol{T}_4^1 = \boldsymbol{A}_2^1 \boldsymbol{A}_3^2 \boldsymbol{A}_4^3 = \begin{bmatrix} \mathbf{R} & \mathbf{p} \\ \mathbf{0} & 1 \end{bmatrix} \tag{8.1}$$

where $\boldsymbol{T}_4^1$ is the composite homogeneous transformation from frame 4 to frame 1, $\boldsymbol{A}_{j+1}^j$ is the homogeneous transformation matrix from frame j to frame $j+1$, $\boldsymbol{p} = [x_{\text{ft}} \; y_{\text{ft}} \; 0]$ is the position of the finger tip with respect to the base frame – frame 1. In addition, $j \in (1, 2, 3)$. Notice that the z-coordinate will always be zero since it was assumed that the MCP joint only possess a single in-plane degree of rotation.

Each finger was actuated by two antagonistic TSAs – one for flexion and one for extension because the TSAs are unidirectional. Since there are three links and only two actuated TSAs, it was clear that θ_j cannot be controlled independently — they are coupled. The movement was achieved by controlling the length of each TSA. The joint angle limits were considered to be similar to the average human motion range — maximum angle of 100°, 105°, and 85° for MCP (θ_1), PIP (θ_2) and DIP (θ_3), respectively [95]. It is necessary to determine the kinematic relationship between the TSA lengths and the joint angles.

Let q_n represent the length of the tendons embedded in the glove, where $n \in (1, 2m)$ with m representing the number of actuated fingers. Specifically, q_1 is the flexion tendon and q_2 is the extension tendon. From Fig. 8.2 and Fig. 8.3, it can be

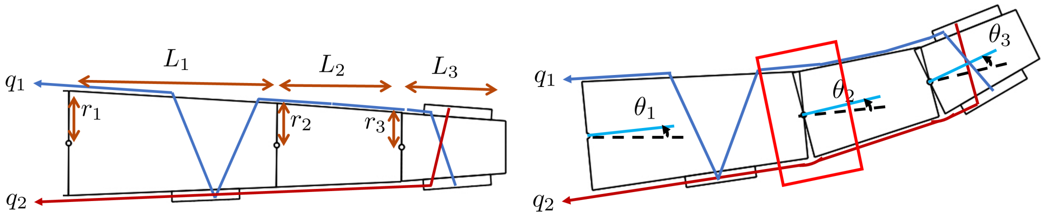

(a) (b)

Figure 8.2: The schematic of the tendons for both flexion and extension — blue is the flexion tendon and red is the extension tendon. (a) The straight configuration of a finger. (b) The actuated configuration when the joint angles are not zero. The red boxes signify where closer attention needs to be paid.

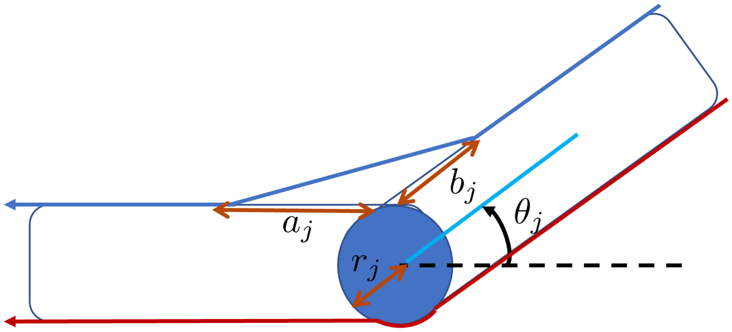

Figure 8.3: The effect the tendons when the finger joints are not zero.

shown that the tendon lengths are given by

$$\begin{aligned} q_1 &= q_{1,0} + \sum_{j=1}^{3} \sqrt{a_j^2 + b_j^2 - 2a_j b_j \cos(\pi - \theta_j)}, \\ q_2 &= q_{2,0} + r_1\theta_1 + r_2\theta_2 + r_3\theta_3, \end{aligned} \tag{8.2}$$

where a_j, b_j are geometric parameters for each joint, $q_{1,0}, q_{2,0}$ are the initial lengths of the tendons. It is noted that θ_j is in radians in this Eq. (8.2). Due to the stretching of the fabric, these parameters are difficult to measure or estimate even though they are design parameters. As a result of this difficulty, the parameters were estimated by performing an optimization from the collected data.

Taking the time derivative of Eq. (8.2) gives

$$\dot{\boldsymbol{q}} = \boldsymbol{H}(\boldsymbol{\theta})\dot{\boldsymbol{\theta}}, \tag{8.3}$$

where $\dot{\boldsymbol{q}} = [\dot{q}_1 \;\; \dot{q}_2]^\top$, $\dot{\boldsymbol{\theta}} = [\dot{\theta}_1 \;\; \dot{\theta}_2 \;\; \dot{\theta}_3]^\top$, $\boldsymbol{H}(\boldsymbol{\theta}) \in \mathbb{R}^{2\times 3}$ is the Jacobian matrix from joint space to the tendon space. $\boldsymbol{H}(\boldsymbol{\theta})$ is also known as the routing/coupling matrix. Specifically, $\boldsymbol{H}(\boldsymbol{\theta}) = \frac{\partial \mathbf{q}}{\partial \boldsymbol{\theta}}$. Therefore the Jacobian matrix is given by

$$\boldsymbol{H}(\boldsymbol{\theta}) = \begin{bmatrix} \frac{-a_1 b_1 \sin(\theta_1)}{\sqrt{a_1^2+b_1^2+2a_1 b_1 \cos(\theta_1)}} & \frac{-a_2 b_2 \sin(\theta_2)}{\sqrt{a_2^2+b_2^2+2a_2 b_2 \cos(\theta_2)}} & \frac{-a_3 b_3 \sin(\theta_3)}{\sqrt{a_3^2+b_3^2+2a_3 b_3 \cos(\theta_3)}} \\ r_1 & r_2 & r_3 \end{bmatrix}. \tag{8.4}$$

If $\boldsymbol{H}(\boldsymbol{\theta}) = \boldsymbol{H}$, that is $\boldsymbol{H}$ is constant and does not depend on the joint angles, then $\boldsymbol{q} = \boldsymbol{H\theta}$. It follows from Eq. (8.3) that given the linear velocities of the tendons, the angular joint velocities can be computed as

$$\dot{\boldsymbol{\theta}} = \boldsymbol{H}(\boldsymbol{\theta})^{+}\dot{\mathbf{q}}, \tag{8.5}$$

where $\boldsymbol{H}(\boldsymbol{\theta})^{+}$ is the pseudo-inverse of $\boldsymbol{H}(\boldsymbol{\theta})$. However, it can be observed in Eq. (8.5) that to compute $\dot{\boldsymbol{\theta}}$, it is necessary that $\boldsymbol{\theta}$ is already known. This coupling will be revisited in the control section and demonstrate how it was tackled. Due to the non-trivial threading of the tendons in the soft glove, stretching of the fabric, the geometric parameters were difficult to measure.

The torque at the joints is then given by

$$\boldsymbol{\tau}_{\text{ext}} = \boldsymbol{H}(\boldsymbol{\theta})^\top \boldsymbol{T}, \tag{8.6}$$

where $\boldsymbol{\tau}_{\text{ext}} = [\tau_1 \;\; \tau_2 \;\; \tau_3]^\top$ represent the joint torques and $\boldsymbol{T} = [T^f \;\; T^e]^\top$ represents the tensions in the flexion tendon , T^f, and in the extension tendon, T^e. It will be shown in the next section that $\boldsymbol{T}$ is a function of the tendon lengths that are driven by the TSAs.

8.2.2 Dynamics model

The dynamic model of AWARD was obtained by deriving the model for each finger motion and then considering fingers as independent rigid bodies. Similar to the kinematic model, planar motion was assumed for the MCP joint. The dynamic model of each finger is given by

$$\boldsymbol{M}(\boldsymbol{\theta})\begin{bmatrix}\ddot{\theta}_1\\ \ddot{\theta}_2\\ \ddot{\theta}_3\end{bmatrix}+\boldsymbol{C}(\boldsymbol{\theta})\begin{bmatrix}\dot{\theta}_1^2\\ \dot{\theta}_2^2\\ \dot{\theta}_3^2\end{bmatrix}+\boldsymbol{B}(\boldsymbol{\theta})\begin{bmatrix}\dot{\theta}_1\dot{\theta}_2\\ \dot{\theta}_1\dot{\theta}_3\\ \dot{\theta}_2\dot{\theta}_3\end{bmatrix}+\boldsymbol{G}(\boldsymbol{\theta})+\boldsymbol{\tau}_{\mathrm{f}}=\boldsymbol{\tau}_{\mathrm{ext}}, \tag{8.7}$$

where $\boldsymbol{M}(\boldsymbol{\theta}) \in \mathbb{R}^{3\times3}$ is the inertia matrix, $\boldsymbol{C}(\boldsymbol{\theta}) \in \mathbb{R}^{3\times3}$ is the centrifugal, $\boldsymbol{B}(\boldsymbol{\theta}) \in \mathbb{R}^{3\times3}$ is the Coriolis matrix, $\boldsymbol{G}(\boldsymbol{\theta}) \in \mathbb{R}^{3\times1}$ is the gravity vector, $\boldsymbol{\tau}_{\mathrm{f}} \in \mathbb{R}^{3\times1}$ is the torques that relates to the tendon friction and flexibility and $\boldsymbol{\tau}_{\mathrm{ext}} \in \mathbb{R}^{3\times1}$ is the total required input joint torque.

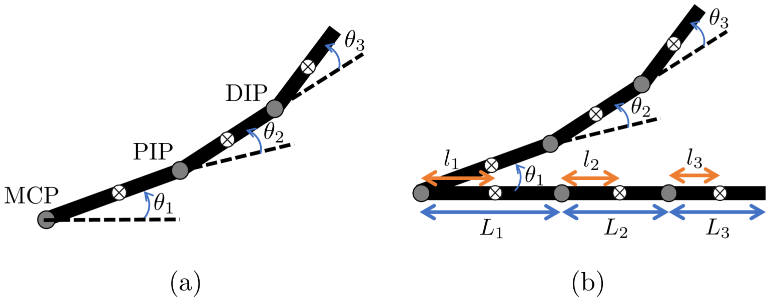

Figure 8.4: (a) The schematic of the kinematic definition of a single finger. The finger is modeled as a serial kinematic chain with three revolute joints and three links. (b) The configuration showing the parameters used to derive the dynamics of each finger.

$\boldsymbol{M}(\boldsymbol{\theta})$, $\boldsymbol{C}(\boldsymbol{\theta})$, $\boldsymbol{B}(\boldsymbol{\theta})$ and $\boldsymbol{G}(\boldsymbol{\theta})$ can be derived by using the Lagrange-Euler approach. The parameters used in these derivations are shown in Fig. 8.1(b). The Lagrangian is given by $\mathcal{L} = K - P$, where K is the kinetic energy and P is the potential energy of the system. Then the equations of motions can be derived from

$$\frac{d}{dt}\frac{\delta \mathcal{L}}{\partial \dot{\theta}_j} - \frac{\partial \mathcal{L}}{\partial \theta_j} = \tau_j. \tag{8.8}$$

The kinetic energy, K, is given by

$$K = \frac{1}{2} m_j v_j^\top v_j + \frac{1}{2} \omega_j^\top I_j \omega_j, \tag{8.9}$$

where $v_j = J_{v_j}(\theta)\dot{\theta}$, $\omega_j = J_{\omega_j}(\theta)\dot{\theta}$ and the moment inertia is given by

$$I_j = \frac{1}{4} m_j \left(\frac{d_j}{2}\right)^2 + \frac{1}{3} m_j L_j^2, \tag{8.10}$$

for $j \in (1, 2, 3)$. Eq. (8.9) can be expressed as $K = (1/2)\dot{\theta}^\top M(\theta)\dot{\theta}$ [133]. The complete derivation and the full form of Eq. (8.7) is shown in Appendix A.

$\boldsymbol{\tau}_\mathrm{f}$ is then defined as

$$\boldsymbol{\tau}_\mathrm{f} = \boldsymbol{w}\dot{\boldsymbol{\theta}}, \tag{8.11}$$

where $\boldsymbol{w} = [w_1\ w_2\ w_3]^\top$ and w_1, w_2, w_3 are constants for each of the three joints. As can be seen, these are defined as damping torques — it is noted this term need to be added since the Euler-Lagrange were derived based on a conservative system. In reality, the finger is always affected by frictional forces within the joints. In this work, the motor torque, τ_m was attained through the measurement of the input motor current as an estimate of the tensions on the TSA strings. Specifically,

$$\tau_\mathrm{m} = k_\tau i_\mathrm{m}, \tag{8.12}$$

where k_τ is the motor torque constant and i_m is the current measured from motor. It is noted that the dry friction of the motor is taken into account by one of two approaches: 1) using the difference between the no-load current and the current during use, or 2) computing the dry friction torque as $\tau_{fr} = k_\tau i_{fr}$, where τ_{fr} is the dry friction torque and i_{fr} is the free run current. Removing the contribution of friction on the torque ensured that the considered torque was only the one that was due to the tension of the tendons. Then the force at the fingertips can be computed by using the dynamic model of the TSA, which is given by Eq. (3.3). For better reading, equation is presented again

$$J\ddot{\Psi} + b_{\Psi}\dot{\Psi} + \tau_{\mathrm{c}}\mathrm{sgn}(\tau_{\mathrm{m}}) + \tau_{\mathrm{t}} = \tau_{\mathrm{m}}, \tag{8.13}$$

where Ψ is the motor angle and the twisting torque τ_{t} is given by Eq. (3.4)

$$\tau_{\mathrm{t}} = Fr^2\Psi/X. \tag{8.14}$$

Assuming steady conditions, then the force at the fingertip due to the TSA is given by

$$F = \frac{X(\tau_{\mathrm{m}} - \tau_c)}{r^2\Psi}. \tag{8.15}$$

Then the tension at the motor connection is given by

$$T = (1+\phi)F, \tag{8.16}$$

where ϕ is the friction between the tendon and the fabric. Then Eq. (8.6) and Eq. (8.16) are used to define the external torque, $\boldsymbol{\tau}_{\mathrm{ext}}$. To further understand the contribution of the motor torque to each joint, the threading design has been considered.

8.2.3 Torque analysis

The implemented threading approach determined the tensions in the tendons. In turn, the tensions in the tendons determined the torques required for actuating the finger motions. Various threading approaches were examined during the development process of AWARD. As mentioned in Section 5.2.3, the threading design was selected to minimize fabric deformation and friction while ensuring that the fingers can attain repeated actuation or motion from fully extended to fully closed. The schematic of the final threading approach used for AWARD is shown in Fig. 8.5.

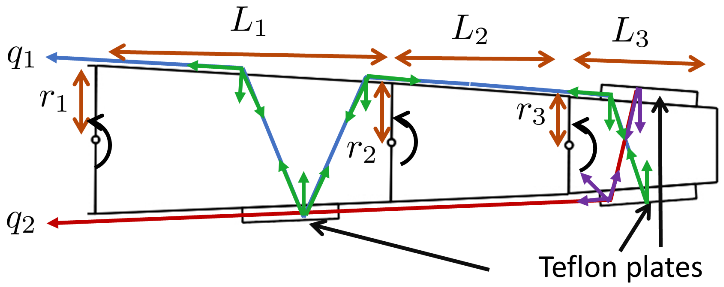

Figure 8.5: A schematic representation of the threading approach used in AWARD. The zigzagging approach allowed for the finger facing forces to limit the deformation of the fabric. The teflon plates concentrate the forces from the tendons allowing for the generation of torques to induce finger motions.

Each finger was actuated in flexion and extension. The torques induced by the flexor and the extensor tendons will be different and must be analyzed separately. First, the torques in each joint during flexion was analyzed.

Let a_i represent the anchor points of the tendons to the glove, $T_{i,f}$ represent the tension in the tendon, d_i is the perpendicular distance of the anchor point from the joint where $i \in (0, 1, 2, 3)$, τ_j is the joint torque, L_j is the length of the phalangeal where $j \in (1, 2, 3)$. Let F_i^N be force that is normal to the finger and F_i^P be the force that is parallel to the finger. Let the angle that $T_{1,f}$ makes with the vertical be γ, the angle that $T_{2,f}$ makes with the vertical be β and the angle that $T_{3,f}$ makes with the vertical be α. These definitions, shown in Fig. 8.6, allowed for the analysis of the torques that contribute to finger flexion.

It can be shown from Fig. 8.6 that $F_i^N = T_{i,f} \cos(\cdot)$ and $F_i^P = T_{i,f} \sin(\cdot)$. Decom-

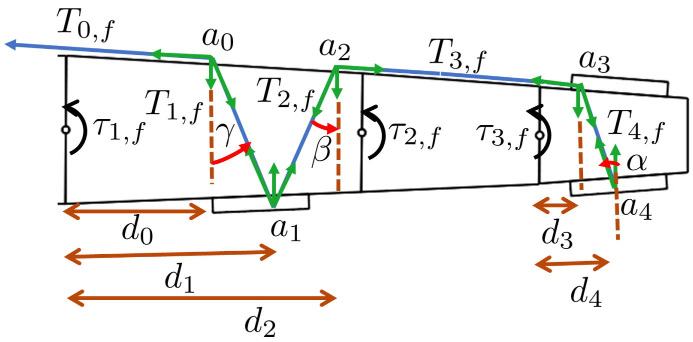

Figure 8.6: Definitions of variables of interest for the analysis of torques in the finger joints during flexion.

posing the forces and computing the torques, the resulting torques for each joint can be expressed as

$$\begin{cases} \tau_{1,f} = T_{0,f}r_1 + T_{1,f}(d_1 - d_0)\cos(\gamma) - 2T_{1,f}r_1\sin(\gamma) \\ + 2T_{2,f}r_1\sin(\beta) + T_{2,f}(d_1 - d_2)\cos(\beta), \\ \tau_{2,f} = T_{3,f}r_2, \\ \tau_{3,f} = T_{3,f}r_3 - 2T_{4,f}r_3\sin(\alpha) + T_{4,f}(d_4 - d_3)\cos(\alpha), \end{cases} \tag{8.17}$$

where $\tau_{j,f}$ represents the joint torques in flexion. It is important to note that $T_{0,f} > T_{1,f} > T_{2,f} > T_{3,f}$, where $T_{0,f}$ is equivalent to the measured tension through the motor torque. Since a_i and d_i are design parameters, α, β, γ are design parameters too. It can be shown that the torques will be positive depending on these design variables.

Due to lack of compact sensors, it was difficult to measure the tension within the tendons. If we assume that the threading does not produce very sharp bends, it is feasible to estimate that the tension through the tendon was the same throughout. Specifically, assume that $T_{0,f} = T_{1,f} = T_{2,f} = T_{3,f} = T^f$. Then Eq. (8.17) can be written as

$$\begin{cases} \tau_{1,f} = T^f r_1 + T^f (d_1 - d_0) \cos(\gamma) - 2T^f r_1 \sin(\gamma) \\ + 2T^f r_1 \sin(\beta) + T^f (d_1 - d_2) \cos(\beta), \\ \tau_{2,f} = T^f r_2, \\ \tau_{3,f} = T^f r_3 - 2T^f r_3 \sin(\alpha) + T^f (d_4 - d_3) \cos(\alpha). \end{cases} \tag{8.18}$$

Eq. (8.18) can be checked by setting $\gamma = \beta = \alpha$. In this configuration, then $d_1 = d_0$, $d_1 = d_2$, $d_3 = d_4$. Since $\sin(0) = 0$, in Eq. (8.18) the flexion torques are then scaled by the radius of the joints, which is the expectation.

The torques required for extension are derived in a similar way used in deriving the flexion torques. The schematic of the variables of interest are defined as shown in Fig. 8.7.

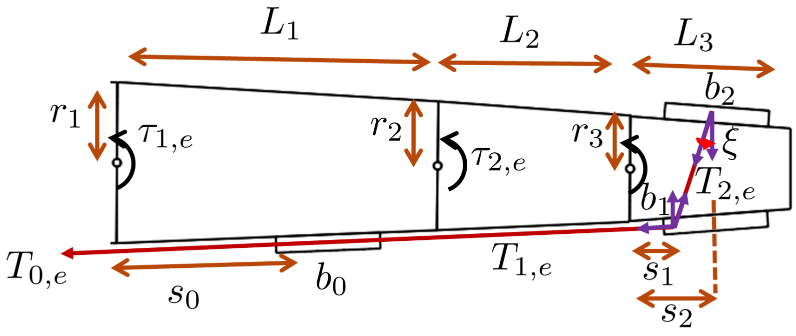

Figure 8.7: Key variable definitions during the extension of the fingers.

It can be shown that the torques due to the extensor tendon can be expressed as

$$\begin{cases} \tau_{1,e} = -T_{0,e} r_1, \\ \tau_{2,e} = -T_{1,e} r_2, \\ \tau_{3,e} = 2T_{2,e} r_3 \sin(\xi) + T_{1,e}(s_1 - s_2) \cos(\xi) - \; T_{2,e} r_3, \end{cases} \tag{8.19}$$

where $\tau_{j,e}$ is the torque due to the extensor tendons. Assuming that there anchor points display minimum sharp curvatures to the tendons, then the tension in the tendon is consistent throughout. That is $T_{0,e} = T_{1,e} = T_{2,e} = T^e$. Then Eq. (8.19) can be written as

$$\begin{cases} \tau_{1,e} = -T^e r_1, \\ \tau_{2,e} = -T^e r_2, \\ \tau_{3,e} = 2T^e r_3 \sin(\xi) + T^e(s_1 - s_2)\cos(\xi) - \ T^e r_3. \end{cases} \tag{8.20}$$

Setting $\xi = 0$, then $s_1 = s_2$ resulting to $\tau_{3,e} = - \ T^e r_3$, demonstrating that the joint torques are again scaled according to the radii of the joints. The total torque, τ_j, for each joint as a result of the extensor and the flexor is then given by

$$\tau_j = \tau_{j,f} + \tau_{j,e}. \tag{8.21}$$

Clearly, τ_j are functions of the tensions in the tendons and the design parameters. Due to the difficulty in sourcing and installing compact tension sensors in the tendons, attaining accurate tension measurement is challenging. Additionally, it was difficult to design a glove that fits the fingers snugly and as a consequence, precisely selecting these design parameters that stay fixed during usage. Understanding the design parameters and an estimation of the tensions in the tendons allowed for an informed design experimentation. As it is evident, Eq. (8.21) is highly non-linear and is dependent on parameters that are difficult to measure for a soft wearable device. Consequently, Eq. (8.6) was used to compute the joint torque contributions. It is evident that the torques on the joints are loosely scaled according to the apparent radii of the surfaces they are rubbing on [134, 135]. The full model for each finger is obtained by plugging in Eq. (8.21) to the right hand side of Eq. (8.7).

It is further noted that since TSA was used, there is no minimum requirement of the tension. In traditional spooled-motor driven tendon actuation, slack is not permitted since the tendons can slide off the pulleys and result in entanglement. In that regard, it is required that $\boldsymbol{T} > \boldsymbol{0}$ all the time.

8.3 Model Identification and Validation

Unknown parameters of both the kinematic and dynamics model were identified. Specifically, the optimization was performed by using the MATLAB ® built in function `fmincon` that minimizes a constrained nonlinear multi-variable function. This function takes as arguments an objective function handle of a single variable that is to be minimized. In the following sections, the exact implementations are described for the kinematics and the dynamics.

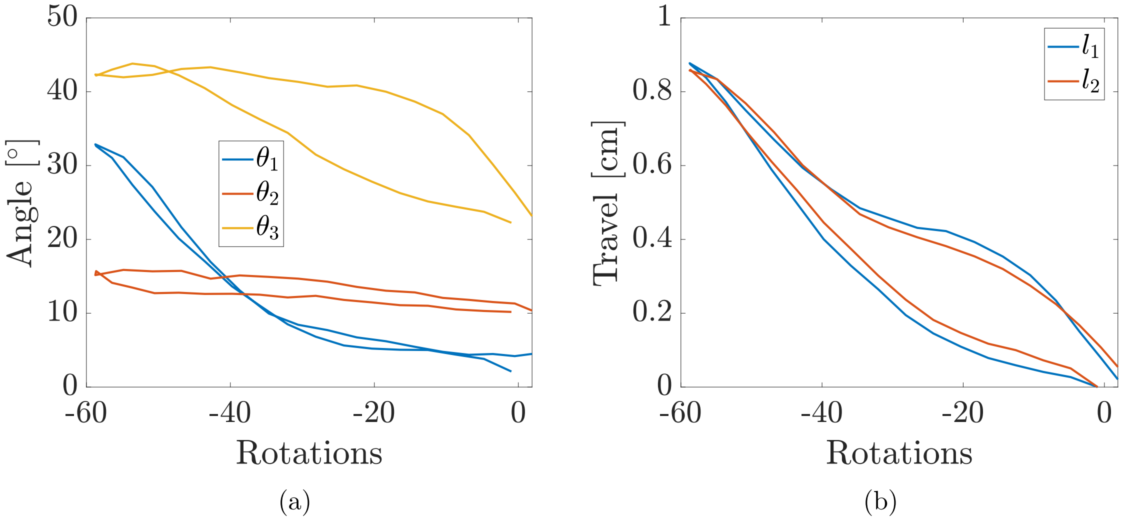

(a)

(b)

Figure 8.8: (a) The joint angles when the motor rotations were increased to 60 motor rotations. (b) The change in tendon lengths for both flexion and extension after identifying unknown parameters.

8.3.1 Kinematics

First, it is important to verify the kinematic relations between the tendon lengths and the change of the joint angles. Specifically, Eq. (8.2) has to be validated. Since the a_j, b_j are not measurable but assumed to be constant throughout the actuation range, they will be identified. Multiple datasets were collected when AWARD was in the fully extended state. Contraction and then full extension was performed. The change of the angles as the tendon lengths changed is shown in Fig. 8.8(a). The diameters of the phalanges of the hand mannequin used were measured to determine r_j. Since the change of the angles was due to a change in the tendon lengths, $q_{1,0},\ q_{2,0}$ can be ignored in this computation. Therefore, with r_j known and θ_j measured, q_2 can be computed. In-order to compute q_1, a_j and b_j must be known. Specifically, `fmincon` was implemented. Since the decrease of q_1 should be equal to the extension of q_2, the error between the two changes in the tendon lengths can be minimized hence determining $a_j,\ b_j$.

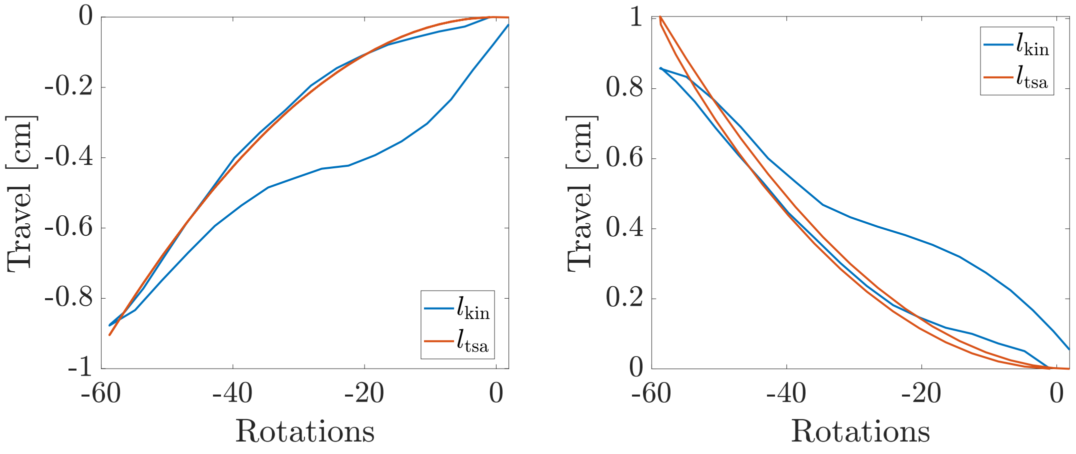

(a) (b)

Figure 8.9: The contraction of the tendons that are computed using the kinematic relationship, q_{kin}, and the expected tendon contraction computed using the TSA model, q_{tsa}. (a) Shows the contraction of q_1 and (b) Shows the contraction for q_2.

The objective function for the optimization was described to enable the minimization of the error between the contractions. The resulting identified parameters are $a_1 = 5.076$ cm, $b_1 = 5.076$ cm, $a_2 = 5.216$ cm, $b_2 = 5.216$ cm, $a_3 = 4.252$ cm, $b_3 = 4.252$ cm. The measured joint angles are shown in Fig. 8.8(a). The identified parameters were used to compute q_1 as shown in Fig. 8.8(b). The procedure to identify the parameters is summarized in Algorithm 8.1. It is important to note that the travel of the TSAs was reshaped to allow for the proper identification of the parameters and to plot Fig. 8.8(b). A comparison between the tendon lengths computed using Eq. (8.2) and contraction of the TSAs is shown in Fig. 8.9 for both q_1 and q_2. The contraction of the TSAs were computed using the model for the fixed twisted zone that is given in Eq. (5.1). For an easier read, the equation is included below:

$$\Delta x = \sqrt{L_t^2 + \Psi^2 r^2} - L_t. \tag{8.22}$$

It can be noted that there is big hysteresis at lower motor rotations for the kinematic tendon contraction while the TSA contraction demonstrates negligible hysteresis as shown in Fig. 8.9. This behavior was attributed to the stretching of the fabric. The fabric was still stretching at lower rotations while the frabric had attained maximum stretch at higher rotations, hence higher consistency.

Algorithm 8.1 *Procedure for parameter identification*

```
1. Define $r_j$, where they are measured from mannequin
2. Define $\boldsymbol{R}, \boldsymbol{\theta}$, inputs to the function
3. Define parameter space from the input of the function:
       $a_1 = \boldsymbol{R}(1),\ b_1 = \boldsymbol{R}(2),\ a_2 = \boldsymbol{R}(3),$
       $b_2 = \boldsymbol{R}(4),\ a_3 = \boldsymbol{R}(5),\ b_3 = \boldsymbol{R}(6)$
       $\theta_1 = \boldsymbol{\theta}(1),\ \theta_2 = \boldsymbol{\theta}(2),\ \theta_3 = \boldsymbol{\theta}(3)$
4. Compute $\boldsymbol{q}_1, \boldsymbol{q}_2$ using tendon kinematics relations with joint angles
5. Reshape $\boldsymbol{q}_1, \boldsymbol{q}_2$ so that they have the same change and not be antagonistic
6. Return $\boldsymbol{e} = \sum (\boldsymbol{q}_2 - \boldsymbol{q}_1)^2$
```

As noted, $a_j,\ b_j$ are assumed to be constant for all actuation. In the identification of these parameters, the measured diameters of the phalanges were treated as the ground truth that were used in the objective function. However, it was difficult to know with certainty if the diameter values translate to moment arms of the fingers during actuation. Using an external motion capture system would have provided the ground truth of the finger positions.

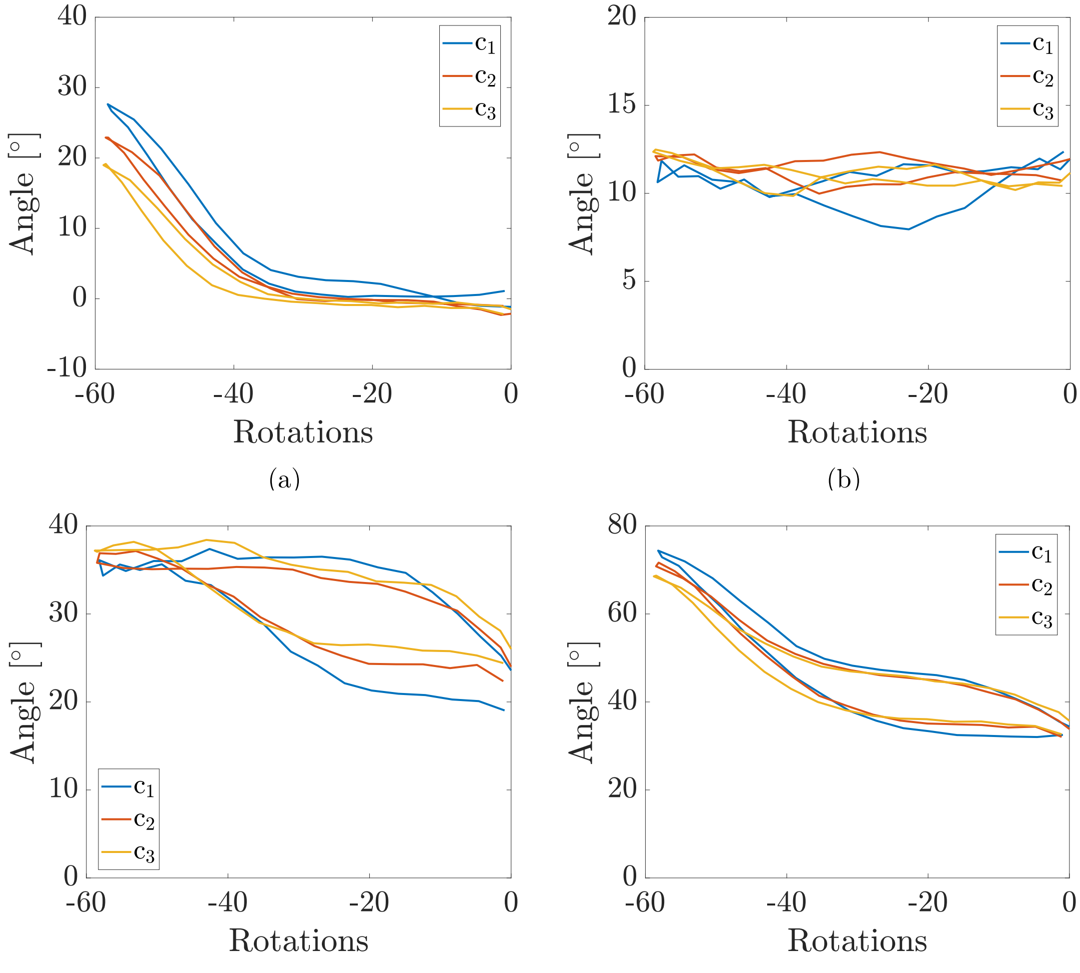

(a)

(b)

(c)

(d)

Figure 8.10: The repeatability of the motion of the fingers demonstrated by the joint measurements when three cycles were conducted where (a) shows θ_1, (b) shows θ_2, (c) shows θ_3 and (d) shows the summation of the joint angles, θ_{total}.

It is important to ensure that the kinematics of the device allows for repeatable data. Further, since the system is under-actuated (two TSA modules that drive three joints) and an uncontrollable tendon driven mechanism [136], kinematic relations of the each finger are key to allow for trajectory generation and control. In Fig. 8.10, the repeatability of the measurements using AWARD are shown. Three cycles were

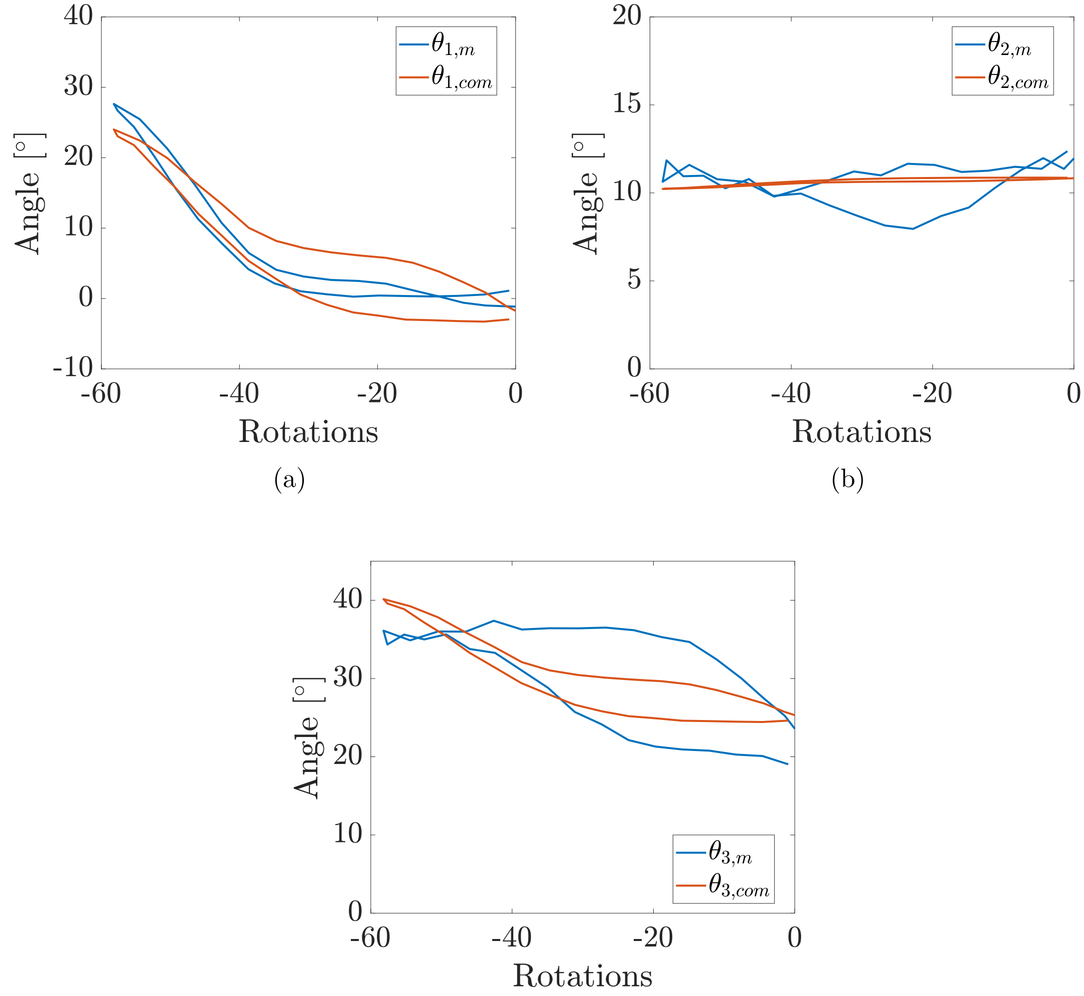

(a)

(b)

(c)

Figure 8.11: The kinematic coupling between the joint angles, θ_j, was determined using the total angle, θ_{total}. Validation of the identified coupling is shown where $\theta_{\text{j,m}}$ is the measured joint angle and $\theta_{\text{j,com}}$ is the computed angle using the identified coupling, where (a) shows θ_1, (b) shows θ_2, and (c) shows θ_3.

conducted with the finger starting from an extended state, closing and then opening again. As shown, the angles demonstrated hysteresis at lower joint angles, especially for θ_3 as shown in Fig. 8.10(c), this may be due to the stretching of the fabric. Despite the stretching, the joint angles exhibited good repeatability.

The kinematic relationship between the three joint angles were needed to allow for the control of the fingertip. The coupling between the joint angles is completely device and configuration dependent [137, 138]. Similar constraints were also applied to human test subject data [139]. To facilitate the identification of the kinematic relationship, the total angle ($\theta_1 + \theta_2 + \theta_3$) is utilized. The goal is to determine the contribution of each joint angle to the fingertip position. The total angle represents the angle of the fingertip. Therefore, θ_{total} will be used to determined the kinematic coupling between the joint angles. The joint angles and θ_{total} are shown in Fig. 8.10, demonstrating the repeatability as the same motion was conducted three times. A data-driven optimization that utilized `fmincon` was used to determine the couplings. Specifically, these kinematic couplings are given by

$$\begin{aligned} \theta_1 &= 0.6443\theta_{\text{total}} - 0.4175 \\ \theta_2 &= -0.0152\theta_{\text{total}} + 0.1982 \\ \theta_3 &= 0.3709\theta_{\text{total}} + 0.2193, \end{aligned} \tag{8.23}$$

where θ_j are in radians. It can also be shown that $\theta_3 = \theta_{\text{total}} - (\theta_1 + \theta_2)$. As it can be seen, these are first order relations that have a bias term. The bias term improved the correlation between the joint angles due to highly nonlinear behavior of the joint angle data. The validation of the identified kinematic relations are shown in Fig. 8.11. The measured and the computed joint angles demonstrated good agreement. The velocity coupling were derived by taking the time derivatives of Eq. (8.23) and can be expressed as

$$\begin{aligned} \dot{\theta}_1 &= 0.6443\dot{\theta}_{\text{total}} \\ \dot{\theta}_2 &= -0.0152\dot{\theta}_{\text{total}} \\ \dot{\theta}_3 &= 0.3709\dot{\theta}_{\text{total}}. \end{aligned} \tag{8.24}$$

8.3.2 Dynamics

Once all the sensor information was collected, it was processed before undertaking the optimization framework to identify the parameters. Specifically, $\boldsymbol{\theta}_j$, $\dot{\boldsymbol{\theta}}_j$, $\ddot{\boldsymbol{\theta}}_j$, $\dot{\boldsymbol{\theta}}_1\dot{\boldsymbol{\theta}}_2$, $\dot{\boldsymbol{\theta}}_1\dot{\boldsymbol{\theta}}_3$, $\dot{\boldsymbol{\theta}}_2\dot{\boldsymbol{\theta}}_3$, $\boldsymbol{\tau}_{\text{ext}}$ were computed, where $j \in (1,2,3)$. Using the data shown in Fig. 6.9, the values of these parameters were computed. The unknown variables to be identified are m_j, L_j, d_j, ϵ, η, ζ, f^j_{damp}, where $j \in (1,2,3)$. This means that there are 15 variables to be identified.

In this implementation, the error between the computed torque and the measured torque was selected as the objective function. The objective function takes a vector that has 15 elements. The nonlinear constraints on the expectation of $\boldsymbol{M}, \boldsymbol{C}, \boldsymbol{B}$ were included as well. For instance, $\boldsymbol{M}$ is symmetric and positive definite. `fmincon` returns the optimal values which is vector with 15 elements. It is noted that `fmincon` has to be run for each measured torque and joint values.

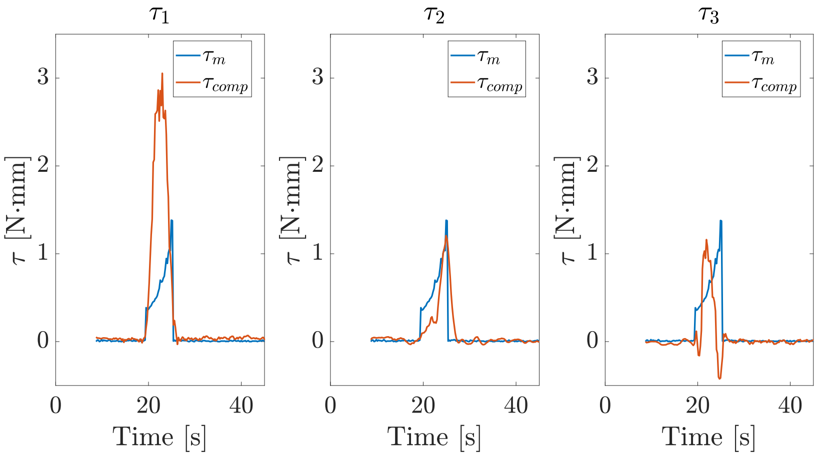

Figure 8.12: Identification of the parameters.

In Fig. 8.12, the comparison between the measured torque, τ_{m}, and the computed torque using the identified parameters, τ_{comp}, is shown during the identification phase. Since during the identification process, the error between τ_{comp} and τ_{m} is minimized, good agreement is expected. The higher error in τ_1, the torque at the MCP joint could be a result of the difficulty to converge due to higher torque at this joint. Existing studies have shown that there is a higher torque at the MCP joint [115, 140]

In Fig. 8.13, a different dataset was used to validate the performance using the identified parameters. As can be shown, the errors between τ_{comp} and τ_{m} is fairly low. While in τ_{m} demonstrated an almost even distribution through all the joints due to the minimal difference in the diameters of the phalanges, τ_{comp} demonstrated that the MCP joint had a higher concentration of the torque. Current works have demonstrated a similar finding [115, 140].

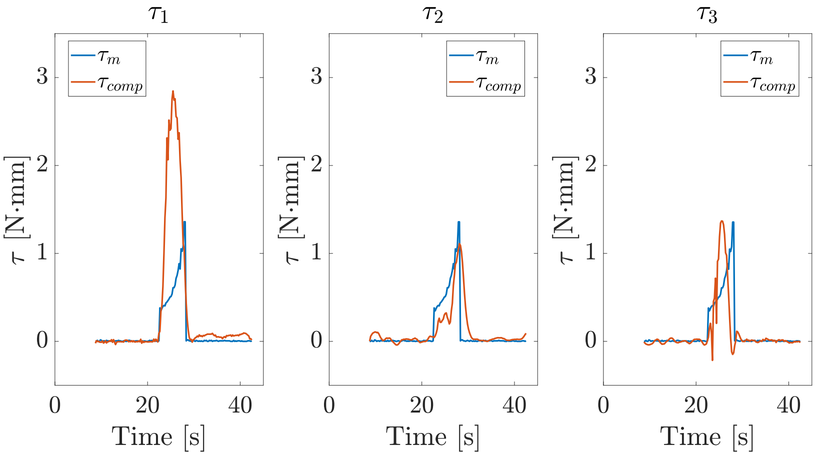

Figure 8.13: Validation of parameter identification.

CHAPTER 9

CONTROL OF AWARD

9.1 Introduction

In this section, the controllers that were used are introduced. The goal is to control the trajectory of the fingertips. As mentioned in Section 8.2.1, $\mathbf{p}$ represents the position of the fingertips. Then $\mathbf{p}_{\text{des}}$ returns $x_{\text{des}},\ y_{\text{des}},\ z_{\text{des}}$ of the desired position of the fingertips. $\mathbf{p}_{\text{des}}$ is attained by specifying the desired joint angles $\theta_{1,\text{d}},\ \theta_{2,\text{d}},\ \theta_{3,\text{d}}$. Since there is no direct independent control to all the angles, the target is knowing the location of the fingertip. Consequent to assuming that the finger motion is planar and that there is no out of plane motion, $z = 0$ for all motions. The world frame is coincident with frame one in Fig. 8.1(a). The controllers will be implemented in the joint space, then $\mathbf{p}$ would be computed by following the scheme outlined in 8.2.1. The remainder of the section details how the desired joint angles were computed, the method followed for trajectory generation and finally the different control schemes that were implemented.

9.1.1 Trajectory generation

The control inputs to the system are the tendon lengths, $\boldsymbol{q}$, and velocities, $\dot{\boldsymbol{q}}$. Ideally, the trajectories would be generated on $\boldsymbol{q},\ \dot{\boldsymbol{q}}$, with $\boldsymbol{\theta}_{\text{d}},\ \dot{\boldsymbol{\theta}}_{\text{d}}$ computed by inverting Eq. (8.2) and Eq. (8.3). However, this approach presents two challenges: First, inverting q_1 in Eq. (8.2) becomes intractable when the kinematic coupling in Eq. (8.23) are used. To demonstrate this, consider the example,

$$\cos(2\Phi + K) = \cos(K) - 2\sin^2(\Phi)\cos(K) - 2\sin(\Phi)\cos(\Phi)\sin(K), \tag{9.1}$$

where K is a constant, Φ is the angle. The relation becomes highly non-linear and it is difficult to solve for Φ. Second, computing $\dot{\boldsymbol{\theta}}_{\mathrm{d}}$ from $\dot{\boldsymbol{q}}_{\mathrm{d}}$ is also difficult since inverting Eq. (8.3) is not completely independent. Since $\boldsymbol{H}(\boldsymbol{\theta})$ depends on $\boldsymbol{\theta}$, this equation requires the knowledge of $\boldsymbol{\theta}$ even as $\boldsymbol{\theta}$ is being computed. To circumvent these two challenges, the trajectories will be generated on θ_{total}. Using θ_{total} for trajectories is reasonable since the position of the fingertip is the goal and has been used in literature [141, 142].

The choice of the desired trajectory was selected carefully. Specifically, two key considerations were: 1) the smoothness of the reference trajectory, which allows for safe interaction of AWARD with the user and 2) the ease in adjusting the desired range of motion. Previous studies [142] have achieved these requirements by minimizing the jerk. Polynomials are good potential options since they allow for the control of position, velocity and acceleration.

The trajectory of θ_{total} was generated using a third order polynomial, which allowed for the specification of position and velocities in the initial and final time is shown in Fig. 9.1. In particular,

$$\begin{aligned} \theta_{\mathrm{total}}(0) &= \theta_{\mathrm{total,0}}, \\ \theta_{\mathrm{total}}(t_f) &= \theta_{\mathrm{total,f}}, \\ \dot{\theta}_{\mathrm{total}}(0) = \dot{\theta}_{\mathrm{total}}(t_f) &= 0, \end{aligned} \tag{9.2}$$

where t_f is the final time, $\theta_{\mathrm{total,0}}$ is the initial total angle and $\theta_{\mathrm{total,f}}$ is the final total angle. Specifically, the third order polynomial was of the form

$$\theta_{\mathrm{total}}(t) = n_0 + n_1 t + n_2 t^2 + n_3 t^3, \tag{9.3}$$

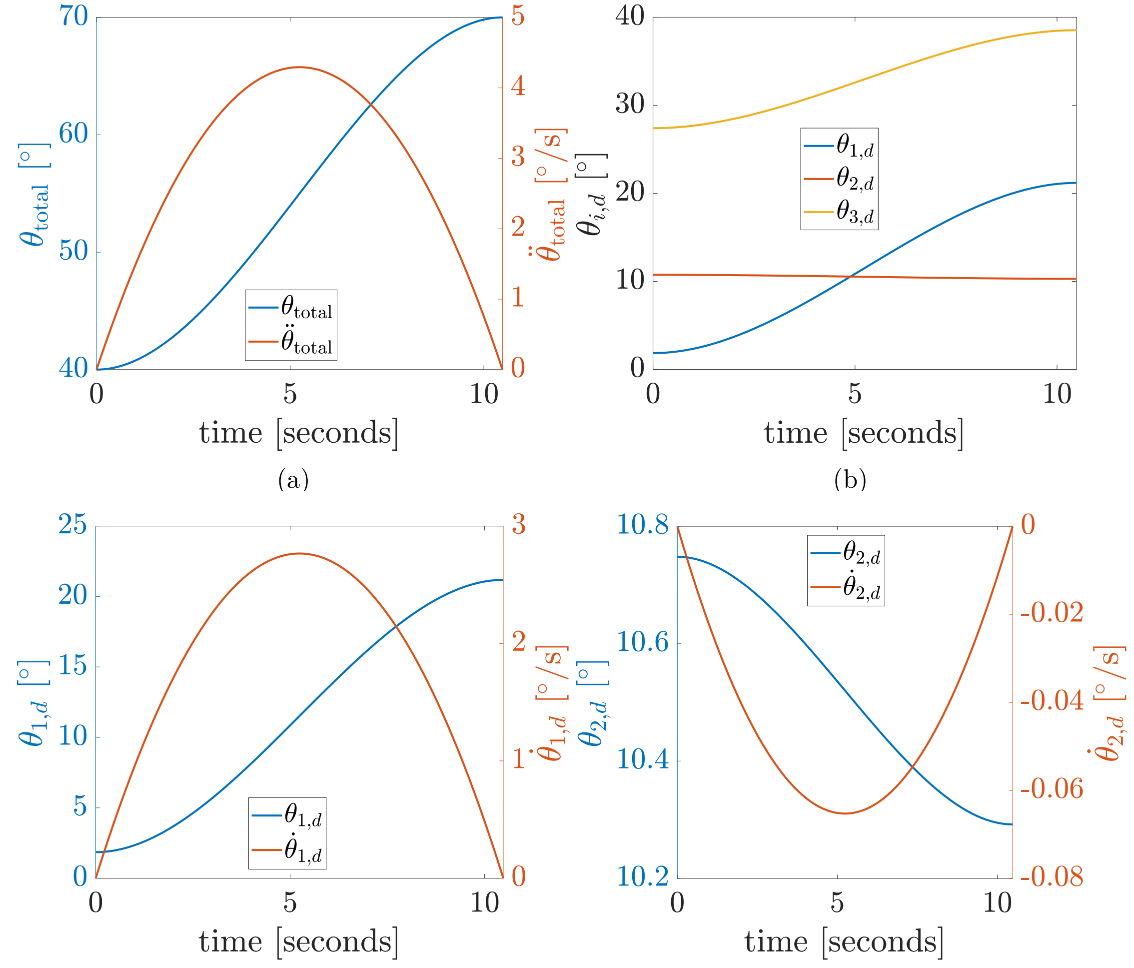

(a) (b)

(c) (d)

Figure 9.1: (a) Shows the desired total angle, θ_{total}, and velocity, $\dot{\theta}_{\text{total}}$, that was generated using a cubic polynomial. (b) Shows the desired joint angles, $\theta_{\text{j,d}}$. (c) Shows $\theta_{1,d}$ and $\dot{\theta}_{1,d}$. (d) Shows $\theta_{2,d}$ and $\dot{\theta}_{2,d}$.

where n_i are constant coefficients and t is time. Fig. 9.1(a) shows the position and velocity of the trajectory of θ_{total}. In Fig. 9.1(b), the position trajectories for the desired joint angles, $\theta_{\text{j,d}}$ are shown as computed using the coupling relations demonstrated in Eq. (8.23). In Fig. 9.1(c) and (d), the desired position and velocities for θ_1 and θ_2 are shown, which exhibit a similar behavior as θ_{total}. It is noted that θ_3 has not been shown but exhibits a similar behavior. The desired joint angles and velocities were computed using Eq. (8.23) and Eq. (8.24).

The knowledge of $\boldsymbol{\theta}_\mathrm{d}$ and $\dot{\boldsymbol{\theta}}_\mathrm{d}$ enabled the computation of the desired tendon contraction and contraction velocities. Specifically, the models in Eq. (8.2) and Eq. (8.3) were utilized to compute $\boldsymbol{q}_\mathrm{d}$, $\dot{\boldsymbol{q}}_\mathrm{d}$. The desired contraction and desired contraction velocity for the tendons are shown in Fig. 9.2. It is important to note that whilst Fig. 9.2(a) shows a clear symmetry — that is $q_{1,\mathrm{d}} = -q_{2,\mathrm{d}}$, in Fig. 9.2(b) there is a slight difference between $\dot{q}_{1,\mathrm{d}}$ and $\dot{q}_{2,\mathrm{d}}$. This may be a result of the parameters a_j, b_j being identified using the contraction of the tendons. If the true parameters were known, it is expected that the contraction velocities demonstrate the same behavior as the contraction. Once $\boldsymbol{q}$, $\dot{\boldsymbol{q}}$ are known, then the required motor rotations, $\boldsymbol{\Psi}_\mathrm{d}$, and motor rotational velocity, $\dot{\boldsymbol{\Psi}}_\mathrm{d}$, can be calculated. It is noted that any trajectories can be generated for control and not only the cubic polynomial that was used for this analysis. For example, in the software base, a fifth order polynomial and a sinusoidal trajectories were implemented. A pseudo code to determine the desired trajectories q_1 and q_2 is presented in Algorithm 9.2.

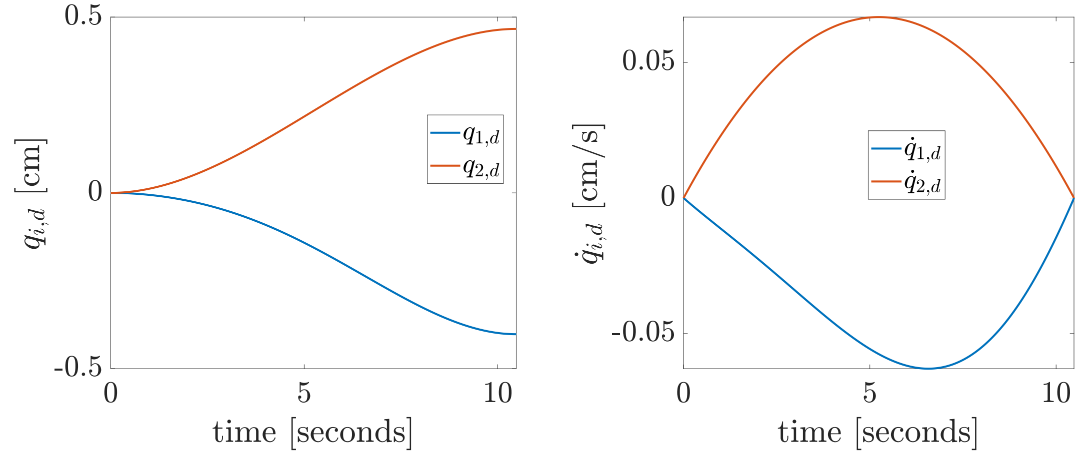

(a) (b)

Figure 9.2: (a) Shows the desired tendon contraction and (b) Shows the contraction velocities.

$\boldsymbol{\Psi}_\mathrm{d}$ is calculated by inverting Eq. (5.1) where $\Delta x = q$. $\dot{\boldsymbol{\Psi}}_\mathrm{d}$ is calculated by taking the

Algorithm 9.2 *Generating desired trajectories*

```
1. Define trajectory and constraints on $\theta_{\text{total}}$
2. Use kinematic relations (Eq. (8.23) and Eq. (8.24)) to compute $\boldsymbol{\theta}_{\text{d}},\ \dot{\boldsymbol{\theta}}_{\text{d}}$
3. Compute $\boldsymbol{q}_{\text{d}},\ \dot{\boldsymbol{q}}_{\text{d}}$ from (Eq. (8.2) and Eq. (8.3))
4. Compute $\boldsymbol{\Psi}_{\text{d}},\ \dot{\boldsymbol{\Psi}}_{\text{d}}$ by using the computed $\boldsymbol{q}_{\text{d}},\ \dot{\boldsymbol{q}}_{\text{d}}$
```

time derivative of the change of the TSA length with respect to the motor rotations. In particular, the TSA's linear velocity is given by [74]

$$\dot{q} = \frac{\Psi\dot{\Psi}r^2}{\sqrt{L_t^2 + \Psi^2 r^2}}. \tag{9.4}$$

Inverting Eq. (9.4) gives $\dot{\Psi}$. It is easy to show that the rotational speed is given by

$$\dot{\Psi} = \dot{q}\frac{\sqrt{L_t^2 + \Psi^2 r^2}}{\Psi r^2}. \tag{9.5}$$

Each DC motor that controls a TSA module has a quadrature encoder for angular velocity measurement, with which an angular velocity controller can be built. However, it is important to note that Eq. (9.5) has a singularity when $\Psi = 0$ and this case needs to be handled carefully. Otherwise, the rotational velocity will be maximum in this instance. This is not ideal — higher velocity will provide abrupt motion to the finger initially.

9.1.2 Controllers

The kinematic model (Eq. (8.2)) that is detailed in Chapter 8 enabled the control of AWARD in the motor encoder space and also in the tendon space. Two low-level controllers were implemented, namely trajectory tracking using PID in the 1) Encoder space and 2) Tendon space. These controllers are based on the error dynamics of position and velocities of the tendons to asymptotically drive the errors to zero in finite time. Both controllers will enable the fingertip to follow a predefined trajectory, which is essential for rehabilitation and resistive training.

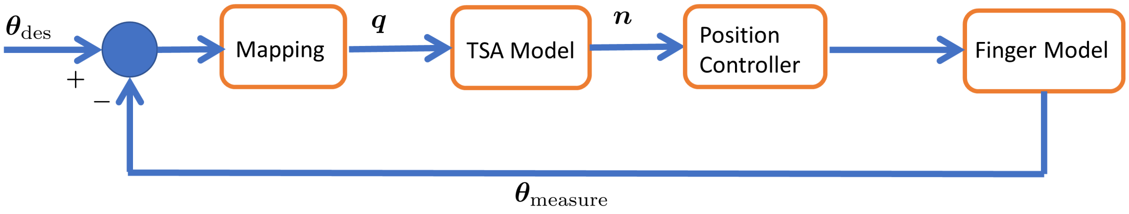

Figure 9.3: The position control architecture for AWARD. The mapping block converts $\boldsymbol{\theta}_{\text{des}}$ to the tendon lengths by using Eq. (8.2).

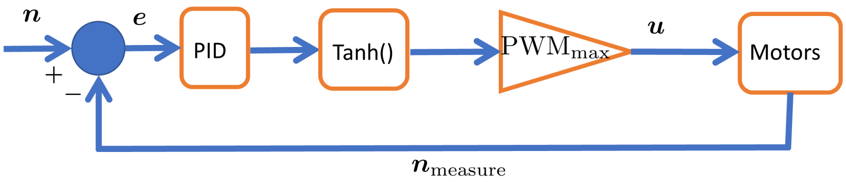

Figure 9.4: The position controller using encoder to measure motor rotations. The tanh() function is used for saturation.

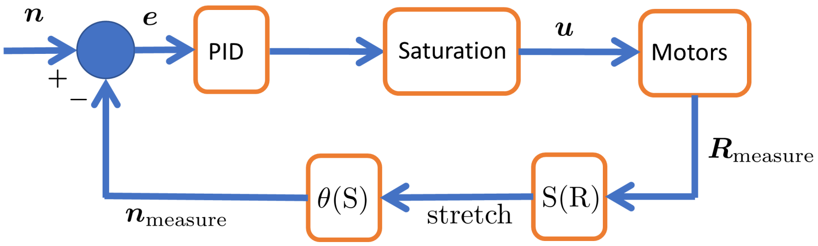

Figure 9.5: The position controller using the resistance measurement of the SCP strings. The saturation block checks for R_{max} and R_{min} and mapping to the active PWM of the motor. S(R) is the stretch as a function of resistance and θ(S) is the motor rotations as a function of stretch.

The controller framework is shown in Fig. 9.3. The mapping block is given by the kinematic coupling of the joint angles. The controller architecture is shown in Fig. 9.4.

The tanh() function takes values between $[-\infty, \infty]$ and outputs values between $[-1, 1]$ and allows for a translating of the input to the outputs with consistent sensitivity at small values. Since the control was implemented in the encoder space, the number of ticks can be quite large and tanh() proved key in the saturation of the computed control command.

When the SCPs were implemented, the controller architecture was then implemented as shown in Fig. 9.5. It is important to note that $\boldsymbol{\theta}_{\text{measure}}$ is obtained through the IMUs and the SCP resistance measurements. In particular, θ_1, θ_2 are acquired from IMUs and then θ_3 is computed using Eq. (8.2).

The control schemes were implemented in the encoder space since this is robust to the vibrations and stretching of the fabric. Due to the antagonistic driven TSA for each finger, there are three control approaches that can be used, namely:

1. *Single motor control* — In this control scheme, the error dynamics of one motor are used to compute the control input. The control input is used for both motors.
2. *Coupled motor control* — In this control approach, the maximum error of the two motors is used to calculate the control input which is then used for both motors.
3. *Independent motor control* — In this control implementation, error dynamics of each motor are used to compute the control input for that particular motor.

It is noted that in all the schemes the control gains are kept the same. Specifically, the gains for the controller were $K_p = 0.03$, $K_i = K_d = 0.01$, selected to minimize errors and track the reference signal as closely as possible.

The above described control schemes are open loop in relation to the measured angles. The desired trajectory was generated by using measured $\theta_{\text{total},0}$ for the initial position with the final position attained by specifying the desired change of θ_{total}. Specifically,

$$\begin{aligned} \theta_{\text{total},0} &= \theta_{1,0} + \theta_{2,0} + \theta_{3,0}, \\ \theta_{\text{total,f}} &= \theta_{\text{total},0} + \Delta\theta_{\text{total}}, \end{aligned} \tag{9.6}$$

where $\theta_{j,0}$ are the initial measurements from the IMUs and $\Delta\theta_{\text{total}}$ is the desired change in the total joint angle. The maximum limit on θ_{total} was checked before the coefficients for the desired trajectory were computed. The desired motor rotations and motor rotational speeds are then computed based on the desired joint angles, using the steps outlined in Section 9.1.1. It is important to note that in this implementation, there is no feedback on the measured joint angles during actuation. This approach accords a lot of trust on the kinematics of the device. In addition, this approach is computationally cheaper — the error dynamics of each TSA module only depend on that TSA module since the motors exhibit bidirectional rotation. A bigger error was decreased by changing direction while a small error was increased by continuing current rotation. While we have demonstrated the repeatability of the devices over multiple cycles, this approach was not robust. In the next section, the joint angles are incorporated in the control.

When the closed-loop control is implemented in the tendon space, the implementations requires careful considerations. Let the error dynamics be defined as

$$\begin{aligned} e_1 &= q_1 - q_{1,\text{d}},\ e_2 = q_2 - q_{2,\text{d}}, \\ \dot{e}_1 &= \dot{q}_1 - \dot{q}_{1,\text{d}},\ \dot{e}_2 = \dot{q}_2 - \dot{q}_{2,\text{d}}, \end{aligned} \tag{9.7}$$

where $q_1,\ q_2$ depend on the measured joint angles as defined in Eq. (8.2). In the ideal case, $e_1 = e_2$ — the deviation of the first tendon from the desired length is equivalent to the deviation of the second tendon from the desired length. This is especially key due to the assumption that the contraction of both tendons are the same. This is the assumption that was utilized when identifying the geometric parameters of the threading. Further, for this case, the control scheme is computationally expensive compared to controlling in the encoder space. In particular, it is important to note that to modify e_1, for example, both TSA modules are needed for actuation. In the case when $e_1 \neq e_2$, $\bar{e}$ is then used, where $\bar{e} = \max\{e_1, e_2\}$. The gains are then tuned carefully to reduce any sinusoidal behavior.

The steps to compute the control input is then outlined in the following steps:

1. Initialize sensors and calculate desired joint angles.
2. Compute $\boldsymbol{q}_{\mathrm{d}},\ \dot{\boldsymbol{q}}_{\mathrm{d}},\ \boldsymbol{q},\ \dot{\boldsymbol{q}}$.
3. Compute $\boldsymbol{e}$, and $\dot{\boldsymbol{e}}$.
4. Compute $\boldsymbol{\Psi}$ and $\dot{\boldsymbol{\Psi}}$ using the TSA model with the result from the step above.
5. Use PID to calculate control input and then pass through saturation before control TSA module PWM.

9.2 Experiments

The characterization of the controllers is presented in two subsections: encoder space control and tendon space control.

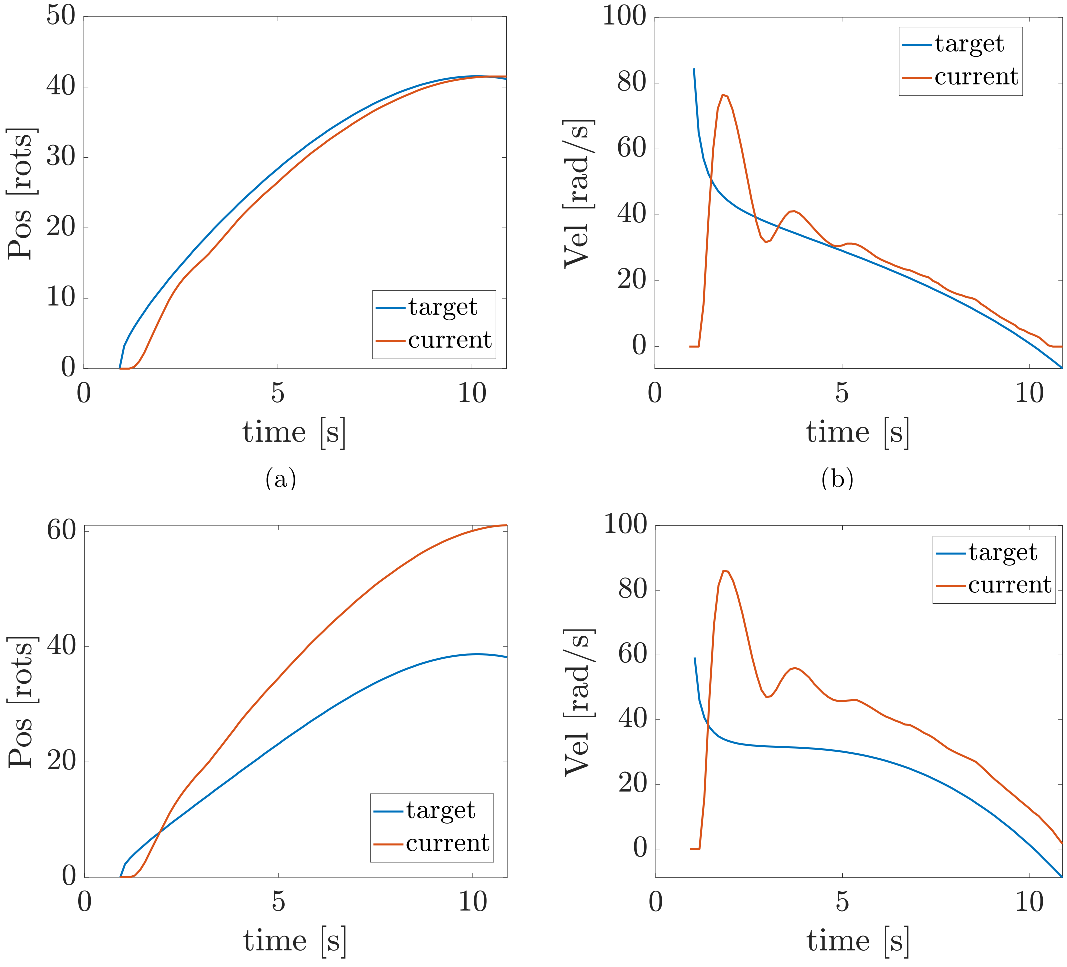

(a) (b) (c) (d)

Figure 9.6: Controller performance to track a trajectory using scheme 1 where the error dynamics for motor connected to q_2 are implemented. (a) Shows the position tracking for motor connected to q_2, (b) Shows the position error, in rotations, for motor connected to q_2, (c) Shows the velocity tracking for motor connected to q_2, (d) Shows the velocity errors for motor connected to q_2, (e) Shows the position tracking for motor connected to q_1, and (d) Shows the velocity tracking for motor connected to q_1. The gains for the controller were $K_p = 0.03,\ K_i = K_d = 0.01$.

9.2.1 Encoder space control

The three PID control schemes were conducted in experiments.

(a) *Single motor control* — The performance of the scheme is shown in Fig. 9.6. It is clear that while the motor connected to q_2 performed well with tracking for both position (Fig. 9.6(a)) and velocity (Fig. 9.6(c)), with the errors approaching zero (Fig. 9.6(b) and (d)), the performance of the motor connected to q_1 performed worse in position tracking (Fig. 9.6(e)) and velocity tracking (Fig. 9.6(f)). Since the motors are rotating in opposite directions, the absolute values are used. Specifically, the motor connected to q_1 had negative rotations. The deviation of the motor connected to q_1 was not ideal. If the motors were not in good synchronization, the net force output at the fingertips will be reduced. Therefore a different control scheme was tested. Especially important to note is that the target velocities do not start from zero, but high values. This was due to the singularity in Eq. (9.5) when there were zero motor rotations. Software implemented accounted for the singularity.

(b) *Coupled motor control* — In Fig. 9.7 and Fig. 9.8, the control performance of the scheme is shown. As it can be demonstrated, both the motors exhibited sinusoidal behaviors. Specifically, as seen in Fig. 9.7(b) and Fig. 9.8(b), the sinosiods had much bigger amplitudes. These sinusoidal behaviors were not ideal for AWARD.

(c) *Independent motor control* — The control performance of this implementation is shown in Fig. 9.9 and Fig. 9.10. In this control scheme, both motors demonstrated good tracking for position and velocity. As seen in Fig. 9.10(b), the velocity for the motor connected to q_2 showed some minor sinusoidal behavior towards the end of the motion. This phenomenon may be improved by further tuning the controller gains.

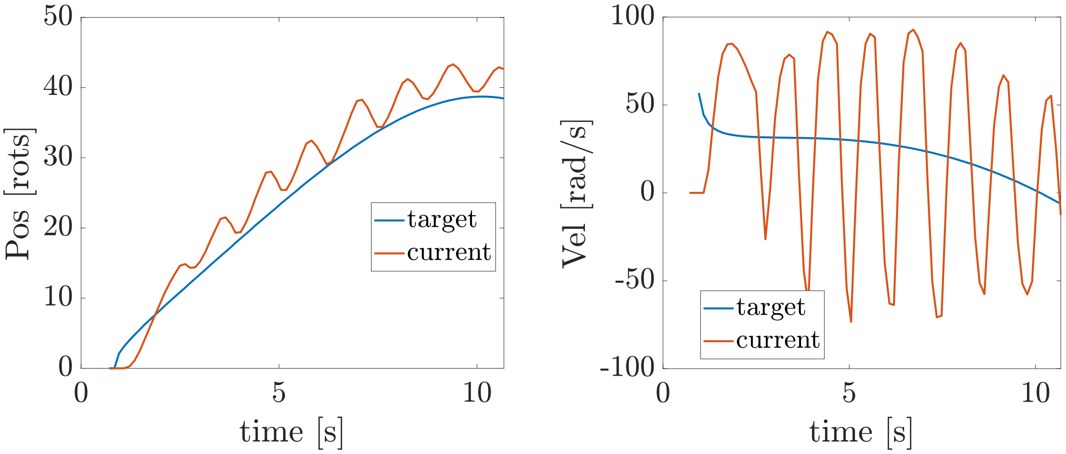

(a) (b)

Figure 9.7: Shows the performance of Scheme 2 controller, (a) Shows the position tracking of the motor connected to q_1, and (b) Shows the velocity tracking for for the motor connected to q_1.

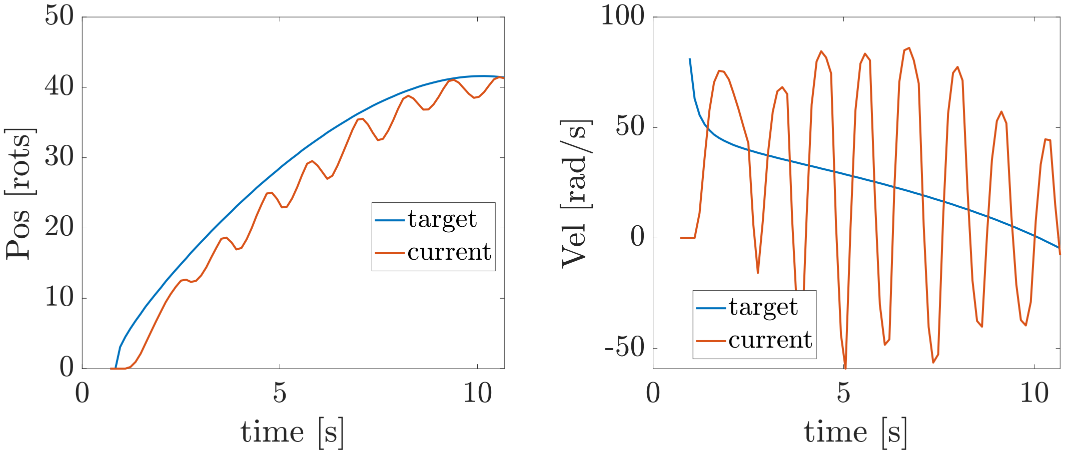

(a) (b)

Figure 9.8: Shows the performance of Scheme 2 controller, (a) Shows the position tracking for motor connected to q_2, and (b) Shows the velocity tracking for motor connected to q_2.

9.2.2 Tendon space control

The performance of this control implementation is shown. In Fig. 9.11, the performance was demonstrated when the controller gains were tuned. Specifically, the gains

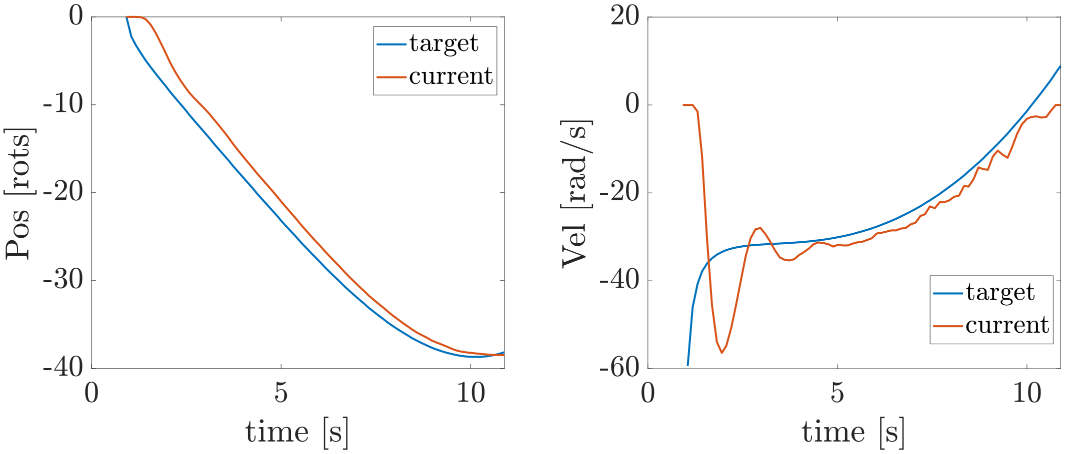

(a) (b)

Figure 9.9: Shows the performance of Scheme 3 controller, (a) Shows the position tracking for motor connected to q_1, and (b) Shows the velocity tracking for motor connected to q_1.

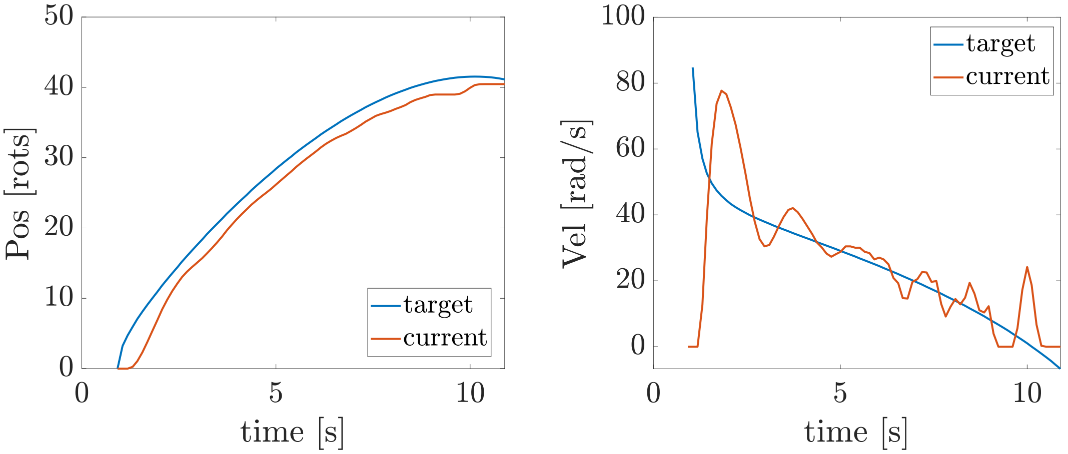

(a) (b)

Figure 9.10: Shows the performance of Scheme 3 controller, (a) Shows the position tracking for motor connected to q_2, and (b) Shows the velocity tracking for motor connected to q_2.

were $K_p = 0.015,\ K_d = 0.01,\ K_i = 0.0$. Controller gains were tuned to minimize high frequency oscillations while tracking the reference signal closely. Fig. 9.11(a)–(d) shows the joints angles, θ_1, θ_2, θ_3 and θ_{total} respectively. In Fig. 9.11(e), the controller performance on q_1 is shown in Fig. 9.11(f), the controller performance on q_2 is shown.

θ_{measure} was used to compute the current contraction for $\boldsymbol{q}$. In this implementation, the errors for the contraction were quite large for both tendons. However, the desired change of total angle was 30° and as can be shown in Fig. 9.11(d), the target change was still reached.

In Fig. 9.12, a different trial was executed when the gains were $K_p = 0.03,\ K_d = 0.01,\ K_i = 0.0$. Fig. 9.12(a)–(d) shows the joints angles, θ_1, θ_2, θ_3 and θ_{total} respectively. Fig. 9.12(e) shows the controller performance on q_1 and Fig. 9.12(f) shows the control performance on q_2. In this realization, the error dynamics on q_1 were used to compute the control input. This is evident due to the smaller errors in q_1 as shown in Fig. 9.12(e). In this trial, the desired angle change for the total angle was 30°. As demonstrated in Fig. 9.12(d), this change was achieved.

9.3 Discussion

The trajectory tracking control schemes implemented exhibited different advantages and performances. Control in the encoder space demonstrated low tracking errors that were not prone to vibrations even as the fabric was stretching. While this behavior is advantageous, the limitation is that there was no feedback to the measured joint angles. This approach allocates a lot of trusts in the kinematics of the devices — that is the same number of rotations will always lead to the same motion or change in motion. However since this model was identified through data-driven optimization, it is possible that this is not the case, hence incorrect motions can be achieved.

Controlling in the tendon space was advantageous due to the feedback from the joint angles. However, the limitation is that joint angles could be noisy due to the stretching of the fabric and the vibrations that may be caused by the wire connections.

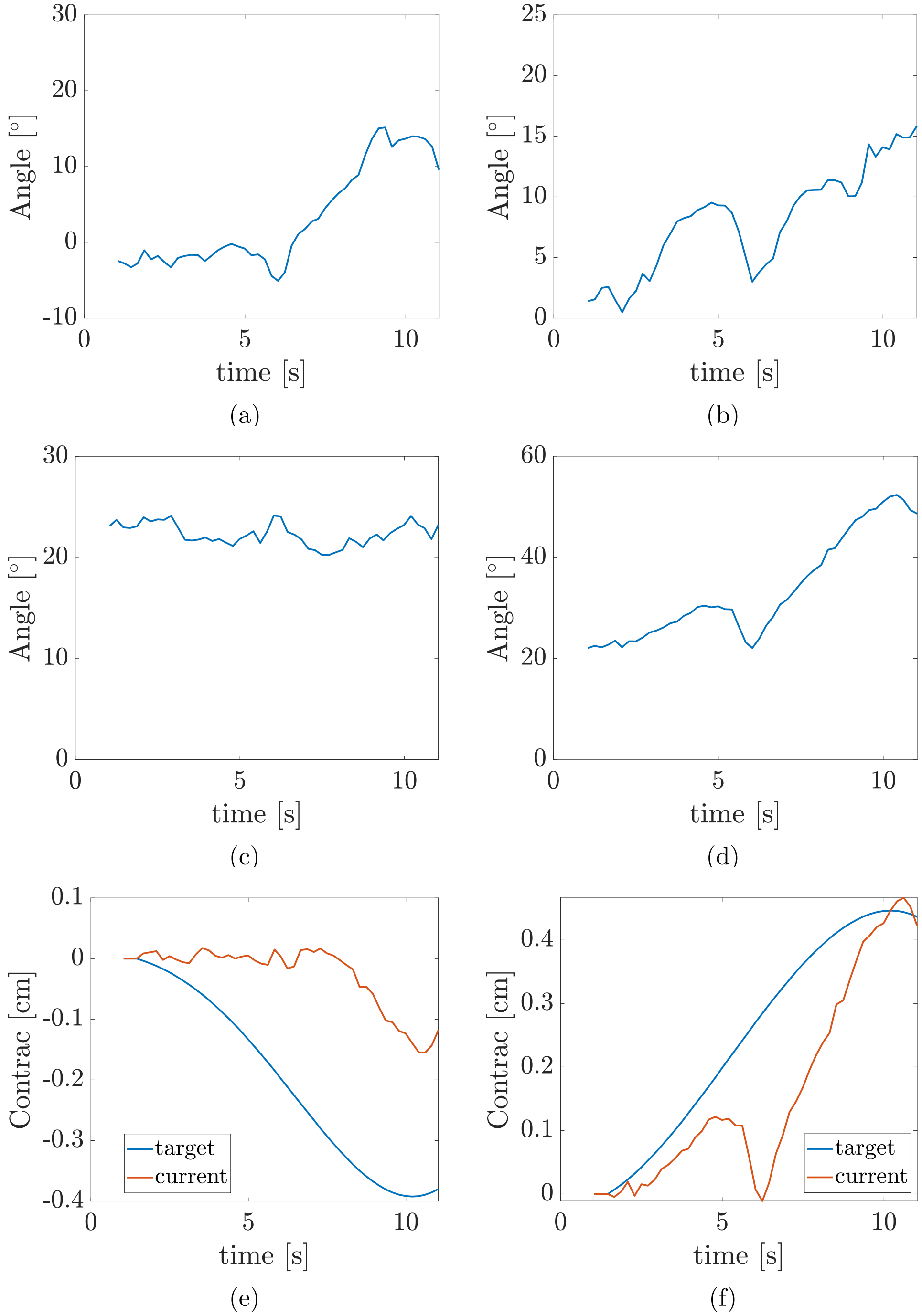

(a) (b) (c) (d) (e) (f)

Figure 9.11: The tendon space controller performance to track a trajectory. (a) Shows the measured θ_1, (b) Shows θ_2, (c) Shows the measurements for θ_3, (d) Shows θ_{total}, (e) Shows the target and measured contraction for q_1, and (f) Shows the desired and measured contraction for q_2.

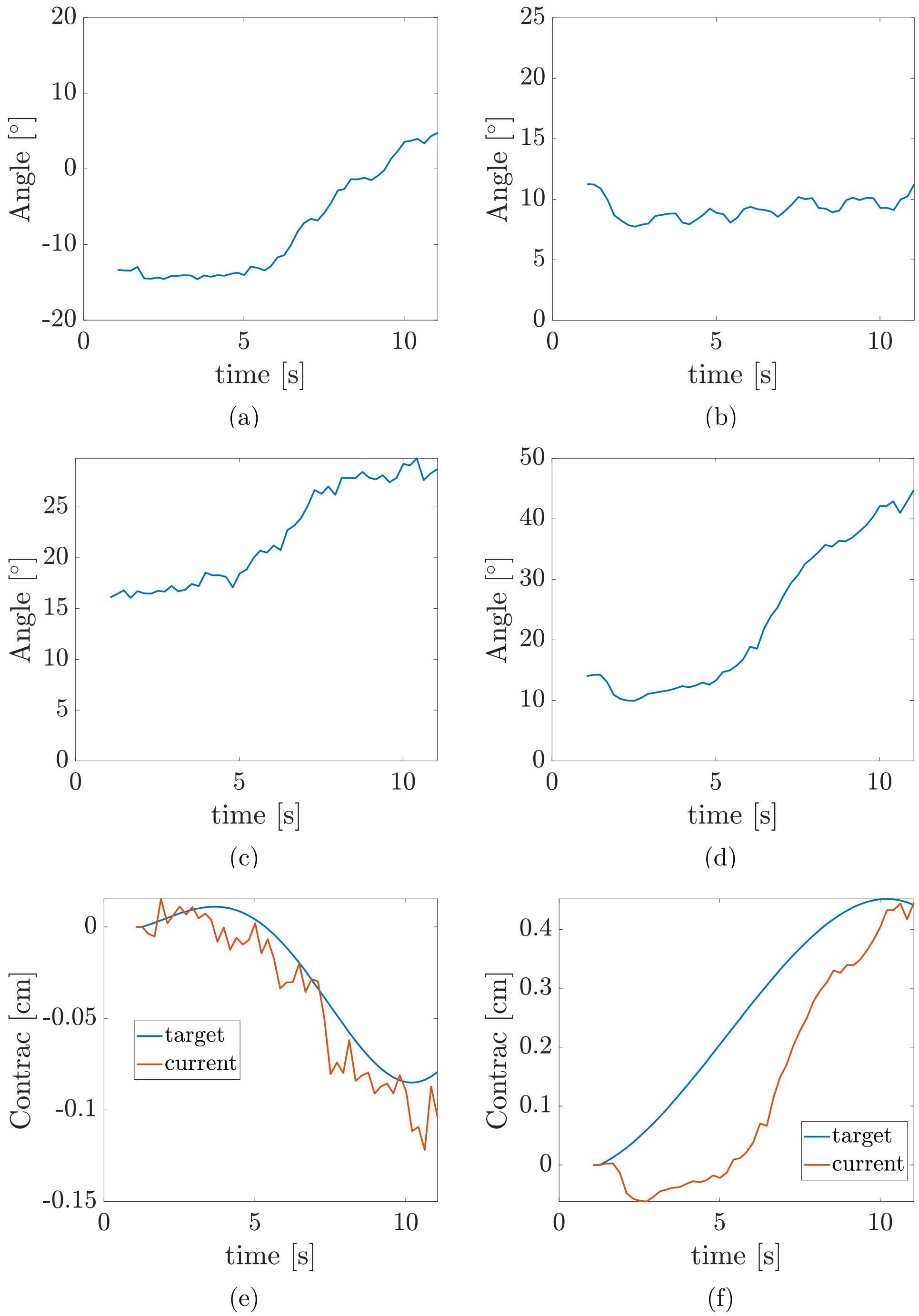

(a) (b) (c) (d) (e) (f)

Figure 9.12: The tendon space controller performance to track a trajectory. (a) Shows the measured θ_1, (b) Shows θ_2, (c) Shows the measurements for θ_3, (d) Shows θ_{total}, (e) Shows the target and measured contraction for q_1, and (f) Shows the desired and measured contraction for q_2.

Some sources of error in the experimental data include the vibration of the IMUs during actuation. This was caused by the fabric stretching as the finger was actuated. In addition, the stiffness of the connecting wires used on the sensor may have also exacerbated errors. The connecting wires of the IMUs were 32 American Wire Gauge (AWG) while the connecting wires for the FSRs were 28 AWG. During actuation, the stiffness of these wires alter the orientations of the IMUs, leading to inclination change that is not a result of the change of finger angles.

Another consideration in conducting the experiments is the encoder being used. Specifically, a relative encoder was used in the TSAs. This means that when the microcontroller resets, the encoder resets to zero. But to be able to control the TSA from any position, the number of rotations to attain that state was needed. Since the goal was to keep the cost of AWARD low, absolute encoders were not used because they are generally more expensive than relative encoders. To circumvent this limitation, software implementation was utilized. In one approach, a full cycle of the either extension then flexion or flexion then extension was always performed. In this way, the position of the motors before microcontroller resets is not needed. In another approach, the EEPROM is used to constantly store the current motor rotations and when the microcontroller resets, the last values are available for retrieval at the beginning of the new run. The Teensy®4.1 has 4 kilobytes of emulated EEPROM.

9.4 Conclusion and Future Work

In this chapter, analysis was performed that allowed for the control of AWARD to follow predefined trajectories that may be suitable for rehabilitation or activities of daily living. Specifically, the kinematics model that allowed for the analytical computation of the effect of tendon lengths to the joint angles were presented. Parameters that were difficult to measure were then identified using a data-driven optimization approach. Further, a systematic approach is presented that allowed for the generation of trajectories that can be followed by the device, enabling control. Two control approaches were then implemented both in the encoder space and also in the tendon space, highlighting the performance and computational differences. The results of the controllers demonstrated reasonably good performance and proved that these controls schemes can be used. Future work will include improvements in the force sensing at the fingertips to allow for force control.

Part IV

Conclusions

CHAPTER 10

CONCLUSION AND FUTURE WORK

This dissertation has described and analyzed a method for comparing the performance metrics of two predominantly used motor-based actuation approaches in wearable devices — TSAs and SMTAs. This method was then utilized to design five devices – two versions of BRAG, two versions of AWARD and a wrist orthosis. All five devices are characterized, tested and open-loop controlled while AWARD is modeled and close-loop control performed. The kinematic and dynamic models were presented. In this chapter, a summary of the main results and contributions are presented and suggestions for areas of future work are provided.

10.1 Conclusion

10.1.1 Choice of actuation mechanisms

Chapter 2 introduced the type of actuation mechanisms predominantly used for wearable robotic devices. An emphasis on the motor-based actuation mechanisms were introduced, providing detailed background information on twisted string actuators. The different configuration of TSAs were discussed. In Chapter 3, a model-based framework that allowed for the analysis of key performance metrics of TSAs was discussed. The performances of TSAs were compared with SMTAs in terms of linear contraction, linear speed, force output, and effective torque input. The performance comparisons were conducted in simulations and experiments, using TSAs and SMTAs constructed from the same type of motors. The results indicated that TSAs performed better in terms of force output and effective torque input, whereas SMTAs performed better in terms of contraction range and speed.

10.1.2 Design of wearable devices

Chapter 4 presented a new compact, high performance, soft glove that was powered with TSAs. TSA-BRAG system eliminated the rigid railing required for the non-rotating ends. Experiments were presented to validate TSA-BRAG's assistive capabilities for ADL, like grasping everyday objects. The choice of actuators for the performance of TSA-BRAG were informed by the comparison study performed in Chapter 3. Furthermore, the second version of TSA-BRAG incorporated SCP strings for motion tracking and as a passive spring to extend fingers after actuation. Experiments were performed to demonstrate the capability of picking everyday objects and highlighted the resistance variation during the picking process.

Chapter 5 then covered the design and characterization of AWARD, detailing the design decisions and analysis of the sub-components of the device. Key features of AWARD were the ability to operate both in assistive mode and resistive mode while being compact, soft and lightweight. Using TSAs that have strings of different materials improved the properties of TSAs, including compliance and the ability to act as a sensing modality. Chapter 6 then outline the improvements from AWARD described in the previous chapter, particularly focusing on the sensing systems that allowed for the closed-loop control described in Chapter 9. The choice and calibration of the sensing is described in detail.

In Chapter 7 the *first* wearable orthosis device that actuated all three DOF of the wrist using TSAs was presented. The versatility of TSAs allowed for the use of TSAs that used two types of strings — FE and PS used stiff fishing lines, while AA utilized the compliant SCP strings. The range of motion of the orthosis was sufficient to perform necessary ADLs. Further, it was shown that the device can actuate while donned by human test subject.

10.1.3 Modeling and closed-loop control of AWARD

In Chapter 8, the kinematic and dynamic model of a finger was presented, and demonstrated that key parameters can be estimated using data-driven approaches. Chapter 9 presented the control of AWARD. In addition, an in-depth analysis on the trajectory was presented with consideration of the under-actuated nature of AWARD. Further, trajectory control strategies in the tendon space and encoder space were realized allowing AWARD to achieve the unique capabilities of active resistance and active assistance.

10.2 Review of Contributions

This dissertation has presented the following contributions:

- A synthesis of existing models of TSAs to succintly demonstrate a closed-form performance analysis of TSAs. Moreover, a theoretical framework for comparing key performance metrics of TSAs and SMTAs was developed with the metrics validated in simulation and experiments. The approach and results were presented in Chapter 3.
- A utilization of TSAs to drive soft wearabe devices. By using TSAs, the designed wearable devices were compact, high-performance and actuated multi-

DOF. We presented the design, characterization and validation of these devices that included two versions of an assistive and rehabilitation glove (BRAG v1 and BRAG v2), a wearable gloves combining both assistive and resistive capabilities (AWARD) and a wearable wrist orthosis. These devices and their performance results were described in Chapters 4, 5, 6 and 7.

- A derivation of the kinematic and dynamic model of AWARD. In addition, the models were then used to implement a closed-loop control scheme of AWARD. The feedback signals were carefully selected, ensuring compactness of the devices and further not hugely sacrificing the intergrity of the signals. Chapters 8 and 9 presented the approaches and the results.

10.3 Future Work

Though the work discussed in this dissertation results in lightweight, high performance wearable robotics devices, the future work that can further advance this work is described below.

10.3.1 Performance Analysis of TSA

Despite developing a model-based framework that doesn't depend on motor properties, a better model may still be developed. Future work will include more accurate modeling that considers the finite stiffness of the strings and more types of motors and strings. Additionally, the performance of SMTAs and TSAs will be compared in practical application where the performance of a robotic device driven by an SMTA and a TSA using the same type of motor will be compared. In addition, SMTA with increasing spool radius due to rotations will be investigated. When thicker strings are used, the effective radius of the spool will increase with increasing rotations as the strings stacking on each other would change the diameter.

10.3.2 Closed-loop control of Wrist Orthosis

The wrist orthosis presented was the first to actuate all the three degrees of freedom (flexion/extension, pronation/supination and adduction/abduction). While the device demonstrated the promise of using TSAs with different properties, the wrist orthosis was open-loop controlled. In the future, closed-loop control utilizing the conductive SCP strings and installing extra inertial measurement units would allow for more sensing capabilities and allowing for feedback control. The device can be analyzed using its similarities to the Stewart platform.

10.3.3 Intention detection schemes for devices

The devices that have been developed have not focused on the type of input that the user provides. But with devices demonstrating good performance in terms of range of motions, force outputs and control, it would be important to implement novel methods to acquire user intentions for usage. Predominantly used methods include voice activation, button activation or using EMG signals. However EMG signals can be limited since EMG signals depend on the orientation of the user limp, sweating or external temperature conditions.

10.3.4 Extensive Human Studies

While the devices that have been presented demonstrate that they both actuated and provided sufficient force output for activities of daily living and rehabilitation, it would be more compelling to perform extended studies with patients that have disabilities or need rehabilitation. For instance, a collaboration with either the Biomedical Engineering department or Medical school would be beneficial for recruiting patients for these studies. Metrics such as comfort, effectiveness of the devices and force output can be evaluated in real life situations.

APPENDIX A

FINGER DYNAMICS DERIVATION

To derive the dynamics of AWARD, the model for each finger motion was analyzed separately. Then the fingers were considered as independent rigid bodies, allowing for the derivation of the full device dynamics. In addition, planar motion was assumed for the MCP joint. The dynamic model of each finger is given by

$$\boldsymbol{M}(\boldsymbol{\theta})\begin{bmatrix}\ddot{\theta}_1\\ \ddot{\theta}_2\\ \ddot{\theta}_3\end{bmatrix}+\boldsymbol{C}(\boldsymbol{\theta})\begin{bmatrix}\dot{\theta}_1^2\\ \dot{\theta}_2^2\\ \dot{\theta}_3^2\end{bmatrix}+\boldsymbol{B}(\boldsymbol{\theta})\begin{bmatrix}\dot{\theta}_1\dot{\theta}_2\\ \dot{\theta}_1\dot{\theta}_3\\ \dot{\theta}_2\dot{\theta}_3\end{bmatrix}+\boldsymbol{G}(\boldsymbol{\theta})+\boldsymbol{\tau}_f=\boldsymbol{\tau}_{\text{ext}}, \tag{A.1}$$

where $\boldsymbol{M}(\boldsymbol{\theta}) \in \mathbb{R}^{3\times3}$ is the inertia matrix, $\boldsymbol{C}(\boldsymbol{\theta}) \in \mathbb{R}^{3\times3}$ is the centrifugal, $\boldsymbol{B}(\boldsymbol{\theta}) \in \mathbb{R}^{3\times3}$ is the Coriolis matrix, $\boldsymbol{G}(\boldsymbol{\theta}) \in \mathbb{R}^{3\times1}$ is the gravity vector, $\boldsymbol{\tau}_f \in \mathbb{R}^{3\times1}$ is the torques that relates to the tendon friction and flexibility and $\boldsymbol{\tau}_{\text{ext}} \in \mathbb{R}^{3\times1}$ is the total required input joint torque.

$\boldsymbol{M}(\boldsymbol{\theta})$, $\boldsymbol{C}(\boldsymbol{\theta})$, $\boldsymbol{B}(\boldsymbol{\theta})$ and $\boldsymbol{G}(\boldsymbol{\theta})$ can be derived by using the Lagrange-Euler approach. The parameters used in these derivations are shown in Fig. 8.1(b). The Lagrangian is given by $\mathcal{L} = K - P$, where K is the kinetic energy and P is the potential energy of the system. Then the equations of motions can be derived from

$$\frac{d}{dt}\frac{\delta\mathcal{L}}{\partial\dot{\theta}_j}-\frac{\partial\mathcal{L}}{\partial\theta_j}=\tau_j. \tag{A.2}$$

The kinetic energy, K, is given by

$$K=\frac{1}{2}m_j v_j^\top v_j+\frac{1}{2}\omega_j^\top I_j\omega_j, \tag{A.3}$$

where $v_j = J_{v_j}(\theta)\dot{\theta}$, $\omega_j = J_{\omega_j}(\theta)\dot{\theta}$ and the moment inertia is given by

$$I_j=\frac{1}{4}m_j\left(\frac{d_j}{2}\right)^2+\frac{1}{3}m_jL_j^2, \tag{A.4}$$

Specifically, the potential energy is given by

$$\begin{aligned} P = m_1 g l_1 \sin(\theta_1) + m_2 g(L_1 \sin(\theta_1) + l_2 \sin(\theta_1+\theta_2)) \\ + m_3 g(L_1 \sin(\theta_1) + L_2 \sin(\theta_1+\theta_2) + l_3 \sin(\theta_1+\theta_2+\theta_3)). \end{aligned} \tag{A.5}$$

Then $\boldsymbol{G}(\boldsymbol{\theta}) = [g_1\ g_2\ g_3]^\top$, where $g_1,\ g_2,\ g_3$ is given by

$$\begin{cases} g_1 = (m_1 l_1 + L_1(m_2+m_3))g\cos(\theta_1) + (m_2 l_2 \\ + m_3 L_3)g\cos(\theta_1+\theta_2) + m_3 g l_3 \cos(\theta_1+\theta_2+\theta_3), \\ g_2 = (m_2 l_2 + m_3 L_3)g\cos(\theta_1+\theta_2) + m_3 g l_3 \cos(\theta_1+\theta_2+\theta_3), \\ g_3 = m_3 g l_3 \cos(\theta_1+\theta_2+\theta_3). \end{cases} \tag{A.6}$$

$\boldsymbol{M}(\boldsymbol{\theta})$ is defined as

$$\boldsymbol{M}(\boldsymbol{\theta}) = \begin{bmatrix} M_{11} & M_{12} & M_{13} \\ M_{21} & M_{22} & M_{23} \\ M_{31} & M_{32} & M_{33} \end{bmatrix}, \tag{A.7}$$

where the elements of $\boldsymbol{M}(\boldsymbol{\theta})$ are described in this way:

$$\begin{cases} M_{11} = m_1 l_1^2 + m_2(L_1^2 + l_2^2 + 2L_1 l_2 \cos(\theta_2)) + m_3(L_1^2 + L_2^2 \\ + l_3^2 + 2L_1 L_2 \cos(\theta_2) + 2L_2 l_3 \cos(\theta_3) + l_3 \cos(\theta_2+\theta_3)) \\ + I_1 + I_2 + I_3, \\ M_{12} = m_2(l_2^2 + L_1 l_2 \cos(\theta_2)) + m_3(L_2^2 + l_3^2 + 2L_2 l_3 \cos(\theta_3) \\ + L_1 L_2 \cos(\theta_2) + L_1 l_3 \cos(\theta_2+\theta_3)) + I_2 + I_3, \\ M_{13} = m_3(l_3^2 + L_1 l_3 \cos(\theta_2+\theta_3)) + L_2 l_3 \cos(\theta_3) + I_3, \\ M_{22} = m_3(L_2^2 l_3^2 + 2L_2 l_3 \cos(\theta_3)) + m_2 l_2^2 + I_2 + I_3, \\ M_{23} = m_3(l_3^2 + L_2 l_3 \cos(\theta_3)) + I_3, \\ M_{33} = m_3 l_3^2 + I_3,\ M_{21} = M_{12},\ M_{31} = M_{13},\ M_{32} = M_{23}. \end{cases} \tag{A.8}$$

where the moment inertia is given by

$$I_j = \frac{1}{4}m_j\left(\frac{d_j}{2}\right)^2 + \frac{1}{3}m_jL_j^2, \tag{A.9}$$

for $j \in (1, 2, 3)$. The matrices $\boldsymbol{C}(\boldsymbol{\theta})$ and $\boldsymbol{B}(\boldsymbol{\theta})$ is given by

$$\boldsymbol{C}(\boldsymbol{\theta}) = \begin{bmatrix} b_{111} & b_{122} & b_{133} \\ b_{211} & b_{222} & b_{233} \\ b_{311} & b_{322} & b_{333} \end{bmatrix}, \ \boldsymbol{B}(\boldsymbol{\theta}) = 2\begin{bmatrix} b_{112} & b_{113} & b_{123} \\ b_{212} & b_{213} & b_{223} \\ b_{312} & b_{323} & b_{323} \end{bmatrix}, \tag{A.10}$$

where b_{ijk}, Christoffel Symbols of the first kind, is given by $b_{ijk} = \frac{1}{2}(M_{ijk}+M_{ikj}-M_{jki})$ and $M_{ijk} = \frac{\partial M_{ij}}{\partial \theta_k}$ where M_{ij} an element of the mass matrix. Specifically, b_{ijk} is given by

$$\begin{cases} b_{111} = b_{222} = b_{333} = 0, \\ b_{122} = -m_2L_1l_2\sin(\theta_2) - m_3L_1(l_3\sin(\theta_2+\theta_3) + l_2\sin(\theta_2)), \\ b_{133} = -m_3l_3(L_1\sin(\theta_2+\theta_3) + L_2\sin(\theta_3)), \\ b_{233} = -m_3L_2l_3\sin((\theta_3)), \\ b_{211} = -b_{122}, \ b_{311} = -b_{133}, \ b_{322} = -b_{233}, \end{cases} \tag{A.11}$$

and

$$\begin{cases} b_{212} = b_{323} = 0, \ b_{213} = b_{223} = -b_{312}, \\ b_{112} = -m_2L_1l_2\sin(\theta_2) - m_3L_1(l_3\sin(\theta_2+\theta_3) + l_2\sin(\theta_2)), \\ b_{113} = -m_3l_3(L_1\sin(\theta_2+\theta_3) + L_2\sin(\theta_3)), \\ b_{123} = b_{113}, \ b_{312} = m_3L_2l_3\sin(\theta_3). \end{cases} \tag{A.12}$$

BIBLIOGRAPHY

[1] J. L. Pons, *Wearable robots: biomechatronic exoskeletons.* John Wiley & Sons, 2008.

[2] A. Schiele, "Ergonomics of exoskeletons: Objective performance metrics," in *World Haptics 2009 - Third Joint EuroHaptics conference and Symposium on Haptic Interfaces for Virtual Environment and Teleoperator Systems*, pp. 103–108, 2009.

[3] A. H. A. Stienen, E. E. G. Hekman, F. C. T. van der Helm, and H. van der Kooij, "Self-aligning exoskeleton axes through decoupling of joint rotations and translations," *IEEE Transactions on Robotics*, vol. 25, no. 3, pp. 628–633, 2009.

[4] M. A. Ergin and V. Patoglu, "A self-adjusting knee exoskeleton for robot-assisted treatment of knee injuries," in *2011 IEEE/RSJ International Conference on Intelligent Robots and Systems*, pp. 4917–4922, 2011.

[5] P. Heo, G. M. Gu, S.-j. Lee, K. Rhee, and J. Kim, "Current hand exoskeleton technologies for rehabilitation and assistive engineering," *International Journal of Precision Engineering and Manufacturing*, vol. 13, no. 5, pp. 807–824, 2012.

[6] M. A. Delph, S. A. Fischer, P. W. Gauthier, C. H. M. Luna, E. A. Clancy, and G. S. Fischer, "A soft robotic exomusculature glove with integrated semg sensing for hand rehabilitation," in *2013 IEEE 13th International Conference on Rehabilitation Robotics (ICORR)*, pp. 1–7, 2013.

[7] L. Gerez, J. Chen, and M. Liarokapis, "On the development of adaptive, tendon-driven, wearable exo-gloves for grasping capabilities enhancement," *IEEE Robotics and Automation Letters*, vol. 4, no. 2, pp. 422–429, 2019.

[8] J. L. Samper-Escudero, A. Gimenez-Fernandez, M. A. Sanchez-Uran, and M. Ferre, "A cable-driven exosuit for upper limb flexion based on fibres compliance," *IEEE Access*, vol. 8, pp. 153297–153310, 2020.

[9] A. T. Asbeck, S. M. De Rossi, I. Galiana, Y. Ding, and C. J. Walsh, "Stronger, smarter, softer: Next-generation wearable robots," *IEEE Robotics and Automation Magazine*, vol. 21, no. 4, pp. 22–33, 2014.

[10] J. Laut, M. Porfiri, and P. Raghavan, "The present and future of robotic technology in rehabilitation," *Current physical medicine and rehabilitation reports*, vol. 4, no. 4, pp. 312–319, 2016.

[11] P. Maciejasz, J. Eschweiler, K. Gerlach-Hahn, A. Jansen-Toy, and S. Leonhardt, “A survey on robotic devices for upper limb rehabilitation,” *Journal of Neuroengineering and Rehabilitation*, vol. 11, p. 3, 2014.

[12] M. A. Diftler, C. Ihrke, L. Bridgwater, J. Rogers, D. Davis, D. Linn, E. Laske, K. Ensley, and J. Lee, “Roboglove-a grasp assist device for earth and space,” in *International Conference on Environmental Systems*, no. JSC-CN-33541, 2015.

[13] S. Park, L. Bishop, T. Post, Yuchen Xiao, J. Stein, and M. Ciocarlie, “On the feasibility of wearable exotendon networks for whole-hand movement patterns in stroke patients,” in *IEEE International Conference on Robotics and Automation*, pp. 3729–3735, 2016.

[14] R. A. Stuck, L. M. Marshall, and R. Sivakumar, “Feasibility of SaeboFlex upper-limb training in acute stroke rehabilitation: A clinical case series,” *Occupational Therapy International*, vol. 21, no. 3, pp. 108–114, 2014.

[15] J. Sibonga, T. Matsumoto, J. Jones, J. Shapiro, T. Lang, L. Shackelford, S. M. Smith, M. Young, J. Keyak, K. Kohri, H. Ohshima, E. Spector, and A. LeBlanc, “Resistive exercise in astronauts on prolonged spaceflights provides partial protection against spaceflight-induced bone loss,” *Bone*, vol. 128, p. 112037, 2019.

[16] A. Villoslada, C. Rivera, N. Escudero, F. Martin, D. Blanco, and L. Moreno, “Hand exo-muscular system for assisting astronauts during extravehicular activities,” *Soft Robotics*, vol. 6, no. 1, pp. 21–37, 2019. PMID: 30457930.

[17] S. Hussain, P. K. Jamwal, P. Van Vliet, and M. H. Ghayesh, “State-of-the-art robotic devices for wrist rehabilitation: Design and control aspects,” *IEEE Transactions on Human-Machine Systems*, vol. 50, no. 5, pp. 361–372, 2020.

[18] J. Oblak, I. Cikajlo, and Z. Matjačić, “Universal haptic drive: A robot for arm and wrist rehabilitation,” *IEEE Transactions on Neural Systems and Rehabilitation Engineering : a publication of the IEEE Engineering in Medicine and Biology Society*, vol. 18, pp. 293–302, 10 2009.

[19] R. A. R. C. Gopura and K. Kiguchi, “Development of an exoskeleton robot for human wrist and forearm motion assist,” in *2007 International Conference on Industrial and Information Systems*, pp. 535–540, 2007.

[20] L. Masia, M. Casadio, P. Giannoni, G. Sandini, and P. Morasso, “Performance adaptive training control strategy for recovering wrist movements in stroke pa-

tients: A preliminary, feasibility study," *Journal of Neuroengineering and Rehabilitation*, vol. 6, p. 44, 12 2009.

[21] A. Gupta, M. K. O'Malley, V. Patoglu, and C. Burgar, "Design, control and performance of ricewrist: A force feedback wrist exoskeleton for rehabilitation and training," *The International Journal of Robotics Research*, vol. 27, no. 2, pp. 233–251, 2008.

[22] J. A. Martinez, P. Ng, S. Lu, M. S. Campagna, and O. Celik, "Design of wrist gimbal: A forearm and wrist exoskeleton for stroke rehabilitation," in *2013 IEEE 13th International Conference on Rehabilitation Robotics (ICORR)*, pp. 1–6, 2013.

[23] M. Dezman, T. Asfour, A. Ude, and A. Gams, "Exoskeleton arm pronation/supination assistance mechanism with a guided double rod system," in *2019 IEEE-RAS 19th International Conference on Humanoid Robots (Humanoids)*, pp. 559–564, 2019.

[24] K. Kiguchi, R. Esaki, and T. Fukuda, "Development of a wearable exoskeleton for daily forearm motion assist," *Advanced Robotics*, vol. 19, no. 7, pp. 751–771, 2005.

[25] J. Hope and A. Mcdaid, "Development of wearable wrist and forearm exoskeleton with shape memory alloy actuators," *Journal of Intelligent & Robotic Systems*, vol. 86, 06 2017.

[26] C. Lambelet, M. Lyu, D. Woolley, R. Gassert, and N. Wenderoth, "The eWrist — a wearable wrist exoskeleton with sEMG-based force control for stroke rehabilitation," in *2017 International Conference on Rehabilitation Robotics (ICORR)*, pp. 726–733, 2017.

[27] L. Sutton, H. Moein, A. Rafiee, J. D. W. Madden, and C. Menon, "Design of an assistive wrist orthosis using conductive nylon actuators," in *2016 6th IEEE International Conference on Biomedical Robotics and Biomechatronics (BioRob)*, pp. 1074–1079, 2016.

[28] S. Sangha, A. M. Elnady, and C. Menon, "A compact robotic orthosis for wrist assistance," in *2016 6th IEEE International Conference on Biomedical Robotics and Biomechatronics (BioRob)*, pp. 1080–1085, 2016.

[29] T. Higuma, K. Kiguchi, and J. Arata, "Low-profile two-degree-of-freedom wrist

exoskeleton device using multiple spring blades," *IEEE Robotics and Automation Letters*, vol. 3, no. 1, pp. 305–311, 2018.

[30] J. Realmuto and T. Sanger, "A robotic forearm orthosis using soft fabric-based helical actuators," in *2019 2nd IEEE International Conference on Soft Robotics (RoboSoft)*, pp. 591–596, 2019.

[31] S. Park, J. Yi, D. Kim, Y. Lee, H. S. Koo, and Y. Park, "A lightweight, soft wearable sleeve for rehabilitation of forearm pronation and supination," in *2019 2nd IEEE International Conference on Soft Robotics (RoboSoft)*, pp. 636–641, 2019.

[32] N. W. Bartlett, V. Lyau, W. A. Raiford, D. Holland, J. B. Gafford, T. D. Ellis, and C. J. Walsh, "A Soft Robotic Orthosis for Wrist Rehabilitation1," *Journal of Medical Devices*, vol. 9, 09 2015. 030918.

[33] I. Gaponov, D. Popov, and J. H. Ryu, "Twisted string actuation systems: A study of the mathematical model and a comparison of twisted strings," *IEEE/ASME Transactions on Mechatronics*, vol. 19, no. 4, pp. 1331–1342, 2014.

[34] G. Palli, C. Natale, C. May, C. Melchiorri, and T. Wurtz, "Modeling and control of the twisted string actuation system," *IEEE/ASME Transactions on Mechatronics*, vol. 18, no. 2, pp. 664–673, 2012.

[35] P. Polygerinos, Z. Wang, K. C. Galloway, R. J. Wood, and C. J. Walsh, "Soft robotic glove for combined assistance and at-home rehabilitation," *Robotics and Autonomous Systems*, vol. 73, pp. 135–143, 2015. Wearable Robotics.

[36] A. D. Deshpande, J. Ko, D. Fox, and Y. Matsuoka, "Control strategies for the index finger of a tendon-driven hand," *The International Journal of Robotics Research*, vol. 32, no. 1, pp. 115–128, 2013.

[37] P. Tran, S. Jeong, K. Herrin, S. Bhatia, S. Kozin, and J. P. Desai, "Flexotendon glove-iii: Soft robotic hand rehabilitation exoskeleton for spinal cord injury," in *2021 IEEE International Conference on Robotics and Automation (ICRA)*, pp. 10332–10339, 2021.

[38] M. H. Yun, H. Jun Eoh, and J. Cho, "A two-dimensional dynamic finger modeling for the analysis of repetitive finger flexion and extension," *International Journal of Industrial Ergonomics*, vol. 29, no. 4, pp. 231–248, 2002.

[39] *Towards a Robotic Hand Rehabilitation Exoskeleton for Stroke Therapy*, vol. 1 of *Dynamic Systems and Control Conference*, 10 2014.

[40] P. Polygerinos, K. C. Galloway, E. Savage, M. Herman, K. O. Donnell, and C. J. Walsh, "Soft robotic glove for hand rehabilitation and task specific training," in *IEEE International Conference on Robotics and Automation*, pp. 2913–2919, 2015.

[41] H. K. Yap, Jeong Hoon Lim, F. Nasrallah, J. C. H. Goh, and R. C. H. Yeow, "A soft exoskeleton for hand assistive and rehabilitation application using pneumatic actuators with variable stiffness," in *IEEE International Conference on Robotics and Automation*, pp. 4967–4972, 2015.

[42] C. T. O'Neill, N. S. Phipps, L. Cappello, S. Paganoni, and C. J. Walsh, "A soft wearable robot for the shoulder: Design, characterization, and preliminary testing," in *IEEE International Conference on Rehabilitation Robotics*, pp. 1672–1678, 2017.

[43] M. Feng, D. Yang, and G. Gu, "High-force fabric-based pneumatic actuators with asymmetric chambers and interference-reinforced structure for soft wearable assistive gloves," *IEEE Robotics and Automation Letters*, vol. 6, no. 2, pp. 3105–3111, 2021.

[44] P. H. Nguyen and W. Zhang, "Design and computational modeling of fabric soft pneumatic actuators for wearable assistive devices," *Scientific reports*, vol. 10, no. 1, pp. 1–13, 2020.

[45] J. Realmuto and T. Sanger, "A robotic forearm orthosis using soft fabric-based helical actuators," in *2019 2nd IEEE International Conference on Soft Robotics (RoboSoft)*, pp. 591–596, IEEE, 2019.

[46] H. K. Yap, N. Kamaldin, J. H. Lim, F. A. Nasrallah, J. C. H. Goh, and C.-H. Yeow, "A magnetic resonance compatible soft wearable robotic glove for hand rehabilitation and brain imaging," *IEEE Transactions on Neural Systems and Rehabilitation Engineering*, vol. 25, no. 6, pp. 782–793, 2017.

[47] P. Polygerinos, Z. Wang, K. C. Galloway, R. J. Wood, and C. J. Walsh, "Soft robotic glove for combined assistance and at-home rehabilitation," *Robotics and Autonomous Systems*, vol. 73, pp. 135–143, 2015. Wearable Robotics.

[48] S. S. Cheng, Y. Kim, and J. P. Desai, "New actuation mechanism for actively

cooled SMA springs in a neurosurgical robot," *IEEE Transactions on Robotics*, vol. 33, no. 4, pp. 986–993, 2017.

[49] A. Simeonov, T. Henderson, Z. Lan, G. Sundar, A. Factor, J. Zhang, and M. Yip, "Bundled super-coiled polymer artificial muscles: Design, characterization, and modeling," *IEEE Robotics and Automation Letters*, vol. 3, no. 3, pp. 1671–1678, 2018.

[50] T. Tsabedze, C. Mullen, R. Coulter, S. Wade, and J. Zhang, "Helically wrapped supercoiled polymer (HW-SCP) artificial muscles: Design, characterization, and modeling," in *Proceedings of IEEE International Conference on Robotics and Automation*, 2020.

[51] L. Saharan, M. J. de Andrade, W. Saleem, R. H. Baughman, and Y. Tadesse, "iGrab: Hand orthosis powered by twisted and coiled polymer muscles," *Smart Materials and Structures*, vol. 26, no. 10, p. 105048, 2017.

[52] C. S. Haines, M. D. Lima, N. Li, G. M. Spinks, J. Foroughi, J. D. W. Madden, S. H. Kim, S. Fang, M. Jung de Andrade, F. Göktepe, Ö. Göktepe, S. M. Mirvakili, S. Naficy, X. Lepró, J. Oh, M. E. Kozlov, S. J. Kim, X. Xu, B. J. Swedlove, G. G. Wallace, and R. H. Baughman, "Artificial muscles from fishing line and sewing thread," *Science*, vol. 343, no. 6173, pp. 868–872, 2014.

[53] X. Tang, K. Li, Y. Liu, D. Zhou, and J. Zhao, "A soft crawling robot driven by single twisted and coiled actuator," *Sensors and Actuators A: Physical*, vol. 291, pp. 80–86, 2019.

[54] Y. Yang, Z. Liu, Y. Wang, S. Liu, and M. Y. Wang, "A compact and low-cost robotic manipulator driven by supercoiled polymer actuators," in *2020 IEEE International Conference on Robotics and Automation (ICRA)*, 2020.

[55] Y. A. Tse, K. W. Wong, Y. Yang, and M. Y. Wang, "Novel design of a soft pump driven by super-coiled polymer artificial muscles," in *2020 IEEE/RSJ International Conference on Intelligent Robots and Systems (IROS)*, pp. 8789–8794, 2020.

[56] S. Wang, H. Huang, H. Huang, B. Li, and K. Huang, "A lightweight soft gripper driven by self-sensing super-coiled polymer actuator," *IEEE Robotics and Automation Letters*, vol. 6, no. 2, pp. 2775–2782, 2021.

[57] T. Tsabedze, C. Mullen, R. Coulter, S. Wade, and J. Zhang, "Helically wrapped supercoiled polymer (HW-SCP) artificial muscles: Design, characterization, and

modeling," in *2020 IEEE International Conference on Robotics and Automation (ICRA)*, pp. 5862–5868, 2020.

[58] T. Tsabedze and J. Zhang, "Design, characterization, modeling, and comparison of helically wrapped super-coiled polymer artificial muscles," *Sensors and Actuators A: Physical*, vol. 331, p. 113018, 2021.

[59] T. Tsabedze, F. McLelland, F. van Breugel, and J. Zhang, "Parameter estimation and adaptive control of super-coiled polymer artificial muscles," *IFAC-PapersOnLine*, vol. 55, no. 37, pp. 445–450, 2022. 2nd Modeling, Estimation and Control Conference MECC 2022.

[60] D. Bombara, S. Fowzer, and J. Zhang, "Compliant, large-strain, and self-sensing twisted string actuators," *Soft Robotics*, vol. 9, no. 1, pp. 72–88, 2022.

[61] D. Bombara, R. Konda, and J. Zhang, "Experimental characterization and modeling of the self-sensing property in compliant twisted string actuators," *IEEE Robotics and Automation Letters*, vol. 6, no. 2, pp. 974–981, 2021.

[62] Z. Ma, P. Ben-Tzvi, and J. Danoff, "Hand rehabilitation learning system with an exoskeleton robotic glove," *IEEE Transactions on Neural Systems and Rehabilitation Engineering*, vol. 24, no. 12, pp. 1323–1332, 2016.

[63] E. Rho, D. Kim, H. Lee, and S. Jo, "Learning fingertip force to grasp deformable objects for soft wearable robotic glove with tsm," *IEEE Robotics and Automation Letters*, vol. 6, no. 4, pp. 8126–8133, 2021.

[64] H. In, B. B. Kang, M. Sin, and K.-J. Cho, "Exo-glove: A wearable robot for the hand with a soft tendon routing system," *IEEE Robotics and Automation Magazine*, vol. 22, no. 1, pp. 97–105, 2015.

[65] L.-W. Tsai, "Design of tendon-driven manipulators," *Journal of Mechanical Design*, vol. 117, pp. 80–86, 06 1995.

[66] P. Rao, Q. Peyron, S. Lilge, and J. Burgner-Kahrs, "How to model tendon-driven continuum robots and benchmark modelling performance," *Frontiers in Robotics and AI*, vol. 7, p. 223, 2021.

[67] S. Jacobsen, H. Ko, E. Iversen, and C. Davis, "Control strategies for tendon-driven manipulators," *IEEE Control Systems Magazine*, vol. 10, no. 2, pp. 23–28, 1990.

[68] S. Ma, S. Hirose, and H. Yoshinada, “Design and experiments for a coupled tendon-driven manipulator,” *IEEE Control Systems Magazine*, vol. 13, no. 1, pp. 30–36, 1993.

[69] L. Gerez, J. Chen, and M. Liarokapis, “On the development of adaptive, tendon-driven, wearable exo-gloves for grasping capabilities enhancement,” *IEEE Robotics and Automation Letters*, vol. 4, no. 2, pp. 422–429, 2019.

[70] C. Liu, A. Bera, T. Tsabedze, D. Edgar, and M. Yim, “Spiral zipper manipulator for aerial grasping and manipulation,” in *2019 IEEE/RSJ International Conference on Intelligent Robots and Systems (IROS)*, pp. 3179–3184, 2019.

[71] V. Vikas, E. Cohen, R. Grassi, C. Sözer, and B. Trimmer, “Design and locomotion control of a soft robot using friction manipulation and motor–tendon actuation,” *IEEE Transactions on Robotics*, vol. 32, no. 4, pp. 949–959, 2016.

[72] X. Chen, P. Stegagno, and C. Yuan, “A cable-driven switching-legged inchworm soft robot: Design and testing,” in *2021 American Control Conference (ACC)*, pp. 2–7, 2021.

[73] D. S. Shah, J. W. Booth, R. L. Baines, K. Wang, M. Vespignani, K. Bekris, and R. Kramer-Bottiglio, “Tensegrity robotics,” *Soft Robotics*, ahead of print, http://doi.org/10.1089/soro.2020.0170.

[74] I. Gaponov, D. Popov, and J. H. Ryu, “Twisted string actuation systems: A study of the mathematical model and a comparison of twisted strings,” *IEEE/ASME Transactions on Mechatronics*, vol. 19, no. 4, pp. 1331–1342, 2014.

[75] G. Palli, C. Natale, C. May, C. Melchiorri, and T. Wurtz, “Modeling and control of the twisted string actuation system,” *IEEE/ASME Transactions on Mechatronics*, vol. 18, no. 2, pp. 664–673, 2013.

[76] J. Zhang, J. Sheng, C. T. O’Neill, C. J. Walsh, R. J. Wood, J.-H. Ryu, J. P. Desai, and M. C. Yip, “Robotic artificial muscles: Current progress and future perspectives,” *IEEE Transactions on Robotics*, vol. 35, no. 3, pp. 761–781, 2019.

[77] K. J. Kim, H. R. Choi, X. Tan, and D. Pugal, *Biomimetic robotic artificial muscles.* World Scientific, 2013.

[78] T. Tsabedze, E. Hartman, and J. Zhang, “A compact, compliant, and biomimetic robotic assistive glove driven by twisted string actuators,” *Inter-*

national Journal of Intelligent Robotics and Applications, vol. 5, no. 3, pp. 381–394, 2021.

[79] R. Shisheie, L. Jiang, L. Banta, and M. Cheng, “Modeling and control of a bidirectional twisted-string actuation for an upper arm robotic device,” *Proceedings of the American Control Conference*, vol. 2015-July, pp. 5794–5799, 2015.

[80] R. Konda, D. Bombara, S. Swanbeck, and J. Zhang, “Anthropomorphic twisted string-actuated soft robotic gripper with tendon-based stiffening,” *IEEE Transactions on Robotics*, 2022, to appear.

[81] I.-W. Park and V. SunSpiral, “Impedance controlled twisted string actuators for tensegrity robots,” in *2014 14th International Conference on Control, Automation and Systems (ICCAS 2014)*, pp. 1331–1338, 2014.

[82] B. Suthar and S. Jung, “Design and feasibility analysis of a foldable robot arm for drones using a twisted string actuator: FRAD-TSA,” *IEEE Robotics and Automation Letters*, vol. 6, no. 3, pp. 5769–5775, 2021.

[83] D. Lee, D. H. Kim, C. H. Che, J. B. In, and D. Shin, “Highly durable bidirectional joint with twisted string actuators and variable radius pulley,” *IEEE/ASME Transactions on Mechatronics*, vol. 25, no. 1, pp. 360–370, 2020.

[84] A. Pepe, M. Hosseini, U. Scarcia, G. Palli, and C. Melchiorri, “Development of an haptic interface based on twisted string actuators,” in *2017 IEEE International Conference on Advanced Intelligent Mechatronics (AIM)*, pp. 28–33, 2017.

[85] M. Tavakoli, R. Batista, and P. Neto, “A compact two-phase twisted string actuation system: Modeling and validation,” *Mechanism and Machine Theory*, vol. 101, pp. 23–35, 2016.

[86] I. Gaponov, D. Popov, S. J. Lee, and J.-H. Ryu, “Auxilio: A portable cable-driven exosuit for upper extremity assistance,” *International Journal of Control, Automation and Systems*, vol. 15, no. 1, pp. 73–84, 2017.

[87] S. Nedelchev, I. Gaponov, and J.-H. Ryu, “Accurate dynamic modeling of twisted string actuators accounting for string compliance and friction,” *IEEE Robotics and Automation Letters*, vol. 5, no. 2, pp. 3438–3443, 2020.

[88] D. Bombara, R. Konda, Z. Kibria, and J. Zhang, “Inverse modeling for com-

ponent selection of twisted string actuators," *IEEE/ASME Transactions on Mechatronics*, pp. 1–12, 2022.

[89] S. Nedelchev, I. Gaponov, and J.-H. Ryu, "Accurate dynamic modeling of twisted string actuators accounting for string compliance and friction," *IEEE Robotics and Automation Letters*, vol. 5, no. 2, pp. 3438–3443, 2020.

[90] T. E. Pillsbury, N. M. Wereley, and Q. Guan, "Comparison of contractile and extensile pneumatic artificial muscles," *Smart Materials and Structures*, vol. 26, no. 9, p. 095034, 2017.

[91] T. W. Henderson, Y. Zhi, A. Liu, and M. C. Yip, "Data-driven actuator selection for artificial muscle-powered robots," in *IEEE Conference on Robotics and Automation (ICRA)*, 2021.

[92] "Pololu micro metal gearmotors," 2021.

[93] A. San-Millan Rodriguez, M. Hosseini, and J. Paik, "A hybrid control strategy for force and precise end effector positioning of a twisted string actuator," *IEEE/ASME Transactions on Mechatronics*, early access, 2020.

[94] M. Usman, H. Seong, B. Suthar, I. Gaponov, and J.-H. Ryu, "A study on life cycle of twisted string actuators: Preliminary results," in *2017 IEEE/RSJ International Conference on Intelligent Robots and Systems (IROS)*, pp. 4680–4685, 2017.

[95] M. C. Hume, H. Gellman, H. McKellop, and R. H. Brumfield, "Functional range of motion of the joints of the hand," *The Journal of Hand Surgery*, vol. 15A, no. 2, pp. 240–243, 1990.

[96] J. Becker, N. Thakor, and K. Gruben, "A study of human hand tendon kinematics with applications to robot hand design," in *Proceedings. 1986 IEEE International Conference on Robotics and Automation*, vol. 3, pp. 1540–1545, 1986.

[97] H. J. Freund, "Time control of hand movements," *Progress in Brain Research*, vol. 64, pp. 287–294, 1986.

[98] O. Sandoval-Gonzalez, J. Jacinto-Villegas, I. Herrera-Aguilar, O. Portillo-Rodiguez, P. Tripicchio, M. Hernandez-Ramos, A. Flores-Cuautle, and C. Avizzano, "Design and development of a hand exoskeleton robot for active and pas-

sive rehabilitation," *International Journal of Advanced Robotic Systems*, vol. 13, no. 2, p. 66, 2016.

[99] J. Sun and J. Zhao, "Integrated actuation and self-sensing for twisted-and-coiled actuators with applications to innervated soft robots," in *2020 IEEE/RSJ International Conference on Intelligent Robots and Systems (IROS)*, pp. 8795–8800, 2020.

[100] J. Sun, B. Tighe, Y. Liu, and J. Zhao, "Twisted-and-coiled actuators with free strokes enable soft robots with programmable motions," *Soft Robotics*, 2020.

[101] Z. Sun, L. Hao, B. Song, R. Yang, R. Cao, and Y. Cheng, "Periodic reference tracking control approach for smart material actuators with complex hysteretic characteristics," *Smart Materials and Structures*, vol. 25, p. 105029, sep 2016.

[102] R. Gilster, C. Hesse, and H. Deubel, "Contact points during multidigit grasping of geometric objects," *Experimental Brain Research*, vol. 217, no. 1, pp. 137–151, 2012.

[103] I. M. Bullock, T. Feix, and A. M. Dollar, "Analyzing human fingertip usage in dexterous precision manipulation: Implications for robotic finger design," in *IEEE/RSJ International Conference on Intelligent Robots and Systems*, pp. 1622–1628, 2014.

[104] I. M. Bullock, T. Feix, and A. M. Dollar, "Dexterous workspace of human two- and three-fingered precision manipulation," in *IEEE Haptics Symposium*, pp. 41–47, 2014.

[105] A. A. Sayer, H. E. Syddall, H. J. Martin, E. M. Dennison, H. C. Roberts, and C. Cooper, "Is grip strength associated with health-related quality of life? Findings from the Hertfordshire Cohort Study," *Age and Ageing*, vol. 35, pp. 409–415, 05 2006.

[106] B. Redmond, R. Aina, T. Gorti, and B. Hannaford, "Haptic characteristics of some activities of daily living," in *2010 IEEE Haptics Symposium*, pp. 71–76, 2010.

[107] C. L. Taylor and R. J. Schwarz, "The anatomy and mechanics of the human hand," *Artificial limbs*, vol. 2, no. 2, pp. 22–35, 1955.

[108] J. Zhang, D. Bombara, S. Fowzer, and Brennan, "Compliant and large-strain

twisted string actuators using supercoiled polymers," in *Proceedings of IEEE International Conference on Soft Robotics*, 2020.

[109] D. Bombara, V. Mansurov, R. Konda, S. Fowzer, and J. Zhang, "Self-sensing for twisted string actuators using conductive supercoiled polymers," in *Proc. ASME Conf. Smart Materials, Adaptive Structures and Intelligent Systems*, Paper SMASIS2019-5587, 2019.

[110] H. Lee, H. Choi, and S. Park, "Accurate modeling and nonlinearity compensation in the speed mode of a twisted string actuator," *Mechanism and Machine Theory*, vol. 137, pp. 53–66, 2019.

[111] L. Wu, M. J. de Andrade, L. K. Saharan, R. S. Rome, R. H. Baughman, and Y. Tadesse, "Compact and low-cost humanoid hand powered by nylon artificial muscles," *Bioinspiration & Biomimetics*, vol. 12, p. 026004, feb 2017.

[112] A. Abbas and J. Zhao, "Twisted and coiled sensor for shape estimation of soft robots," in *2017 IEEE/RSJ International Conference on Intelligent Robots and Systems (IROS)*, pp. 482–487, 2017.

[113] B. B. Kang, H. Choi, H. Lee, and K.-J. Cho, "Exo-Glove poly II: A polymer-based soft wearable robot for the hand with a tendon-driven actuation system," *Soft Robotics*, vol. 6, no. 2, pp. 214–227, 2019.

[114] S. C. Chirinos and E. A. Vela, "A modular soft robotic exoskeleton for active hand rehabilitation after stroke," in *2021 IEEE Engineering International Research Conference (EIRCON)*, pp. 1–4, 2021.

[115] S. Koizumi, T.-H. Chang, H. Nabae, G. Endo, K. Suzumori, M. Mita, K. Saitoh, K. Hatakeyama, S. Chida, and Y. Shimada, "Soft robotic gloves with thin McKibben muscles for hand assist and rehabilitation," in *2020 IEEE/SICE International Symposium on System Integration (SII)*, pp. 93–98, 2020.

[116] A. Erwin, F. Sergi, V. Chawda, and M. K. O'Malley, "Interaction control for rehabilitation robotics via a low-cost force sensing handle," in *Dynamic Systems and Control Conference*, 10 2013.

[117] "Force Sensing Resistor®(FSR®) 400 series," 2022.

[118] D. Bombara, R. Konda, and J. Zhang, "Experimental characterization and modeling of the self-sensing property in compliant twisted string actuators," *IEEE Robotics and Automation Letters*, vol. 6, no. 2, pp. 974–981, 2021.

[119] T. Tsabedze and J. Zhang, "Design, characterization, modeling, and comparison of helically wrapped super-coiled polymer artificial muscles," *Sensors and Actuators A: Physical*, vol. 331, p. 113018, 2021.

[120] "STMicroelectronics," 2023.

[121] "Allegro microsystems," 2023.

[122] J. Jang, K. Kim, J. Lee, B. Lim, and Y. Shim, "Online gait task recognition algorithm for hip exoskeleton," in *2015 IEEE/RSJ International Conference on Intelligent Robots and Systems (IROS)*, pp. 5327–5332, 2015.

[123] B.-S. Lin, I.-J. Lee, S.-Y. Yang, Y.-C. Lo, J. Lee, and J.-L. Chen, "Design of an inertial-sensor-based data glove for hand function evaluation," *Sensors*, vol. 18, no. 5, 2018.

[124] S. Lee, H. Lee, J. Lee, H. Ryu, I. Y. Kim, and J. Kim, "Clip-on IMU system for assessing age-related changes in hand functions," *Sensors*, vol. 20, no. 21, 2020.

[125] S. Y. Song, Y. Pei, and E. T. Hsiao-Wecksler, "Estimating relative angles using two inertial measurement units without magnetometers," *IEEE Sensors Journal*, vol. 22, no. 20, pp. 19688–19699, 2022.

[126] S. O. H. Madgwick, A. J. L. Harrison, and R. Vaidyanathan, "Estimation of IMU and MARG orientation using a gradient descent algorithm," in *2011 IEEE International Conference on Rehabilitation Robotics*, pp. 1–7, 2011.

[127] D. Lee, I. Gaponov, and J.-H. Ryu, "Effect of vibration on twisted string actuation through conduit at high bending angles," in *2019 IEEE/RSJ International Conference on Intelligent Robots and Systems (IROS)*, pp. 5965–5970, 2019.

[128] R. A. R. C. Gopura and K. Kiguchi, "EMG-based control of an exoskeleton robot for human forearm and wrist motion assist," in *2008 IEEE International Conference on Robotics and Automation*, pp. 731–736, 2008.

[129] R. H. Brumfield and J. A. Champoux, "A biomechanical study of normal functional wrist motion," *Clinical Orthopaedics and Related Research*, no. 187, 1984.

[130] W. D. B. Nancy Berryman Reese, Charlotte Yates, *Joint Range of Motion and Muscle Length Testing.* Saunders, Elsevier, 3rd edition ed., 2016.

[131] M. E. Abdallah, R. Platt, B. Hargrave, and F. Permenter, “Position control of tendon-driven fingers with position controlled actuators,” in *2012 IEEE International Conference on Robotics and Automation*, pp. 2859–2864, 2012.

[132] P. Agarwal, J. Fox, Y. Yun, M. K. O’Malley, and A. D. Deshpande, “An index finger exoskeleton with series elastic actuation for rehabilitation: Design, control and performance characterization,” *The International Journal of Robotics Research*, vol. 34, no. 14, pp. 1747–1772, 2015.

[133] M. Spong, S. Hutchinson, and M. Vidyasagar, *Robot Modeling and Control*. Wiley, 2005.

[134] L. Zollo, S. Roccella, E. Guglielmelli, M. C. Carrozza, and P. Dario, “Biomechatronic design and control of an anthropomorphic artificial hand for prosthetic and robotic applications,” *IEEE/ASME Transactions on Mechatronics*, vol. 12, no. 4, pp. 418–429, 2007.

[135] M. C. Carrozza, C. Suppo, F. Sebastiani, B. Massa, F. Vecchi, R. Lazzarini, M. R. Cutkosky, and P. Dario, “The SPRING hand: Development of a self-adaptive prosthesis for restoring natural grasping,” *Auton. Robots*, vol. 16, p. 125–141, mar 2004.

[136] R. M. Murray, S. Sastry, and Z. Li, “A mathematical introduction to robotic manipulation,” 1994.

[137] H. Li, L. Cheng, N. Sun, and R. Cao, “Design and control of an underactuated finger exoskeleton for assisting activities of daily living,” *IEEE/ASME Transactions on Mechatronics*, vol. 27, no. 5, pp. 2699–2709, 2022.

[138] Y. Wang, S. Zheng, Z. Song, J. Pang, and J. Li, “A coupling dynamic model for studying the physical interaction between a finger exoskeleton and a human finger,” *IEEE Access*, vol. 8, pp. 125412–125422, 2020.

[139] C. D. Metcalf, R. Robinson, A. J. Malpass, T. P. Bogle, T. A. Dell, C. Harris, and S. H. Demain, “Markerless motion capture and measurement of hand kinematics: Validation and application to home-based upper limb rehabilitation,” *IEEE Transactions on Biomedical Engineering*, vol. 60, no. 8, pp. 2184–2192, 2013.

[140] D. G. Kamper, H. C. Fischer, and E. G. Cruz, “Impact of finger posture on mapping from muscle activation to joint torque,” *Clinical Biomechanics*, vol. 21, no. 4, pp. 361–369, 2006.

[141] H. Liu, C. Wu, S. Lin, Y. Chen, Y. Hu, T. Xu, W. Yuan, and Y. Li, “Finger flexion and extension driven by a single motor in robotic glove design,” *Advanced Intelligent Systems*, vol. 5, no. 5, p. 2200274, 2023.

[142] Z. Q. Tang, H. L. Heung, K. Y. Tong, and Z. Li, “Model-based online learning and adaptive control for a “human-wearable soft robot” integrated system,” *The International Journal of Robotics Research*, vol. 40, no. 1, pp. 256–276, 2021.